Copyright

by

Lindsay Jo Olinde

2015

The Dissertation Committee for Lindsay Jo Olinde Certifies that this is the approved version of the following dissertation:

DISPLACEMENT AND ENTRAINMENT BEHAVIOR OF BEDLOAD CLASTS IN MOUNTAIN STREAMS

Committee:

Joel Johnson, Supervisor

David Mohrig

Kevan Moffett

Paola Passalacqua

Elowyn Yager

DISPLACEMENT AND ENTRAINMENT BEHAVIOR OF BEDLOAD CLASTS IN MOUNTAIN STREAMS

by

Lindsay Jo Olinde, B.S.C.E.; M.S.

Dissertation

Presented to the Faculty of the Graduate School of

The University of Texas at Austin

in Partial Fulfillment

of the Requirements

for the Degree of

Doctor of Philosophy

The University of Texas at Austin

May 2015

Acknowledgements

I first thank my advisor, Joel Johnson, for giving me the opportunity to delve into fluvial geomorphology and for his enthusiasm advancing our field. I also thank my other committee members, David Mohrig, Paola Passalacqua, Kevan Moffett and Elowyn Yager. I am grateful for their insights and mentorship over the course of my dissertation research. I also appreciate the many friends and family who provided field and laboratory support, including Austin Morrell, Michael Markowski, Michael Olinde, Karen Foote, Brandon Minton, Travis Swanson, Alexander Aronovitz, Katie Delbecq, Jamie Levine, Joseph Kugler, Brendan Murphy, Jon Sanfilippo, Marc Rached, Peter Polito, Angel Monsalve, Jillian Rowley and Christopher Clements. Additionally, I thank the Jackson School and broader geomorphology community for their humor, support and brainstorming, especially Philip Guerrero, Brittany Smith, Lauren Andrews, Kevin Befus, Anastasia Piliouras, Mauricio Perillo, Man Liang, Kealie Goodwin, Audrey Sawyer and Colin Phillips. The USDA-ARS team at the Reynolds Creek Experimental Watershed also deserves significant recognition, particularly Barry Caldwell's welding efforts and John Wilford's assistance with electronics. This work was funded by a grant from the National Science Foundation (EAR 1053508) and student grants from Geological Society of America, American Association of Petroleum Geologists, American Federation of Mineralogical Sciences, ConocoPhillips and University of Texas Jackson School.

DISPLACEMENT AND ENTRAINMENT BEHAVIOR OF BEDLOAD CLASTS IN MOUNTAIN STREAMS

Lindsay Jo Olinde, Ph.D.

The University of Texas at Austin, 2015

Supervisor: Joel Johnson

Understanding how individual grains and populations of grains move through alluvial systems is important for predicting how landscapes adjust to changes in climate, tectonics and watershed management. Mountainous terrain covers over 20% of Earth's landscape and channels running through these steep slopes deliver significant volumes of sediment to lowland systems. However, most historic sediment transport studies were conducted in lowland rivers and laboratory experiments. Recently, upland stream studies have had limited success in monitoring the bedload fraction of sediment transported during floods exceeding bankfull flows. To address the scarcity of bedload observations in natural streams, I characterized bedload displacement and entrainment behavior in a mountain stream over a range of temporal and spatial scales. I designed and developed new fluvial geomorphology tools, including active tracers that were clasts embedded with accelerometers to record the timing of motion relative to discharge. I also deployed passive tracers which were bedload clasts embedded with radio frequency identification (RFID) tags. The passive tracers were used to determined flood-scale displacement lengths. Additionally, I installed RFID antennas on the channel bed to record the times that tracers passed through a reach. Flow strength during flood events was estimated using discharge records and numerical modeling. Datasets collected by the active and

passive tracers demonstrated that probabilities of transport, average step lengths and cumulative displacement distances scale with discharge. The heavy-tailed measurements of rest times from the active tracers suggested that bedload transport is superdiffusive in mountain streams. Transport, deposition and re-entrainment records showed that thresholds of motion are best represented by a distribution rather than a constant value, are influenced by channel width and bed slope, and can be lower at re-entrainment than deposition. Historic discharge records and field-modified transport formulas predicted that a broad range of discharges contribute significant fractions of the total bedload volumes, and that magnitude-frequency analyses are highly sensitive to common scaling and extrapolation techniques. The rare field-based observations from this research provide new insights into the complex mechanisms that drive bedload dispersion in mountain streams.

Table of Contents

List of Tables

List of Figures

CHAPTER 1: INTRODUCTION

1.1 Motivation

Understanding how mountain streams transport bedload is important for predicting the extent to which these channels and their sediment budgets may shift due to changes in tectonics, climate, and management. Such knowledge is crucial for predicting the degree that these changes may affect rivers downstream. Implications regarding how, when and where sediment is entrained, deposited and re-entrained are relevant to river management, watershed sediment budget and landscape modeling efforts.

Much of the previous work characterizing bedload transport in natural streams and thresholds required to entrain grains have focused on observations from lowland rivers or flume experiments [e.g., *Shields*, 1936; *Einstein*, 1950; *Leopold and Wolman*, 1960; *Wolman and Miller*, 1960]. Bedload transport relations and concepts developed in lowland rivers are often applied to streams in steep mountainous terrains due to the scarcity of datasets that measure transport conditions in coarse and steep alluvial channels, [e.g., *Dietrich and Dunne*, 1978; *Andrews and Nankervis*, 1995; *Whipple and Tucker*, 1999; *Doyle et al.*, 2007; *USDA-NRCS*, 2007]. However, relations generated from these lowland studies may not be fully applicable in steeper, upland channels due to the differences in grain size distributions, slopes, hydrologic regimes and sediment supply [e.g., *Montgomery and Buffington*, 1997; *Yager et al.*, 2007; *Wohl*, 2010]. Additionally, uncertainties in bedload transport thresholds that are estimated for mountain streams can cause predictions of bedload transport to vary by orders of magnitude [e.g., *Buffington and Montgomery*, 1997; *Barry et al.*, 2008].

The objective of this dissertation is to improve the characterization of bedload transport in mountain streams. I combine field monitoring studies with numerical modeling to evaluate the complex roles that channel morphology and stochastic hydrologic forcing have in driving the

transport of individual bedload clasts as well as the collective transport of populations of clasts over time. The overall research questions addressed in this work were:

- How do the probabilities of transport, average step lengths and rest times of bedload clasts vary with discharges?
- How do transport thresholds vary with grain size, deposition locations vary with hydrologic forcing and channel morphology and re-entrainment conditions vary with deposition conditions?
- How do total bedload volumes vary with discharge magnitude and frequency in mountain streams?

1.2 Dissertation organization

In Chapter 2, I characterized total clast displacement distances as a function of hydrologic forcing as well as the individual clast steps that total displacements reflect. I also quantified the probabilities that a given clast was transported as a function of discharge and, once transported, how average step lengths increased as a function of discharge. Measurements of clast rest time during eleven snowmelt floods provided new insights into the superdiffusive behavior of bedload transport in mountain streams. I included details of the new bedload monitoring technologies that I developed as part of this dissertation research. The design of in-stream Radio Frequency Identification (RFID) antennas and active tracers (accelerometer-tagged cobbles) enabled the collection of rare measurements of bedload mobility during flood events using both Lagrangian and Eulerian perspectives.

In Chapter 3, I combined field observations with flow modeling to further explore thresholds associated with the transport, deposition and re-entrainment of bedload clasts in mountain streams. Transport thresholds were constrained in one of the study reaches using the

RFID-embedded tracers and in-stream RFID antennas to build a hiding function that shows initiation of motion as a function of grain size. The resulting hiding function showed that equal entrainment mobility conditions existed in the reach for a range of tracer sizes, indicating that the initiation of motion of the coarser tracers coincided with that of the finer portion. The deposition records from active tracers demonstrated that mobility thresholds can vary with channel width and bed slope. Combining these results with those of previous studies indicated that transport thresholds in steeper channels are more sensitive to changes in slope than those in channels having gradients that are orders of magnitude lower. Comparing deposition and re-entrainment conditions, I found that discharges when clasts are re-entrained can be less than when they were deposited. This observation diverges from the classic theory that re-entrainment conditions are similar to or larger than those of deposition [e.g., *Hjulström*, 1935; *Shields*, 1936].

The temporal scope of the dissertation was expanded in Chapter 4 to examine the cumulative effects that transport thresholds and hydrologic forcing can have on bedload transport over decadal timescales. Predictions of the discharges most effective at transporting over a time period of 48 years demonstrated that bedload transport in mountain streams is most affected by low magnitude and high frequency events, and that the discharges that most contribute to total bedload volumes are best considered as a broad range rather than a single value. The results also showed that magnitude-frequency results are sensitive to transport threshold assumptions and extrapolation of bedload discharge-water discharge relations, particularly at the higher discharges that rarely are constrained by field measurements.

Chapter 5 summarizes the key findings from the presented dissertation research. Implications of the conclusions are discussed in terms of their potential to improve the accuracy of sediment budgets, success of river restoration projects and predictions of landscape models. Remaining questions to motivate future fluvial geomorphology studies are also listed.

CHAPTER 2: USING RFID AND ACCELEROMETER TRACERS TO MEASURE PROBABILITIES OF TRANSPORT, STEP LENGTHS AND REST TIMES IN A MOUNTAIN STREAM

This chapter is presently in peer-review for publication in the journal of Water Resources Research.

2.1 INTRODUCTION

Bedload transport is commonly quantified by measuring flux—the mass or volume of sediment moving through a given cross-sectional area of flow per unit time. Most bedload transport equations are empirical predictions of this flux [e.g., *Parker*, 1990a; *Wilcock and Crowe*, 2003]. While sufficient for many applications, bedload flux alone is an incomplete description of transport because flux does not constrain downstream migration or dispersion rates of grain populations. Additionally, bedload flux does not account for the intermittent and probabilistic nature of individual grain movement that has also long been recognized as inherent to bedload transport [e.g., *Einstein*, 1937]. Recently, a resurgence of interest has focused on incorporating stochastic factors into unified theories of transport that can explain individual grain motions, dispersion of clast populations and mass fluxes [e.g., *Schumer et al.*, 2009; *Furbish et al.*, 2012; *Martin et al.*, 2014].

The cumulative distance that an individual bedload clast travels will depend on the number of discrete movements (steps) taken, the distances traveled downstream in each movement (step lengths) and the durations of immobility between movements (rest times). The scaling of step length and rest time distributions is important because the combination of these variables controls how particles migrate and disperse and, in particular, whether their spread exhibits normal or anomalous dispersion. For a given clast population, dispersion can be described by how the variance of particle displacements (σ_X^2) changes with time as $\sigma_X^2 = \langle (X_i - \langle X \rangle)^2 \rangle \propto t^\gamma$, where X_i is the cumulative displacement distance of a given grain (i), and

brackets "⟨ ⟩" denotes the ensemble average for all bedload grains in a given population such that $\langle X \rangle$ represents the average displacement of grains over a given time. A scaling exponent γ equal to 1 indicates normal dispersion, while $\gamma \neq 1$ indicates anomalous dispersion. Subdiffusion occurs when $\gamma < 1$ and superdiffusion when $\gamma > 1$. If both step lengths and rest times follow thin-tailed distributions (such as exponential or gamma), then normal diffusion prevails [e.g., *Einstein*, 1937; *Yang and Sayre*, 1971]. Conversely, heavy-tailed step length or rest time distributions can lead to anomalous diffusion [e.g., *Schumer et al.*, 2009; *Ganti et al.*, 2010; *Voepel et al.*, 2013]. *Hassan et al.* [2013] reviewed over 60 field-based bedload tracer studies and concluded that constraints of probabilistic transport models that were based solely on the distributions of cumulative displacements measured before and after transporting events remain somewhat "speculative" due to the limited temporal and spatial measurements collected during the events. More complete field measurements of step lengths and rest durations during transporting events remain needed to understand and predict how bedload disperses downstream.

Due to the difficulty of measuring steps and rests of clasts in field settings, much of the understanding of dispersion has come from well-constrained but idealized laboratory experiments. Previous works estimating these variables have come to different conclusions. Tracking clast displacements over relatively short times (several seconds) showed superdiffusive behavior in steady-state flume experiments ($\gamma = 1.6$) [*Martin et al.*, 2012], and in a constant flow irrigation canal ($\gamma = 1.7$) [*Nikora et al.*, 2002]. Conversely, field videos of clasts tracked for several tens of seconds demonstrated subdiffusive dispersion ($\gamma \approx 0.7$) [*Nikora et al.*, 2002]. Measurements of rest time distributions during equilibrium-state flume experiments with run times up to 2 hours also suggested superdiffusive behavior ($\gamma = 2 \; to \; 2.3$) [*Martin et al.*, 2012, 2014]. Over longer time scales of a series of flash floods, *Phillips et al.* [2013] found bedload exhibiting superdiffusive behaviors (γ=1.9) from measurements of variances in cumulative displacements over time. In other field studies however, motion data collected during transporting events using active tracers (clasts embedded with various motion sensor technologies) found thin-tailed rest times and step length distributions [*Schmidt and Ergenzinger*,

1992; *Habersack*, 2001], suggesting normal diffusion rather than anomalous diffusive; γ exponents were not explicitly evaluated. Results from these and several other pioneering active tracer studies are summarized in Table 2.1.

The dependence of transport probabilities, step lengths and rest times on variable discharge are currently difficult to predict with confidence. For example, step lengths measured in steady-state flume experiments have shown both decreases [*Wong et al.*, 2007] and increases [*Lajeunesse et al.*, 2010] with higher shear stress, the latter finding being consistent with qualitative descriptions based on active tracers in natural channels [*Schmidt and Ergenzinger*, 1992; *Chacho et al.*, 1996]. During a transporting event, the duration over which measurements are made may also affect results— rest time distributions measured in previous flume studies have spanned seconds to hours in steady-state flow [e.g., *Martin et al.*, 2012], while cumulative displacement distributions measured by passive tracers in natural channels have spanned multiple transporting events to several years [e.g., *Hassan et al.*, 1992; *Haschenburger and Church*, 1998; *Bradley and Tucker*, 2012; *Phillips et al.*, 2013]. The scarcity of bedload datasets that quantify transport statistics with respect to hydrologic forcing has required that rest and step length parameters in transport models be fit empirically for each unique hydrograph period [e.g., *Schmidt and Ergenzinger*, 1992; *Bradley and Tucker*, 2012].

The above summary highlights how the current ability to predict and understand bedload dispersion is limited in part by a lack of quantitative field measurements during transporting events. With this motivation, the study had three related objectives. First, probabilities of transport, average step lengths and rest times are quantified for bedload particles during a series of snowmelt events to better understand stochastic bedload transport in natural channels. Second, these parameters are evaluated with respect to varying discharge. Third, detailed descriptions of the methods that were used to deploy radio frequency identification (RFID) and accelerometer tracer technologies are presented because data collection was challenging but ultimately successful. These technologies have great potential for quantifying and improving predictions of bedload transport in field settings.

The chapter is organized as follows. First, the study area and its snowmelt hydrology are described, then methods to produce the tracers and install stationary RFID antennas are summarized. In the subsequent results section, transport probabilities and average step lengths as functions of discharge as well as the scaling of rest time distributions are presented. Then, the discussion section explores the significance of the hydrologic dependent transport relations, shows that scaling exponents for the heavy-tailed rest time distributions appear consistent with previous lab measurements, examine the implications of the thin-tailed displacement distributions and heavy-tailed rest times on superdiffusive dispersion and highlight several recommendations for future field efforts. The study's findings are summarized in the conclusion section.

2.2 Study Site: Reynolds Creek, Idaho, USA

Reynolds Creek is a coarse alluvial channel located in the Owyhee Mountains, Idaho, USA (Figure 2.1a). The stream is in the Reynolds Creek Experimental Watershed (RCEW) and managed by the USDA-Agricultural Research Service (ARS). The tracer recovery field campaigns covered 11 km of Reynolds Creek, beginning approximately 0.7 km upstream from the Tollgate gauging station (USDA-ARS Station 116b) and ending 10.3 km downstream of the gauging station. The study's upstream boundary coincided with the location of the most upstream tracer deployment site, at a drainage area of 55 km^2. The downstream boundary corresponded to the location where field surveys ceased, several kilometers after the most downstream bedload tracer was found.

Over the study length, the channel bed consisted of coarse clasts (gravels to boulders) with occasional short bedrock reaches. Channel bed morphology was generally planar with some pool-riffle and step-pool reaches (Figure 2.1b). Most of the natural clasts represented Miocene basalt bedrock [*Ross and Forrester*, 1958; *Seyfried et al.*, 2001], and many clasts were vesicular. Field surveys and analysis of airborne LiDAR data [*Northwest Watershed Research*

Center, 2009] indicated that channel widths range from 3 to 18 m with an average of approximately 5 m. Over 100 m reach lengths, bed slope varied from 0.01 to 0.07 m/m. Wolman pebble counts [*Wolman*, 1954] were performed along 11 reaches, using 150 to 500 particles for each evaluation. The surface D_{16} and D_{50} among these reaches were similar, with respective means of 25 and 60 mm. The surface D_{84} varied more significantly over the pebble counts, ranging from 70 to 300 mm with a mean of 150 mm. Grain size distributions are further presented in Section 2.3.

Discharge has been calculated at several watershed gauging stations since the 1960s [*Pierson et al.*, 2001]. Flow is snowmelt-dominated and the highest discharges occur between March and May. Occasional high flows also occur during the winter months due to flashy rain-on-snow events. Much of the stream runs nearly dry during the late summer. The study area was downstream of the major tributaries that convey most snowmelt runoff from higher watershed elevations. Discharges calculated at Tollgate gauging station and a gauge 18 km downstream (USDA-ARS Station 36) indicated that discharges were similar along the study length [*Northwest Watershed Research Center*, 2015]. Based on the 1966 to 2014 record at the Tollgate gauge, annual peak discharges ranged from 0.5 m^3s^{-1} to 20.6 m^3s^{-1} (flood frequency analysis shown in Figure 2.1c).

Effective runoff (V_e) represents the volume of water discharge over some time span exceeding a discharge threshold for bedload transport [e.g., *Lenzi et al.*, 2004]. Figure 2.1d shows a magnitude-frequency analysis for annual effective runoff using a discharge threshold of 2 m^3s^{-1} (justified in Section 2.4.1). The variable morphology over the multiple kilometer study length precluded reporting discharge in terms of fraction of bankfull. Although beyond the scope of work presented here, HEC-RAS flow modeling along the study length indicates that transport stage ($\tau/\tau_{cr,}$ where τ is basal shear stress and τ_{cr} is the threshold of motion for D_{50} grains) generally remained below 2 for the historic record of relevant discharges [Ch. 4].

During this study, bedload transport was monitored over three snowmelt intervals: April to July 2011, October 2011 to March 2012 and March to June 2012 (Figure 2,1e). The spring

periods had longer durations and higher discharge magnitudes than the winter season, which was marked by several short rain-on-snow events. Comparing the flows from the monitored seasons with the 49 year record [*Northwest Watershed Research Center*, 2015], maximum discharges during the April to July 2011, October 2011 to March 2012, and March to June 2012 monitoring periods corresponded to annual records equivalent years having recurrence intervals of 5.0, 1.9 and 4.5 years, respectively (Figure 2.1c). In terms of effective runoff, differences in durations and discharge caused recurrence intervals to shift slightly to 5.4, 1.3 and 2.2 years, respectively (Figure 2.1d). The approximately diurnal series of bedload transporting periods that occurred in spring 2012 are further identified numerically (total of eleven) in subsequent analyses, and referred to simply as individual hydrograph events or transporting events.

2.3 Methods

2.3.1 RFID TRACER TECHNOLOGY AND PRODUCTION

RFID technologies are summarized briefly here because previous studies provide thorough explanations [e.g., *Nichols*, 2004; *Allan et al.*, 2006; *Lamarre and Roy*, 2008; *Schneider et al.*, 2010; *Bradley and Tucker*, 2012]. Capacitors inside of passive RFID tags are charged inductively when a nearby antenna briefly creates a magnetic field. Powered by the discharging capacitor, the tag immediately broadcasts its unique identification number, which is read by the antenna and recorded to a data logger. An antenna's ability to read RFID tags depends on its inductance, which is sensitive antenna size, shape and proximity to metal. Antennas are "tuned" through adjustable capacitors to balance read distance, sampling rate and power consumption. For conciseness, additional information is in the appendix regarding the production of the passive tracers and limitations of the applied RFID technologies that influenced the study's implementation.

Coarse gravels and cobbles were embedded with RFID tags that were 32 mm or 23 mm long by 3.65 mm in diameter (Figure 2.2a). The passive tracer clasts were made using two

techniques. First, a rotary hammer drill was used to bore holes in natural clasts, and tags were sealed inside with marine epoxy. The intermediate axis (*D*) for these clasts ranged from 50 mm to 160 mm, with a mean of 90 mm. However, roughly one fifth of the grains that was attempted to drill fractured, and the smaller particles fractured at a higher rate. The fracturing resulted in less than 5% of the successfully drilled rocks having intermediate axes smaller than 60 mm.

Similar to *Schmidt and Ergenzinger* [1992] and *Nichols* [2004], artificial clasts were also molded from concrete to more efficiently make smaller tracers. Fifty-five rubber molds were produced from natural river particles with intermediate axes ranging from 45 to 110 mm; the median grain size of the passive tracers approximating the channel's surface D_{50} (60 mm; Figure 2.2b). The densities of the artificial tracers (mean of 2300 kg m^{-3}) most closely corresponded to vesicular basalt clasts in Reynolds Creek, which had an average density using the ASTM C127-07 method [2007] of 2400 kg m^{-3} (range of 2100 to 2650 kg m^{-3}). The non-vesicular basalt and granite clasts had an average density of 2700 kg m^{-3} (2350 to 2950 kg m^{-3}).

2.3.2 ACTIVE TRACER TECHNOLOGY & PRODUCTION

Active tracers were molded out of concrete using methods similar to those applied to produce the artificial passive tracers. Active tracers were also embedded with an accelerometer and lead weights, in addition to an RFID tag (Figure 2.2c). Like *Tremblay et al.* [2010], relatively small (58x33x23 mm) HOBO Pendant G Data Logger accelerometers were used. The accelerometers measured ±3 g along three orthogonal axes (x, y and z) at an essentially instantaneous moment in time. Because of the accelerometers' limited memory (64 kb), accelerations could only be recorded once every 10 minutes throughout the spring 2012 season (two additional sensors instead recorded at 15 minute intervals). A change in the orientation of an axis relative to gravity changed the measured acceleration, allowing the devices to serve as motion sensors. Movement was interpreted to have occurred between two sequential measurements (i.e. sometime in the previous 10 minutes) if the accelerations on any axis differed by more than the device accuracy (±0.105 g) [*Onset Computer Corporation*, 2011].

Similar to devices used in other active tracer bedload studies [e.g., *Ergenzinger and Schmidt*, 1994; *McNamara and Borden*, 2004], the accelerometers could not distinguish between downstream transport and particle rocking in place. Additional images of the active tracers and the steps of their production are provided in the appendix.

Due to the size of the accelerometers, the intermediate diameters of the active tracers ranged from 100 to 150 mm (Figure 2.2b), such that their mean of 125 mm that approximated the D_{80} of the channel over the 2 km area where the active tracers were recovered. Average accelerometer tracer densities were 2300 kg m^{-3}, comparable to the RFID-only clasts and local vesicular basalt clasts (Section 2.3.1). After recovering the tracers following the spring 2012 season, the clasts were broken open to retrieve the accelerometers and download the data. An additional 93 accelerometers were produced and deployed in December 2012, but subsequent snowmelt discharges were too low to transport the tracers (peak of only 1.4 m^3s^{-1} between December 2012 and July 2013).

2.3.3 TRACER DEPLOYMENT

A total of 1400 passive tracers were deployed at several cross sections upstream of the Tollgate gauge (Figure 2.2d) at three different times (April 2011, October 2011 and March 2012; Figure 2.1e). The numbers of clasts in each deployment are outlined in Table 2.2. Similar to other studies [e.g., *Ferguson and Wathen*, 1998; *Habersack*, 2001; *McNamara and Borden*, 2004; *Phillips et al.*, 2013], particles were deployed by distributing the tracers on existing surface grains. With this deployment method, the tracers begin in highly mobile positions, similar to the most mobile surface grains of similar sizes (~channel D_{50} for the passive tracers and ~channel D_{80} for the active tracers). Section 2.5.3 further discusses how the initial tracer deployment may have affected transport behavior.

2.3.4 RFID ANTENNAS

2.3.4.1 Surveying tracer positions with mobile RFID antennas

Using a mobile antenna and battery-operated backpack data logger (Figure 2.1b), tracer locations were surveyed in July 2011, March 2012 and June 2012. Passive tracers were left undisturbed where found to allow future monitoring of displacements. The 0.5 m diameter antenna was tuned to give a read range of approximately 1 m for the 32 mm tags. In 2011, a Garmin GPS unit with an accuracy of ±4 m was used to measure tracer locations. In 2012, a Trimble XT GPS was used, which provided ±1 m accuracies after post-processing. The July 2011 and June 2012 field campaigns each covered the 11 km length of the channel. Due to unsafe wading conditions, the March 2012 survey only covered the 700 m reach from the study's upstream boundary to the Tollgate gauge. The mobile antenna unit provided reasonable recovery rates over significant distances (e.g., recovered 83% of the tracers traveling up to 8 km; Table 2.2). Recovery rates decreased to 50% for several of the tracer groups in the July 2012 field campaign because a high density of the tracers deposited in an excavated pool, causing significant radio interference for the mobile data logger. The pool that had been excavated by the USDA-ARS in September 2011 and filled during the subsequent transporting events; thus, the total displacement lengths presented herein exclude these tracers.

The mobile RFID antenna was also used to recover 34 active tracers in July 2012. The recovered active tracers moved 8 to 2130 m downstream from their deployment sites. Unlike the passive tracers, the active tracers had to be removed from the bed to download data. While 11 active tracers were recovered in the filled pool, I suspect that many of the unrecovered active tracers remain deposited in the filled pool because other active tracers were read in the fill, but could not be recovered due to deep burial depths and limited field time. Seven of the recovered accelerometers stopped logging prematurely, and the final logged times for these faulty sensors corresponded to high flow discharges, suggesting that the sensor failures were likely due to large

impacts that occurred shortly after their last measurements (Onset Computer Corporation, pers. comm.). Two other accelerometers had several days of systematic noise even during extremely low flow conditions, but subsequently began working again. Significant damage during the removal from the accelerometer housings prevented data retrieval from three sensors.

2.3.4.2 Tracking passing tracers with stationary RFID antennas

Three stationary RFID antennas were mounted directly onto the bed to record the timing and identification numbers of passing active and passive tracers. The antennas were made into channel bed-spanning rectangles and installed just below the most downstream deployment site with a spacing of 15 m (Figures 2.2d,e). Although individual antennas missed some tags as tracers passed by during the transporting events, the redundancy of having three antennas increased the probability that a given tag would be read by at least one antenna (percentages provided below). The antenna loops minimally protruded into the flow and were installed directly onto the mobile gravel and cobble bed by attaching the antennas onto 0.9 m steel stakes that were hammered into the bed (Figure 2.2f). The close proximity of the antennas to the metal stakes reduced read distances to approximately 0.25 m. Antennas remained in place during the spring 2012 snowmelt pulses, until the most downstream antenna dislodged during the final peak event due to significant local bed scour.

The signals from multiple tags passing an antenna at the same time can cause interference, resulting in some or all passing tags not being recorded. The likelihood of tags passing at exactly the same time was reduced by staggering tracer deployments at several cross sections 20 to 650 m upstream of the stationary antennas (Figure 2.2d). These staggered deployment locations allowed particles to be less clustered when passing through the instrumented reach. Some of the tracers placed at the deployment site nearest the antenna reach (only 20 m upstream) likely crossed antennas at similar times during the first transporting event, causing interference and some tags to pass unread by the antennas. Despite these technological

restrictions, 53% of the RFID tracers that passed the antenna reach were recorded by at least one antenna. Further, when only considering those tracers that were deployed 300 and 650 m upstream from the antenna reach, the read success increased to 88%. The closely spaced antennas were expected to also permit particle velocity estimates; however, non-systematic time drifts among the antennas' data loggers precluded these calculations. Additional antenna design considerations are summarized in the electronic supplement.

2.3.5 CHARACTERIZATION OF HYDROLOGIC FORCING

The bedload analyses presented below uses discharge (measured at the gauging station) as a direct measure of hydrologic forcing, rather than location-dependent shear stress, stream power or shear velocities [e.g., *Hassan et al.*, 1992; *Haschenburger and Church*, 1998; *Phillips et al.*, 2013]. Over the spatial extents that the tracers traveled, local channel morphology varied significantly (local bed slopes ranged from 0.005 to 0.07 m/m), giving high uncertainty to spatially averaged calculations of shear stress or related variables. Tracer positions were unknown during most of their transport history. Tracer locations were only known where they were deployed, if/when they crossed the stationary antenna reach, and where they were last deposited (i.e. where I found them during stream surveys). Because of the high degree of spatial heterogeneity within mountain channels, previous work has demonstrated that discharge-based transport relations are also appropriate for steep channels [e.g., *Rickenmann*, 2001; *Lenzi et al.*, 2006a].

2.4 Results

The results section is organized as follows. First, probabilities of transport from the active tracers are evaluated (Section 2.4.1). Then, average step lengths and rest distributions are calculated (Sections 2.4.2, 2.4.3). Finally, the transport probability and step length constraints from the active tracers are combined into an empirical function of discharge to predict mean transport distances for different groups of passive tracers (Section 2.4.4).

2.4.1 PROBABILITIES OF TRANSPORT

The motion records of the active tracers were used to calculate probabilities of transport over time and as a function of discharge (Figures 2.3a,b,c). Probabilities of transport (p_t) were evaluated for every sampling interval (t_i; i.e., every 10 minutes) over the spring 2012 hydrograph as

$$p_{t,t_i} = \frac{n_{m,t_i}}{n_{total,t_i}} \quad (2.1)$$

where n_{m,t_i} represents the number of active tracers that moved within each sampling interval, and n_{total,t_i} represents the total number of moving and stationary tracers within each interval. Similarly, constraints on transport as a function of hydrologic forcing were made by calculating probabilities of transport for given discharge intervals (Q_i) [e.g., *May and Pryor*, 2013] as

$$p_{t,Q_i} = \frac{n_{m,Q_i}}{n_{total,Q_i}} \quad (2.2)$$

where n_{m,Q_i} represents the number of accelerometer tracers that moved within each discharge interval and n_{total,Q_i} represents the total number of moving and stationary tracers within each interval. Equation 2.2 was evaluated for discharge intervals binned every 0.25 m^3s^{-1}; for example, the $5m^3s^{-1}$ bin corresponded to when discharges were between 4.875 and 5.125 m^3s^{-1}.

The probabilities of transport showed that mobility varied systematically with water discharge over time (Figures 2.3a,b,c). Probabilities of transporting for hydrograph events 4 through 11 are shown in Figure 2.3, while events 1 to 3 are presented later in this section (omitted here to minimize effects of increased mobility at initial deployment; discussed below). Full tracer mobility did not occur in any sampling period (i.e., $p_{t,t_i}<1$; Figure 2.3b). Even when discharges exceeded 6 m^3s^{-1} during the peak flow event, the maximum probability of transport was limited to only 0.30. This finding indicates that, for each sampling interval, the majority of tracers were resting. Because tracer transport was negligible when discharge was less than 2 m^3s^{-1} (i.e., $p_{t,Q_i}<0.005$; Figure 2.3c), 2 m^3s^{-1} was applied as a discharge threshold of motion in subsequent analyses. The transport probabilities are predicted reasonably well by a linear function of discharge ($R^2=0.66$; Figure 2.3c; Table 2.3) as

$$p_{t,Q_i} = 0.036Q_i - 0.06 \quad \text{for } Q_i > 2 \text{ m}^3\text{s}^{-1} \tag{2.3}$$

The scatter in the probability of transport results over the peak flows may reflect the relatively short sampling intervals over the discharge intervals (each Q_i bin exceeding 6 m^3s^{-1} had durations of less than half an hour), and hysteresis with discharge (presented below).

The stationary antenna records also showed that the passive tracers were transported past the monitored reach at times similar to when the active tracers moved (Figure 2.3d). However, the frequency that the passive tracers passed over the antennas did not demonstrate an apparent trend with water discharge (Figure 2.3e). This result is presented to demonstrate an important methodological point: the difference between Figures 2.3c,e was due to a decreasing upstream supply of passive tracers to the antenna reach over time. The supply of passive tracers to the antenna reach dwindled as the season progressed because additional tracers were not added to the stream after each transporting event, causing the majority of passive tracers logged by the stationary antennas to move past the antennas prior to the peak event.

The degree of hysteresis in transport probability between rising and falling limbs varied among different event hydrographs (Figure 2.4). Events 3, 4 and 9 showed little hysteresis, while events 5, 6, 7, 8 and 10 showed moderate amounts of clockwise hysteresis. Hysteresis was more pronounced during events 1, 2 and 11. During events 1 and 2, some of the tracers moved when water discharges were below 2 m^3s^{-1}; however, after event 2, motion rarely occurred when water discharge fell below 2 m^3s^{-1}. Event 11 exhibited the most complex hysteresis pattern, showing clockwise hysteresis when water discharge was below 6.5 m^3s^{-1} and counter-clockwise hysteresis when discharge exceeded 6.5 m^3s^{-1}. The similar hydrographs of events 4 through 10 coincided with similar transport probabilities and degrees of hysteresis, especially compared the hysteresis of events 1 and 2.

2.4.2 INDIVIDUAL STEPS AND STEP LENGTHS

The records of motion from the active tracers during spring 2012 also constrained on the total number of discrete movements (steps) each clast experienced ($N_{t,i}$; Figure 2.5a). The

average number of steps each tracer took ranged from 3 to 18 during the individual hydrograph events, and from 6 to 190 during the entire season. The tracers with fewer steps corresponded to shorter cumulative displacement distances (Figure 2.5a), suggesting that the sampling intervals of the accelerometers were sufficiently short to meaningfully constrain the transport. The number of detected motion periods represented a minimum bound on the total number of steps each tracer actually took because the accelerometers could not resolve whether more than one step was taken within a given 10 minute accelerometer sampling interval (the appropriateness of this assumption is discussed in Section 2.5.1).

The cumulative displacements of the active tracers follow a thin-tailed distribution and are well fit by a statistically-significant gamma function (Figures 2.5b,c; Table 2.3). Average step lengths for the active tracers were calculated using the minimum constraints on total motion periods as

$$\langle L_i^* \rangle = X_i / N_{t,i} \tag{2.4}$$

where X_i represented each tracer's cumulative displacement over the season. Resulting average step length values ranged from 1.1 m to 25.5 m with a mean of 12.4 m (from 9 to 252 diameters with a mean of 98 diameters). Like the cumulative distances, average step lengths also followed a thin-tailed distribution that was well described by a gamma function (Figure 2.5b,c,d; Table 2.3).

The accelerometer records supported the use of each tracer's total number of detected motion periods to estimate a maximum constraint on its average step lengths (Equation 2.4) as a reasonable assumption. Only a small fraction of the accelerometers' transport records corresponded to tracers that were in motion and accelerating at a given time of measurement. When an accelerometer was resting on the bed and not in motion at the moment of measurement, the vector sum was 1 g ±0.18 g (where the uncertainty of 0.18 g is calculated from the device accuracy as $\sqrt{(0.105\ g)^2 + (0.105\ g)^2 + (0.105\ g)^2}$); conversely, when a clast was in motion and accelerating at the moment of measurement, the vector sum deviated from 1 g ±0.18 g. Only 5.01 percent of the 10-minute accelerometer records and 3.06 percent of the 15-minute records

indicated that the tracers were moving when accelerations were measured. These numbers suggest that tracers were transported on average for approximately 30 seconds within each detected motion interval (10 min × 0.0501 and 15 min × 0.0306). This 30-second transport estimate is consistent with previous works showing that bedload transport consisted of short duration, intermittent particle movements [*Drake et al.*, 1988; *Chacho et al.*, 1994; *Emmett et al.*, 1996] and long particle rest times [e.g., *Drake et al.*, 1988; *Chacho et al.*, 1994; *Singh et al.*, 2009; *Martin et al.*, 2012].

Average step lengths also systematically increased with discharge during motion (Figure 2.5e). Because each tracer took steps at different times, the water discharges corresponding to times when each tracer moved were averaged over the season ($\langle Q_{m,i} \rangle$) and compared to each tracer's respective step length results. A linear relation between average step length and average discharge for each tracer (R^2=0.71; Table 2.3) was found as

$$\langle L_i^* \rangle = 5.6 \langle Q_{m,i} \rangle - 8.8 \quad (2.5)$$

2.4.3 REST TIME SCALING

Along with step lengths, rest time distributions are of key interest because the combination of these variables may control particle translation and dispersion [e.g., *Ganti et al.*, 2010; *Martin et al.*, 2012, 2014]. The active tracers enabled rest times (t_r) to be calculated using the durations of rest between periods of motion. The minimum rest time that could be measured was 10 minutes (i.e. the accelerometer's sampling interval). It is important to understand how the discrete sampling interval may influence the measurements of rest. To illustrate, consider an active tracer that recorded accelerations at a time of 0, 10, 20 and 30 minutes. Consider also that the clast moved at least once in the first interval (i.e., acceleration records indicated that particle orientation changed at unknown times between 0 and 10 minutes) and in the second interval (i.e., orientation changed again at unknown times between 10 and 20 minutes). If this occurred, then the accelerometer data would indicate that movement occurred at the 10 and 20 minute intervals respectively, giving a measured rest time of 10 minutes. However, a range of actual rest times

could give this simplified 10 minute result. For example, if the movements occurred at 0.1 minute and 19.9 minutes, then the actual rest time was 19.8 minutes. In another scenario, if the movements occurred at 9.9 minutes and 10.1 minutes, then the actual rest time was 0.2 minutes. In both of these cases, the rest time would be still be calculated with the accelerometers as 10 minutes. Hence, the rest times measured by the accelerometers (i.e., 10 minutes in the above example) represent an average, with the minimum and maximum possible values bounded by ± the sampling interval. The minimum sampling interval used in the scaling analysis below is thus 20 minutes.

Rest time distributions were analyzed for all eleven transporting events during spring 2012 (Figure 2.6). Additionally, rest times were also calculated from the beginning of event 4 through event 11 (325 hrs of $Q \geq 2$ m^3s^{-1}). The durations that a clast rested while discharge was below the 2 m^3s^{-1} threshold were not included in the event 4 through 11 analysis. The calculations of the exceedance probabilities of the rest times ($P(t_r > t)$) and power laws fit to the distributions to constrain the α scaling exponents ($P(t_r > t) \sim t^{-\alpha}$) were performed using the methods employed in laboratory experiments of *Martin et al.* [2012, 2014]. Distributions are considered heavy-tailed when the scaling exponent α was less than 2 [e.g., *Hassan et al.*, 2013].

Rest time distributions were heavy-tailed, with power law scaling exponents that varied with the series of hydrograph events (Figure 2.6). Rest times varied from 10 minutes (the accelerometers' sampling rate limit) up to 20 hours among the individual events, and up to 187.5 hours when events 4 through 11 were evaluated as one time series. Power law regressions were done for rest times longer than 0.3 hours because of sampling issues described above and also due to slope breaks near this duration for most of the distributions. The heavy-tailed rest time distributions gave α from 0.24 to 0.72 (Table 2.3 includes confidence bounds and goodness of fit metrics). Events 1 and 2 had higher α scaling exponents than events 3 to 8 because their rest time distributions were more dominated by shorter periods of rest than longer periods of rest

(Figure 2.6a). The subsequent events 3 through 8 had lowerα, corresponding to heavier tails (Figures 2.6a,b,c). The peak discharges during event 11 coincided with the most tracer transport (Figure 2.4o), which again steepened the tail of the rest time distribution (Figure 2.6d). The combined analysis of events 4 through 11 spanned nearly 3 orders of magnitude in rest time (from 20 minutes to 187 hours), and resulted in an α rest exponent of 0.67±0.02 (95% confidence interval) (Figure 2.6e; Table 2.3). The longest rest times in the combined analysis (Figure 2.6e) represented tracers that been immobile from event 4 until event 11.

2.4.4 CUMULATIVE DISPLACEMENTS

2.4.4.1 Passive tracers

Like the active tracers, the cumulative displacements of the passive tracers also showed thin-tailed distributions (Figures 2.7a,b). Following methods of other passive tracer studies [*Phillips et al.*, 2013; *Phillips and Jerolmack*, 2014], cumulative displacement distances were calculated from all permutations of the tracer deployments and surveys due to the limited number of field campaigns (Groups A through G; Figure 2.1e; Table 2.2). The cumulative displacements of the passive tracers were not correlated to tracer size due to the tracers' relatively narrowly range around the study area's D_{50} (mean diameter of 60 mm, Figure 2.2b). However, the displacement distribution of Group C had mean transport lengths that were 1.4 times longer than the larger active tracers (larger mean diameter of 125 mm) that were deployed and transported with Group C in spring 2012 (Table 2.2). Among the passive tracer groups, mean displacements increased linearly with effective runoff (R^2=0.98; Figure 2.7c; Table 2.3) as

$$\langle X \rangle = 0.0009 \forall_e - 64 \qquad (2.6)$$

2.4.4.2 Predictions of cumulative displacements passed on individual step statistics

In addition to using effective runoff volumes to predict mean cumulative displacements (Equation 2.6), the mean cumulative displacements of the passive tracer groups were also

employed to evaluate whether they could be reasonably predicted from discharge records (Figure 2.1e) by using the discharge-dependent probabilities of transport and mean step lengths that were recorded by the active tracers (Sections 2.4.1, 2.4.2). The mean cumulative displacement for each passive tracer group was predicted as a summation over time:

$$\langle X \rangle = \sum_{d=d_0}^{d=d_1} \langle X_{Q_p} \rangle \quad (2.7)$$

where Q_p represents the discharge in each gauge interval (15 minutes gauging station data), $\langle X_{Q_p} \rangle$ is the mean displacement estimated for each discharge interval, and d_0 and d_1 are a tracer group's respective start and end dates (times). For a given discharge interval, the mean displacements were calculated as

$$\langle X_{Q_p} \rangle = \frac{n_{t,Q_p}\langle L_{t,Q_p} \rangle + n_{r,Q_p}\langle L_{r,Q_p} \rangle}{n_{total}} \quad (2.8)$$

where n_{t,Q_p}represents the number of tracers that were transported with mean step lengths of $\langle L_{t,Q_p} \rangle$ in each discharge interval; n_{r,Q_p} represents the number of tracers that were resting with mean step lengths ($\langle L_{r,Q_p} \rangle$) of 0 m; and n_{total} represents the total number of tracers. The number of transported tracers in Equation 2.8 was calculated with the probability of transport as

$$n_{t,Q_p} = p_{t,Q_p} \times n_{total} \quad (2.9)$$

Combining Equations 2.7, 2.8 and 2.9 gives

$$\langle X \rangle = \sum_{d=d_0}^{d=d_1} p_{t,Q_p} \langle L_{t,Q_p} \rangle \quad (2.10)$$

Combining Equations 2.3, 2.5 and 2.10 gives the final empirical relation:

$$\langle X \rangle = \sum_{d=d_0}^{d=d_1} \left(0.2Q_p^2 - 0.65Q_p + 0.52\right) \text{ for } Q_p > 2 \text{ m}^3\text{s}^{-1} \quad (2.11)$$

Because Equation 2.11 is based on transport relations from the larger active tracers, the $\langle X \rangle$ prediction was then crudely adjusted to the smaller passive tracers by simply multiplying predictions from Equation 2.11 by 1.4, which is the ratio of the mean cumulative displacement observed in the passive tracer Group C to the mean displacement of the active tracers over the same time interval (Section 2.4.4.1).

Applying the step-scale model to the discharge records predicted cumulative displacements for passive (and active) tracer groups reasonably well (Figure 2.7d). Excluding

passive tracer Groups B and G, the predicted $\langle X \rangle$ results were on average only 15% lower than the observations. The mean prediction for Group B was 65% higher than its corresponding measurement, while the mean prediction for Group G was 48% lower than its measurement. Discussion regarding the deviations between the predictions and observations are presented in Section 5.2.1.2.

2.5 Discussion

The combination of active and passive tracers enabled the collection of new bedload transport data during transporting events in a snowmelt-dominated mountain stream. To our knowledge, the study's active tracer data span longer cumulative distances, times, and more sequential events than previous studies that directly measured transport probabilities and rest times [e.g., *Schmidt and Ergenzinger*, 1992; *McNamara and Borden*, 2004; *May and Pryor*, 2013] (Table 2.1). The following sections explore implications of the calculated transport statistics in the context of hydrologic forcing (Section 2.5.1), anomalous dispersion (Section 2.5.2) and field techniques (Section 2.5.3).

2.5.1 HYDROLOGIC FORCING

2.5.1.1 Transport likelihoods and length scales

The quantitative relations found between discharge and probabilities of transport and step lengths (Figures 2.3c and 2.5e; Equations 2.3 and 2.5) expand on the previous active tracer studies that were performed in mountain streams but were unable to quantify hydrologic trends in the bedload transport records [*Schmidt and Ergenzinger*, 1992; *McNamara and Borden*, 2004]. To our knowledge, the only previous probabilities of transport calculations in relation to hydrologic forcing also showed a clockwise hysteresis pattern, and was based on the transport records of active tracers that were deployed before a dam release in a larger, flatter river [*May and Pryor*, 2013]. The observed increase in step lengths with discharge (Figure 2.5e) is also

supported by similar finding from previous flume experiments using steady flow and uniform grain size [e.g., *Lee and Hsu*, 1994; *Niño et al.*, 1994; *Lajeunesse et al.*, 2010], and described qualitatively in active tracer studies [*Schmidt and Ergenzinger*, 1992; *Chacho et al.*, 1996].

Hysteresis is often observed in coarse bedload transport [e.g., *Moog and Whiting*, 1998; *Hassan and Church*, 2001; *Gaeuman*, 2010], but underlying mechanisms remain poorly understood. In a different study that also took place in Reynolds Creek, *McNamara and Borden* [2004] tracked four radio-embedded tracers and similarly noted differences in transport probabilities between rising and falling hydrograph limbs. Based on the active tracers deployed in the present study (Figure 2.4), the largest difference between rising and falling limb transport probabilities occurs where tracers are starting from unstable positions and being worked into the bed (events 1 and 2). The complex hysteresis measured for event 11 defies easy explanation with the current dataset, but hysteresis over discharges of 2 to approximately 4 m^3s^{-1} is broadly similar to the same discharge range during events 5, 6, 7 and 8. In a series of equilibrium flume experiments, *Wong et al.* [2007] found that variation in bed elevations increased with Shields stress. In Reynolds Creek, bed fluctuations may have also increased with discharge such that there was more scour on the rising limb (i.e., increased in mobility) and preferential burial on the falling limb (i.e. decreased mobility).

2.5.1.2 Predicting mean transport distances

The incorporation of hydrologic forcing into a step-scale model (Figure 2.7d; Equation 2.11) illustrates the use of active tracers as predictive tools for transport [e.g., *Chacho et al.*, 1994; *Habersack*, 2001; *McNamara and Borden*, 2004]. The similarities between the observed mean cumulative displacements of the passive tracers with the predictions from the step-based model using the active tracer relations (Figure 2.7d) demonstrates that the hydrologic-dependent transport relations captured by the active tracers (Equations 2.3 and 2.5) reasonably approximated the mean behavior of the other tracer populations during their unique hydrographs

(Figure 2.1e). The close but often under prediction may be due to i) the probability of transport relation represented by Equation 2.3 did not take into account the initially enhanced mobility due to deployment (Figures 2.4 and 2.6a), and ii) Equation 2.3 did not differentiate between slight differences in transport over the hydrographs' rising and falling limbs (Figure 2.4). The initial enhanced mobility due to deployment may also in part explain why the predicted $\langle X \rangle$ for Group B was 65% lower than the observed; the winter 2011 season only had three short rain-on-snow bedload transporting events (each <6.5 hrs) compared to the spring seasons which had series of diurnal snowmelt events.

In contrast, Equation 2.11 predicted a mean cumulative displacement for Group G that was 50% larger than observed. This over prediction may in part be due to the starting positions of the Group G tracers in spring 2012 being significantly downstream of the spatial extent of the other tracer groups (by several kilometers). These downstream reaches tended to have modestly lower gradients and wider widths compared the upstream reaches where active tracers were transported. As a result, the dependence of transport probability and average step length on discharge that is represented in Equations 2.3 and 2.5 may be less appropriate for approximating Group G's mean behavior.

2.5.1.3 Rest time distributions

A significant finding from the present work is that rest times measured continuously over multiple days and transporting events in a natural mountain channel followed a heavy-tailed power law distribution (Figure 2.6; Table 2.3). When discharge exceeded the 2 m^3s^{-1} threshold during event 4 through 11 (total of 325 hours), the rest times ranged from 20 minutes to 187.5 hours and resulted in a rest time scaling exponent was α=0.67. This scaling is in good agreement with the α exponents of 0.85 and 0.68 that were found respectively in 130 minute and 90 minute laboratory experiments that measured rest times from approximately 10 seconds to 15 minutes [*Martin et al.*, 2012]. These somewhat idealized flume runs used a narrow grain size

distributions of fine gravels and constant water discharge and sediment feed rate to drive scour, transport and deposition.

The Reynolds Creek data showed a similar scaling heavy-tailed exponent to *Martin et al.* [2012] in a natural field settings with spatial heterogeneity, broad channel bed grain size distributions, and timescales spanning multiple transporting events over days to weeks. This is an important result because previous field studies have reported rest times fit by thin-tailed exponential or gamma distributions [*Schmidt and Ergenzinger*, 1992; *Chacho et al.*, 1994; *Habersack*, 2001; *McNamara and Borden*, 2004]. In contrast, neither exponential nor gamma distributions provide statistically acceptable fits for the Reynolds Creek rest time distributions, which is seen in Figure 2.6 with the indication that thin-tailed distributions (which would occur for $\alpha \geq 2$ and the t^{-2} slope scale bar) are not consistent with the data.

Thin-tailed rest time distributions may have been found in previous active tracer field studies due to methodological and technological limitations (Table 2.1). For example, several previous studies used embedded radio transmitters that recorded motion and rest with antennas mounted along the banks of a river reach. This configuration limited the duration of measurements and the distances over which clasts were allowed to travel (approximately a couple hundred meters) before needing to be redeployed at the beginning of the monitoring reach again [*Schmidt and Ergenzinger*, 1992; *Habersack*, 2001]. Another field study that found thin-tailed rest time distributions collected rest times from a single tracer that was tracked for a couple hours [*Chacho et al.*, 1994]; the authors followed the tracer downstream by walking along stream banks with a mobile antenna. Enhanced mobility right after redeployment and before particles were worked into the bed may have led to a larger amount of short rest times in these data.

While most rest times reported in the previous active tracer studies were less than two hours, the four tracers monitored by *McNamara and Borden* [2004] in Reynolds Creek had longer rest durations of up to 19 hours that were also fit by a thin-tailed gamma distribution. While *McNamara and Borden* [2004] did not redeploy tracers, snowmelt runoff in the year of their study was minor (brief peak $Q=3.6\ m^3s^{-1}$), which resulted in the tracers having relatively

short cumulative displacements (between 7 m and 55 m). These few tracers also showed thresholds of motion to be between 1.9 m^3s^{-1} and 2.2 m^3s^{-1}, which is consistent with the constraint of 2 m^3s^{-1} based on the presented study's active tracer records. The relatively low number of tracers deployed and gaps caused by radio noise may have also affected the distributions of rest time reported by *McNamara and Borden* [2004]. Due to the season's low flows, the tracers may also have never been sufficiently incorporated into the active transport layer of the bed, which could have also influenced the distributions of rest times. In present study, only the hydrograph events 4 through 11 were used in the rest time scaling analysis (Figure 2.6) so that the clasts were worked into the bed at least to some extent (effects of deployment are further explored in Section 2.5.3).

Variable discharge as well as particle stability on the bed influenced the scaling exponents for the individual event hydrographs (Figures 2.4 and 2.6). At low discharges (less than approximately 3 m^3s^{-1}), the active tracers were far more mobile in hydrograph events 1 and 2 than in subsequent events (Figure 2.4). While an empirical discharge threshold of motion of 2 m^3s^{-1} was found for events 4 through 11 (Figures 2.3c and 2.4), events 1 and 2 had significant movement when discharge was larger than 1 m^3s^{-1} (Figure 2.4). Scaling exponents for these two initial events with higher tracer mobility were α=0.55 and α=0.64, respectively (Figure 2.6a; Table 2.3). In contrast, hydrograph events 3 to 8 and event 10 had statistically lower values of α ranging from 0.24 to 0.43. Relatively higher (i.e. less heavy-tailed) α values indicate that a systematically greater proportion of rest times were shorter rather than longer, consistent with more mobile grains. The comparatively higher α rest exponents and larger hysteresis associated with hydrograph events 1 and 2 are interpreted to have been caused by the enhanced initial mobility of the active tracers as they were gradually worked into progressively more stable locations in the bed. Conversely, rest time distributions were heavier-tailed for hydrograph events 3 to 10 with the comparable discharge ranges likely due to being in more stable positions.

More fundamentally, variable discharge can influence rest time scaling, both among and within transporting events. Event 2 had a peak discharge of approximately 4 m^3s^{-1}, which was as

high as event 4 and exceeded the peak discharges of events 3 and 5 through 10 (Figure 2.4). While clasts no doubt continued to be incorporated into more stable positions by these subsequent flows, the peak flow of event 2 peak flow was likely sufficient to move most clasts into relatively stable positions for flows of equal or lesser magnitude (i.e., events 3 to 10). As such, the heavier-tailed scaling for events 3 to 10 (mean α=0.35±0.04, where the uncertainty in this case is standard error; Figure 2.6) may reflect the rest time distributions of relatively stable particles at comparatively low transport probabilities (Figure 2.4).

Event 11 had a much higher peak discharge than the previous events (peak Q=7.9 m^3s^{-1}), during which the rest time distribution became somewhat less heavy-tailed with α=0.72 (Figure 2.6d; Table 2.3). This higher discharge also coincided with higher transport probability magnitudes (Figure 2.4o), and the 2 m^3s^{-1} discharge threshold of motion was more greatly exceeded than in previous events. Additionally, event 11 probably had on average more scour and fill and thicker active layers than the earlier events. These factors likely contributed to the distributions of rest times during event 11 to be less heavy-tailed than the previous lower flow events, which suggests that rest time scaling exponents can vary with discharge. Nonetheless, the rest scaling exponent α=0.67 from events 4 through 11 (Figure 2.6e) is interpreted as the study's most appropriate measure of rest time scaling exponents because the measurement period spanned multiple events over a range of discharges, and excluded the first three events with enhanced mobility immediately following deployment.

While all of the regressions used to constrain α rest exponents are statistically robust (R^2>0.9 and p-values less than 0.05; Table 2.3), the log-log plots in Figure 2.6 also show deviations in scaling from straight-line (i.e., power law) scaling. Factors related to the timing of the snowmelt hydrographs may have influenced the variability in local scaling. For example, the rest distribution from event 4 through 11 (Figure 2.6e) includes a clustering of rest times at approximately 20 to 25 hours. Further examination of these individual data points indicate that they correspond to several clasts that moved near the peak discharge during an event, then remained at rest until being re-entrained near a similar peak discharge during the subsequent

event. Hence, the grouping of these data points can be explained by the diurnal cycle of peak snowmelt discharges approximately every 20 to 25 hours.

2.5.2 ANOMALOUS DISPERSION

A fundamental motivation for constraining step lengths, cumulative displacements and rest times (Figures 2.5 and 2.6) is to better understand particle dispersion in mountain streams like Reynolds Creek. Previously, field and flume bedload studies have measured or assumed thin-tailed step length or cumulative displacement distributions with heavy-tailed rest times to constrain either γ dispersion scaling exponents ($\sigma_X^2 \propto t^{\gamma}$) or α rest time scaling exponents ($P(t_w > t) \sim t^{-\alpha}$) [*Martin et al.*, 2012, 2014; *Phillips et al.*, 2013]. These studies employed an hypothesis proposed by *Weeks et al.* [1996] that clasts being transported in one direction (downstream) with thin-tailed step lengths and heavy-tailed rest times should have a γ dispersion exponent and α rest exponent that are related as γ=3-α. The finding of thin-tailed cumulative displacements in this study (Figures 2.5b, 2.7a,b) were similar to previous passive tracer studies [e.g., *Hassan et al.*, 2013; *Phillips et al.*, 2013]. If the *Weeks et al.* [1996] hypothesis is valid when applied to the Reynolds Creek data, then the active tracer's thin-tailed displacements (Figures 2.5c,d) with heavy-tailed α (Figure 2.6; Table 2.3) suggest that γ should be larger than 1, predicting superdiffusive dispersion. For the best estimate α =0.67 (Figure 2.6e; Section 2.5.1.3), the corresponding γ is predicted to be 2.33. To our knowledge, the only other studies that evaluated exceedance probabilities of rest time distributions as a means of constraining dispersive scaling exponents used equilibrium flume experiments lasting approximately two hours, which also showed similar heavy-tailed rest time scaling to the Reynolds Creek datasets [*Martin et al.*, 2012, 2014] (Section 2.5.1.3). Although *Martin et al.* [2012, 2014] were not able to directly measure grain dispersion over durations longer than a couple seconds, the γ=3-α relation applied with their rest time scaling results also suggested superdiffusive γ values (ranging from approximately 2 to 2.32). In a tropical flash-flood river, *Phillips et al.* [2013] also

found superdiffusive scaling with a γ exponent of 1.9 by measuring the displacements of passive bedload tracers over time.

Repeat surveys of the tracer's positions in Reynolds Creek were not sufficient for the direct calculation of γ from the cumulative transport distributions over time. Unlike *Phillips et al.* [2013], the active tracers could not be surveyed several times during the spring 2012 flood events, and only two of the passive tracer populations could be resurveyed twice, i.e., not enough for reliable $\sigma_X^2 \propto t^\gamma$ analyses. However, rather than an increase in displacement variances over time as observed by *Phillips et al.* [2013], the displacements of the same passive tracer population during spring 2011 (Group A) and during spring 2011 through spring 2012 (Group F) showed a slight decrease (Table 2.2). This decrease coincided with the spring 2011 flows moving these passive tracers into flatter and wider channel areas that were multiple kilometers downstream from the other groups. In the Reynolds Creek study length and perhaps others, it is possible that downstream changes in channel morphology to lower gradient reaches could cause particle migration rates to decrease, which could influence dispersion measurements. For the particular 2 km reach where active tracers were transported, morphological control seems unlikely as the D_{50} did not change significantly and the plane bed morphology was fairly consistent. Nonetheless, spatial changes in grain size and reach morphology over the study length may complicate the ability to compare dispersion results over time within a channel and among channels. An example of a more complicated field setting is the Allt Dubhaig, where the dispersion of passive tracers were tracked over a 3.5 km section to examine effects of significant morphological changes on transport; over the study length, bed gradients decreased from 0.02 to 0.0002 m/m and surface D_{50} decreased from 100 mm to 20 mm [*Ferguson and Wathen,* 1998; *Ferguson et al.*, 2002]. Resulting cumulative displacements of passive tracers in the Allt Dubhaig indicated a slow-down of tracer displacements over time, though explicit γ calculations were not made.

2.5.3 FIELD METHODS

In addition to representing new field-based transport statistics, the results from the active tracers also motivate several recommendations related to methods for future tracer studies. The first point relates to the use of stationary RFID antennas and the deployment of tracers in upstream of the antennas. This study is one of the first to successfully use RFID antennas mounted directly onto the bed of a mountain channel to record the timing and identification numbers of passing RFID tracers. Previously efforts include floating RFID antennas to estimate bridge scour [*Moustakidis et al.*, 2010], and stationary antennas installed onto dams in torrents in Switzerland to constrain bedload transport (Schneider, pers. comm.). The observed improvement in antenna read efficiency to 88% by allowing the tracers to disperse over several hundreds of meters upstream of the antennas (Section 2.3.4.2) illustrates how staggering tracer deployment locations can significantly decrease tag interference and improve antenna performance.

Tracer mobility was also observed to decrease rapidly after deployment, particularly after the somewhat larger event 2 hydrograph (Figures 2.4b,c). These findings support previous bedload tracer studies that assumed tracers deployed loosely on a bed were moved into more stable positions after the first few transporting events [e.g., *Habersack*, 2001; *Liedermann et al.*, 2013; *Phillips et al.*, 2013]. If the first few events following tracer deployment are short in duration and relatively low in magnitude, then the stable positions that clasts achieve shortly after deployment are likely on the surface or near the surface.

Additionally, the tracer records also provide insights into interpretations of cumulative displacements depending on the characteristics of the first few hydrographs following tracer deployment. The Reynolds Creek results suggest that, if the initial transporting events following deployment are relatively low and not extremely long, then displacements that occur during this initial period can be relatively minimal compared to the cumulative displacements over longer times. For example, the effective runoff volumes during transporting events 1 and 2 in spring

2012 (using 1 m^3s^{-1} as a threshold; Figure 2.4b) were comparable to that of the short rain-on-snow events that moved passive tracer Group B (Figure 2.1e), which had a corresponding mean displacement of only 70 m (i.e., less than a tenth the active tracers' mean displacement during all of spring 2012; Table 2.2). Conversely, the effective runoff for the peak event in spring 2012 (Figure 2.4l) was over ten times larger than Group B's. Hence, if event 11 had occurred immediately following the deployment of the active tracers, then the initial, deployment-based instabilities affecting cumulative displacement may have been more pronounced.

The importance of the Event 11 observation is i) field studies with objectives related to the transport of active tracers would ideally monitor the movement and rest of active tracers over a series of events, rather than only over the first event following deployment, and ii) interpretations of cumulative displacements from active or passive tracers deployed loosely should be approached cautiously when the first few flood events following deployment are extremely large and have long durations. The latter implication also applies to the deployment method of replacing local grains with tracers as this disturbs the stability of the bed to an unknown degree [e.g., *Bradley and Tucker*, 2012]. Monitoring over multiple events could help decrease reporting artificially low transport thresholds, artificially high magnitudes of probabilities of transport, and artificially disparate hysteresis trends between rising and falling limbs (e.g., Figures 2.4b,c versus Figures 2.4d through 4o).

2.6 Conclusions

Accelerometer and RFID-embedded tracer clasts were used to collect rare data of coarse bedload transport statistics in a mountain stream. Increases in discharge were observed to correspond to increases in probabilities of transport, step lengths and cumulative displacement lengths. Average step lengths and cumulative displacement distributions were well fit by thin-tailed gamma distributions. Mean transport distances of the passive RFID tracers were well predicted using hydrograph records and accelerometer-based relations of step lengths and probabilities of transport with respect to discharge. Rest times measured over individual and

multiple bedload transporting events were described by heavy-tailed power law distributions, with scaling exponents that varied somewhat with event magnitude. The combination of heavy-tailed rest times with thin-tailed displacements also suggests that dispersion was superdiffusive. Monitoring particle motion in natural fluvial systems remains a crucial component in validating stochastic transport models that are based on theoretical or laboratory experiments. Expansion of similar tracking efforts in other channels remain warranted to further advance field datasets that can, ultimately, be used together to evaluate the universality of bedload transport dynamics among differing channel regimes.

Tables

Table 2.1: Comparison of several previous active tracer studies

Channel	***Lainbach, Germany***	***Phelan Creek, Alaska***	***Waimakariri River, New Zealand***	***Reynolds Creek, Idaho***	***Trinity River, California***
Type	Single thread	Single thread	Braided	Single thread	Single thread
Discharge regime monitored	Rain storms	Snowmelt	Rain storms	Snowmelt	Rain-on-snow and dam releases
Slope (m/m)	0.006-0.057	0.05	0.004	0.026	0.002
D_{50} (mm)	290-805	66	52	84	47
Study	[*Schmidt and Ergenzinger*, 1992]	[*Chacho et al.*, 1994]	[*Habersack*, 2001]	[*McNamara and Borden*, 2004]	[*May and Pryor*, 2013]
Study scope					
Tracer type	Single-frequency radio-tracers	Motion-sensing radio transmitters	Motion-sensing radio transmitters	Motion-sensing radio transmitters	Motion-sensing radio transmitters
Monitored length (m)	120	400	NR	55	800
Number of transporting events studied	6 transporting events	One 2 hr period & one 4.5 hr period	5 transporting events	2 months of monitoring[a]	3 transporting events
Number of monitored tracers	Up to 7 depending on event	1 per event	Up to 16 depending on event	4	Between 13 and 26
Tracer sampling interval	10 sec	1 sec	<30 sec	30 sec	15 min
Rest periods					
Number of observed rest intervals	47[b]	18[b]	NR	NR	NA
Distribution, including rest between events	NR	NR	Exponential	Gamma	NA
Distribution, excluding rest between events	Exponential	Exponential	NR	Exponential	NA
Step length					
Number of observed motion intervals	63[b]	29[b]	NR	NR	NA
Distribution	Exponential	NR	Gamma	NR	NA
Mean step length	19.3 m[b]	77 to 181 diameters	Reported for only 2 tracers during 1 event, 150 & 120 diameters	NR	NA
Probability of transport as a function of hydrologic forcing	NA	NA	NA	NA	Clockwise hysteresis for one of the dam releases

NR: Not reported
NA: Component not part of the study
[a]: Conducted in spring 1999, an extremely low snowmelt season for the watershed's record [*Northwest Watershed Research Center*, 2015].
[b]. Represents the total number of measurements compiled from all of the individual events monitored

Table 2.2: Summary of tracer deployments and displacement lengths

Parameters include peak discharges (Q_{peak}), excess runoff volumes (V_e), time exceeding a threshold of 2 m^3s^{-1} (t_e) and the number of tracers deployed (n).

Monitoring period	Q_{peak} (m^3s^{-1})	V_e (m^3)	t_e (days)	Group	n	Recovery rates	Displacement distances[a] Mean± stand. error[b] (m)	Median (m)	Maximum (m)	Variance (m^2)	Coeff. of variation[c]
April to July 2011	8.2	$3.55x10^6$	43.1	A	204	75%	3560±123	3760	6440	$2.31x10^6$	0.43
October 2011 to March 2012	4.5	$3.19x10^4$	0.5	B	98	83%	71±7	52.1	210	$3.81x10^3$	0.88
March to June 2012	7.9	$1.07x10^6$	15.5	C	1024	51%	1020±41	885	3350	$5.24x10^5$	0.71
				D[d]	154	90%	554±46	431	2570	$2.89x10^5$	0.98
				E[e]	81	83 %	989±102	1030	2180	$3.56x10^5$	0.61
				Active tracers	73	47%	728±111	678	2140	$3.09x10^5$	0.76
April 2011 to June 2012	8.2	$4.66x10^6$	59.1	F[f]	204	83 %	4160±115	4330	7840	$2.20x10^6$	0.36
October 2011 to June 2012	7.9	$1.10x10^6$	16.0	G[g]	98	52%	1025±97	904	2710	$4.40x10^5$	0.64

[a]. Excluding filled Tollgate pool area (Section 2.3.4.1). [b]. standard error=standard deviation/(sample number)$^{0.5}$. [c]. Coefficient of variation=standard deviation/mean. [d]. Initial locations were where Group A tracers were found in the previous survey; many of which were several kilometers downstream the other Spring 2012 tracers. [e]. Initial locations were where Group B tracers were found in the previous survey, near the deployment sites of Group C. [f]. Same population of tracers deployed in Group A, but displacements accrued over Spring 2011 through Spring 2012. [g]. Same population as the tracers deployed in Group B, but displacements accrued over Winter 2011 through Spring 2012.

Table 2.3: Regression fitting results

The resulting equations and their respective 95% confidence bounds of regression parameters (indicated by ±) and goodness of fit parameters of R^2 and p-values. The reported p-values in the regression analyses represent the result of testing the null hypothesis of no correlation at the significance of 0.05; a p-value less than 0.05 rejects the null hypothesis, suggesting that correlation between observations and regression is statistically significant. All regression evaluations were performed in Matlab.

Section	Relation	Regression results		
2.4.1	Probability of transport as a function of water discharge (Figure 2.3c)	• Equation 2.3: p_t=0.036Q-0.06 for Q≥2m^{3}s^{-1}; R^2= 0.66; 95% confidence bounds: a=0.036±0.01; b=-0.06±0.06		
2.4.2	Cumulative displacements of active tracers versus total periods of motion (Figure 2.5a)	• X_i/D_i=55$N_{total,i}$+1275; R^2= 0.61; 95% confidence bounds: a=55±20; b=1275±1550 • X_i (m)=6.9$N_{total,i}$+160; R^2= 0.61; 95% confidence bounds: a=6.9±2.5; b=160±195		
	Probability density functions for cumulative distances of active tracers (Figure 2.5c)	• $\boldsymbol{f(X_i/D_i) = \frac{(X_i/D_i)^{1.3-1}e^{-(X_i/D_i)/4550}}{4550^{1.3}\Gamma(1.3)}}$; p-value=0.0004<0.05; standard error bounds: α =1.3±0.32; β=4550±1410 • $\boldsymbol{f(X_i) = \frac{X_i^{1.3-1}e^{-X_i/565}}{565^{1.3}\Gamma(1.3)}}$; p-value=0.004<0.05; standard error bounds: α =1.3±0.33; β=565±175		
	Probability density function of active tracer step lengths (Figure 2.5d)	• $\boldsymbol{f(\langle L_i^*\rangle/D_i) = \frac{(\langle L_i^*\rangle/D_i)^{2.7-1}e^{-(\langle L_i^*\rangle/D_i)/36}}{36^{2.7}\Gamma(2.7)}}$; p-value=0.002<0.05; standard error bounds: α =2.7±0.76; β=36±11 • $\boldsymbol{f(\langle L_i^*\rangle) = \frac{\langle L_i^*\rangle^{2.7-1}e^{-\langle L_i^*\rangle/4.6}}{4.6^{2.7}\Gamma(2.7)}}$; p-value=1.8x10^{-5}<0.05; standard error bounds: α =2.7±0.76; β=4.6±1.4		
	Step lengths as a function of discharge (Figure 2.5e)	• $\boldsymbol{\langle L_i^*\rangle/D_i = 36\langle Q_{m,i}\rangle - 41}$; R^2= 0.63; 95% confidence bounds: a=36±2.1; b=41±7 • Equation 2.5: $\boldsymbol{\langle L_i^*\rangle = 5.6\langle Q_{m,i}\rangle - 8.8}$; R^2= 0.71; 95% confidence bounds: a=5.6±16; b=8.8±61		
2.4.3	Rest times distribution scaling ($t^{-\alpha}$) for rest exceeding 0.3 hours. (Figure 2.6)	• E1: α=0.55±0.04; R^2=0.96; p-value= 2E-26 • E2: α=0.64±0.05; R^2=0.96; p-value= 1E-29 • E3: α=0.24±0.02; R^2=0.95; p-value= 1E-19 • E4: α=0.31±0.02; R^2=0.97; p-value= 2E-22	• E5: α=0.25±0.04; R^2=0.92; p-value= 3E-13 • E6: α=0.29±0.04; R^2=0.91; p-value= 4E-12 • E7: α=0.40±0.04; R^2=0.94; p-value= 2E-21 • E8: α=0.43±0.05; R^2=0.94; p-value= 5E-20	• E9: α=0.56±0.04; R^2=0.96; p-value= 1E-28 • E10: α=0.31±0.05; R^2=0.94; p-value= 4E-11 • E11: α=0.72±0.04; R^2=0.96; p-value= 1E-63 • E4 to E11: α=0.67±0.02; R^2=0.97; p-value= 1E-161
2.4.4	Mean cumulative RFID displacements as a function of excess runoff (Figure 2.7c)	• Equation 2.6: $\boldsymbol{\langle X\rangle = 0.0009\Psi_e - 64}$; R^2= 0.98; 95% confidence bounds: a=0.0009±0.00015; b=64±350 • $\boldsymbol{\langle X/D\rangle = 0.013\Psi_e - 187}$; R^2= 0.98; 95% confidence bounds: a=0.013±0.002; b=187±5518		

Figures

Figure 2.1: Study site and hydrographs

(a) Reynolds Creek study area with tracer deployment and recovery locations indicated on 1 m airborne LiDAR [*Northwest Watershed Research Center*, 2009]. The most downstream deployment site is approximately 70 m upstream of the Tollgate gauging station (USDA-ARS Station 116b).
(b) Several reach images along the study length; mobile RFID antennas also shown.
(c) Flood frequency plot based on the water year's maximum annual water discharges (Q_{max}) from daily records at the USDA-ARS Tollgate gauge (1966 to 2014; [*Northwest Watershed Research Center*, 2015]). Over the 49 year record, discharges were evaluated at Tollgate every 0.1 to 24 hrs before 1994, and every 15-minutes starting in 1994.
(d) Effective runoff ($\forall_e$) representing the hydrograph volume exceeding the 2 m^3s^{-1} discharge threshold (Section 2.4.1) for each water year on record versus recurrence interval.
(e) Hydrograph during the study period with corresponding tracer groups indicated in chart below (see Table 2.2 for tracer group descriptions). Light vertical lines on hydrograph indicate when tracer groups were deployed and dark lines indicate when groups were surveyed. The discharges are calculated every 15-minutes and the 2 m^3s^{-1} discharge threshold is also indicated (discussed in Section 2.4.1).

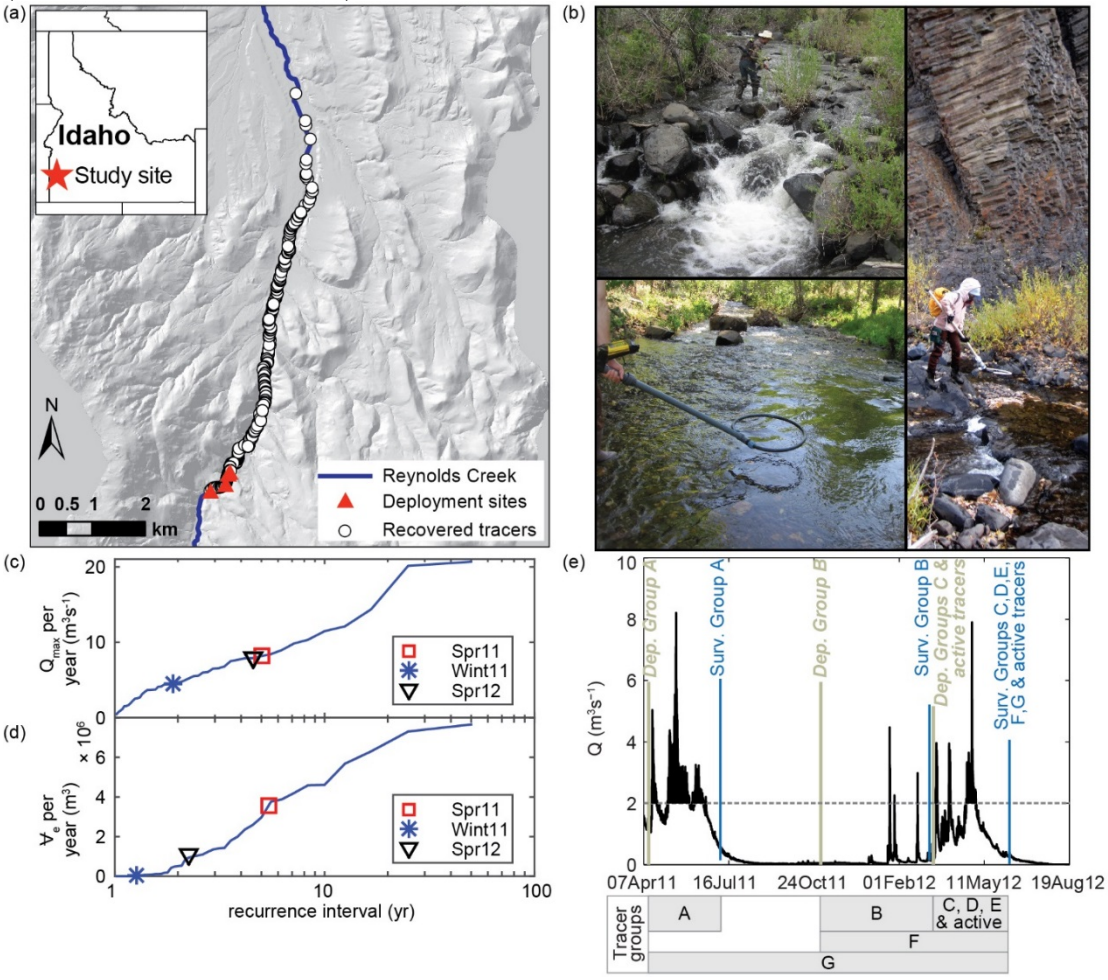

Figure 2.2: Method images of active and passive tracers and stationary antennas

(a) Coarse gravel, RFID tag (specs: 32 mm, HDX and 134.5 kHz) and protective silicon sleeve.
(b) Distribution of the b-axes, or intermediate grain diameters (*D*) for local and tracer clasts.
(c) Left: HOBO Pendant G data logger (58x33x23 mm). Right: plastic RFID disk (specs: 30 mm, HDX and 134.5 kHz).
(d) Sites of tracer deployment locations. The monitored stationary antenna reach was immediately downstream the most downstream deployment location.
(e) Site schematic of the stationary RFID antenna reach with antennas spaced 15 m apart. Antennas are submerged in image but locations indicated by the red rectangles.
(f) Portion of an installed antenna in plastic tubing that was staked directly onto the bed. The antennas consisted of insulated 10 AWG stranded copper wire that was housed in ½-inch diameter tubing to protect the wire.

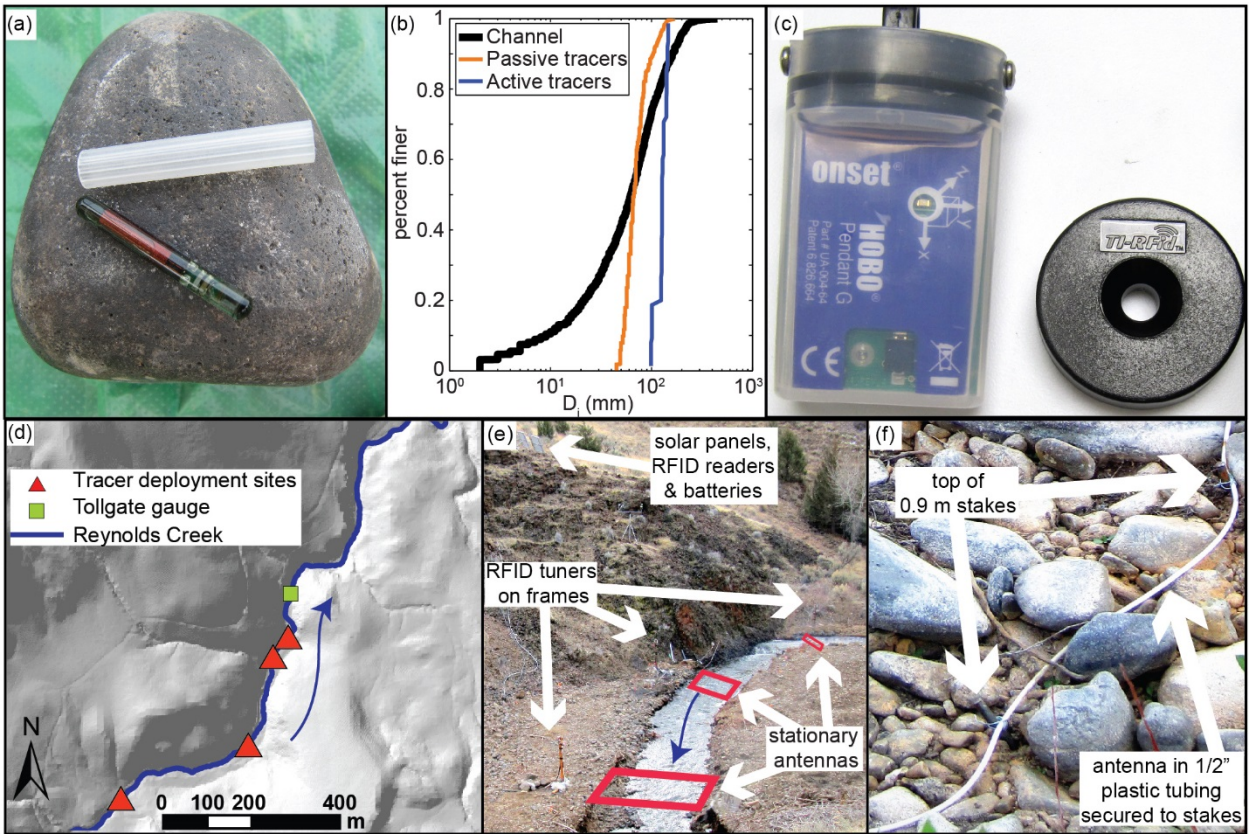

Figure 2.3: Transport statistics over time and discharge

(a) Water discharge (Q) of Reynolds Creek during spring 2012 season with events indicated above the respective diurnal peaks [*Northwest Watershed Research Center*, 2015]. Results from the first few events following deployment (events 1 through 3) are presented in Figure 2.4.
(b) Probabilities of transport (p_t) with time (Equation 2.1) over events 4 through 11.
(c) Probabilities of transport evaluated per 0.25 m^3s^{-1} discharge bin (Equation 2.2) from events 4 through 11. Linear regression results of Equation 2.3 (R^2=0.66) are presented in Table 2.3. The durations of each discharge bin (t_Q) less than 4 m^3s^{-1} exceeded 4 hours while the durations of each discharge bin larger than 6 m^3s^{-1} were less than 0.5 hours; these durations are indicated by vertical lines in the right subplots.
(d) Count of the passing passive tracers recorded by the stationary antennas during events 4 through 11.
(e) Relative frequency of the passive tracers recorded by the antennas versus discharge. Relative frequency was calculated as the number of tracers recorded per discharge bin divided by the total number of tracers read.

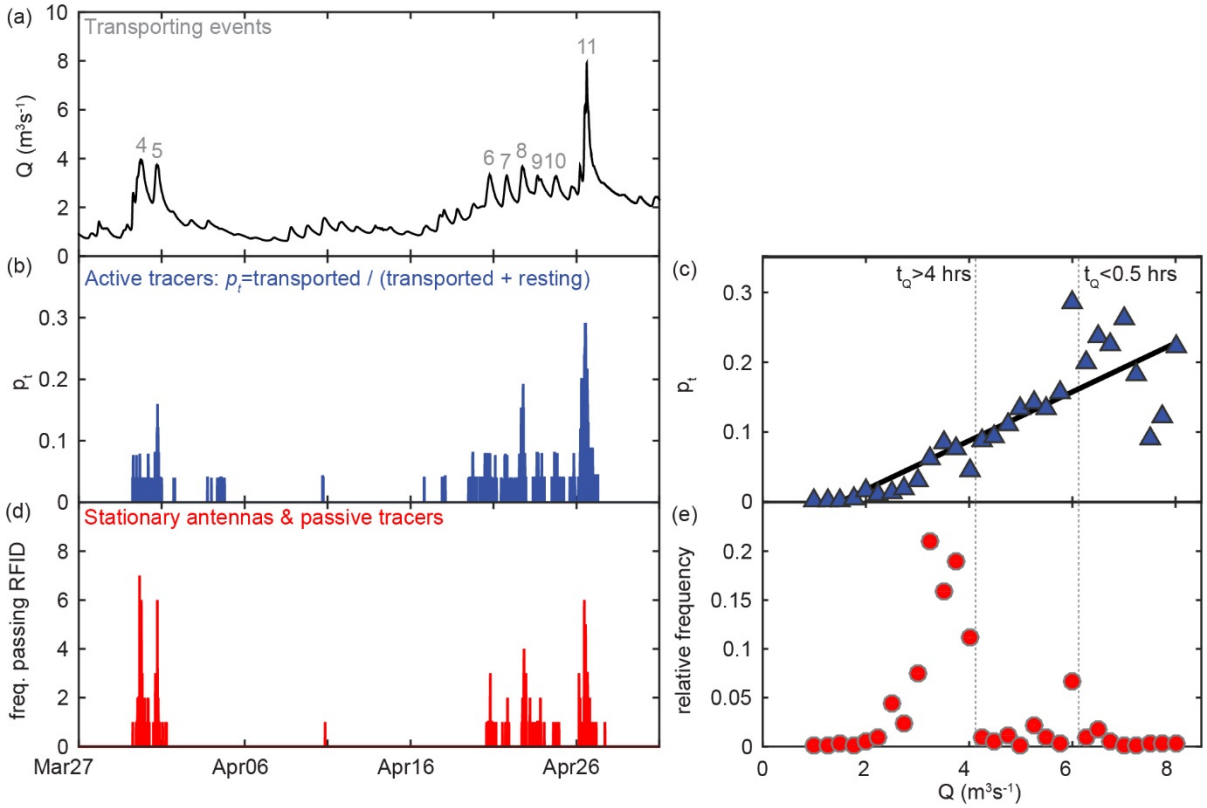

Figure 2.4: Transport probabilities over individual events

Hydrographs of the individual events are presented in the first column [*Northwest Watershed Research Center*, 2015], the active tracers' probabilities of transport (p_t) versus discharge in the subsequent columns. In event 11 (Figure 2.4o), the extents of previous subpanels are indicated by the dashed boundaries.

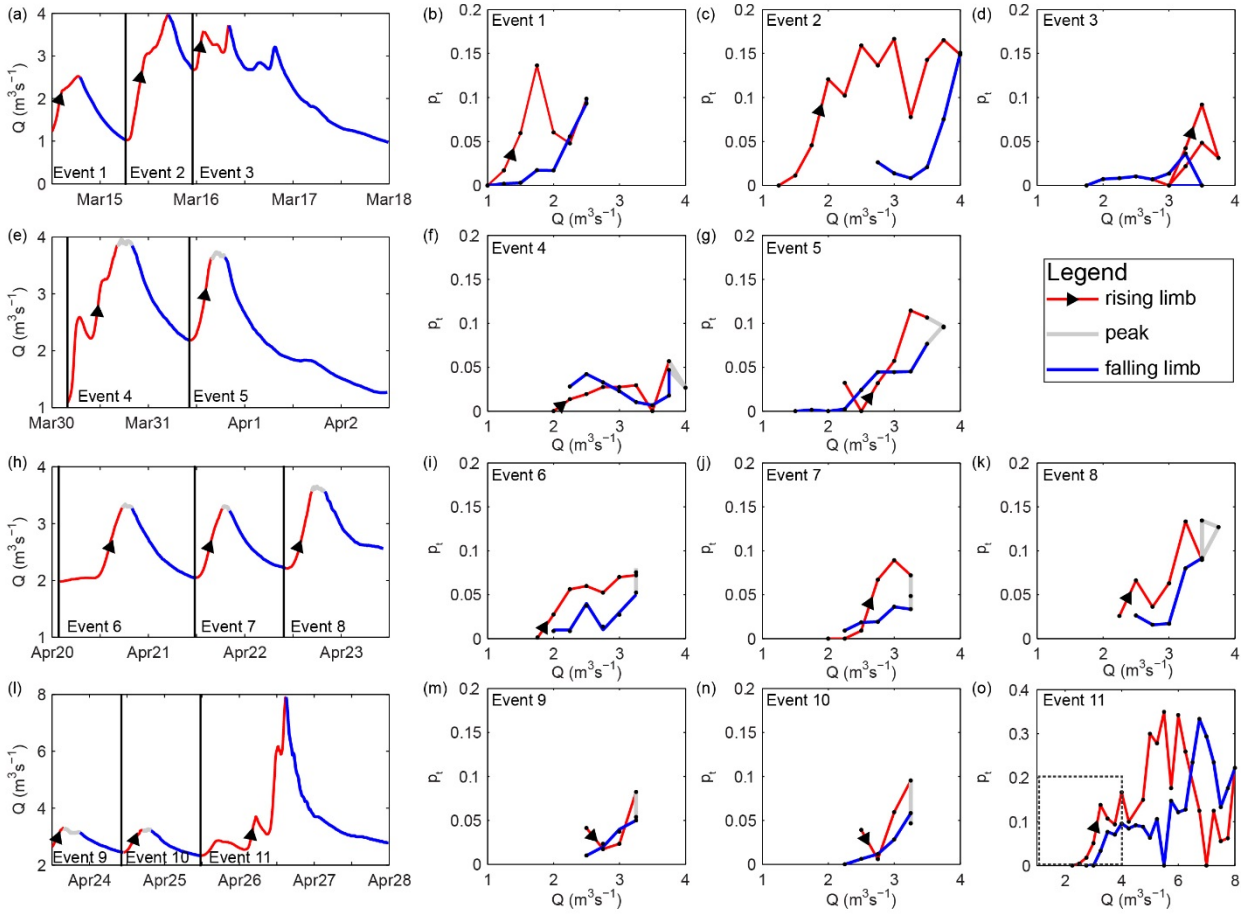

Figure 2.5: Periods of motion, cumulative displacements and step lengths

(a) Cumulative displacement distances (X_i) of the active tracers over spring 2012 normalized by tracer diameters (D_i) versus total number of motion periods detected ($N_{t,i}$). Inset: X_i versus $N_{t,i}$. Linear regression equations for plots are presented in Table 2.3 (both result in R^2=0.61).
(b) Exceedance probability plots of active tracers' X_i/D_i (open square) and mean step lengths ($\langle L_i^* \rangle$) normalized by D_i (filled circles). Average step lengths could only be calculated using Equation 2.4 for tracers with complete season-long records. Inset: Exceedance probability plots of X_i (open square) and mean step lengths ($\langle L_i^* \rangle$) (filled circles).
(c) Probability density function (PDF) of active tracers' X_i/D_i and X_i (inset) with gamma fits ($p<0.05$; equations and goodness of fit metrics presented in Table 2.3).
(d) PDF for results for $\langle L_i^* \rangle/D$ and $\langle L_i^* \rangle$ (inset) with gamma fits ($p<0.05$; equations and goodness of fit metrics presented in Table 2.3).
(e) Average discharge when each tracer was mobile ($<Q_{m,i}>$) versus $\langle L_i^* \rangle/D$ (R^2=0.63; Table 2.3) and $\langle L_i^* \rangle$ (inset; R^2=0.71; Table 2.3). Tracers shown were transported at least once after event 2.

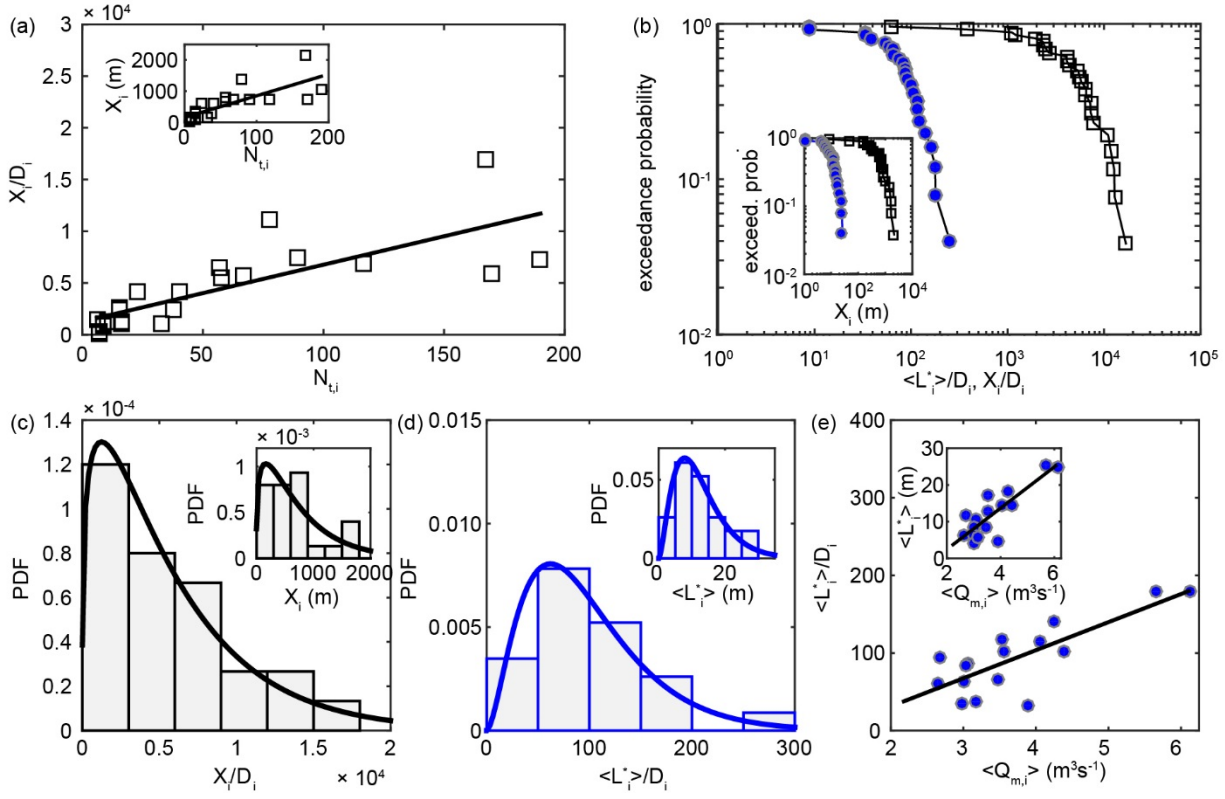

Figure 2.6: Rest times of accelerometer tracers over individual transporting events

The distributions of the active tracers' rest times (t_r) during spring 2012. Exceedance probabilities of the rest times were calculated using the methods employed in laboratory experiments of *Martin et al.* [2012, 2014] whereby the total sample number used in the exceedance probability calculations included counts of immobile clasts. The hydrograph event IDs correspond to those shown in Figure 2.4. Scaling exponents are fit for each subplot for t_r larger than 0.3 hour and goodness of fit metrics are included in Table 2.3.

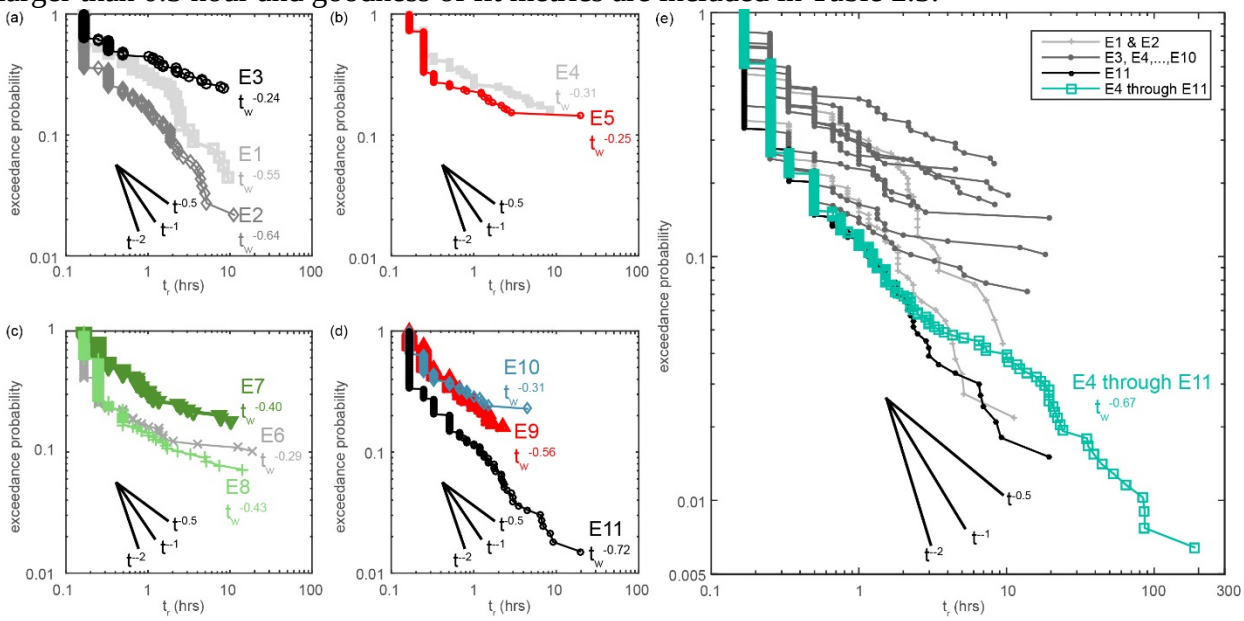

Figure 2.7: Cumulative displacements of passive tracers

(a, b) Exceedance probabilities of the RFID tracer groups' cumulative displacement distances (X_i) for the passive tracers. Groups are separated for clarity due to the similarity of groups C, D and G.
(c) Tracer group's mean cumulative displacements ($\langle X \rangle$) versus effective runoff ($\forall_e$). Here, effective runoff represents the flow volume when 2 m^3s^{-1} was exceeded (discussed in Section 4.1).
(d) Observed mean displacements versus predicted mean displacements from applying Equation 2.11 to the 15-minute hydrographs of each tracer groups. The theoretical line of observations equal to predictions is also shown.

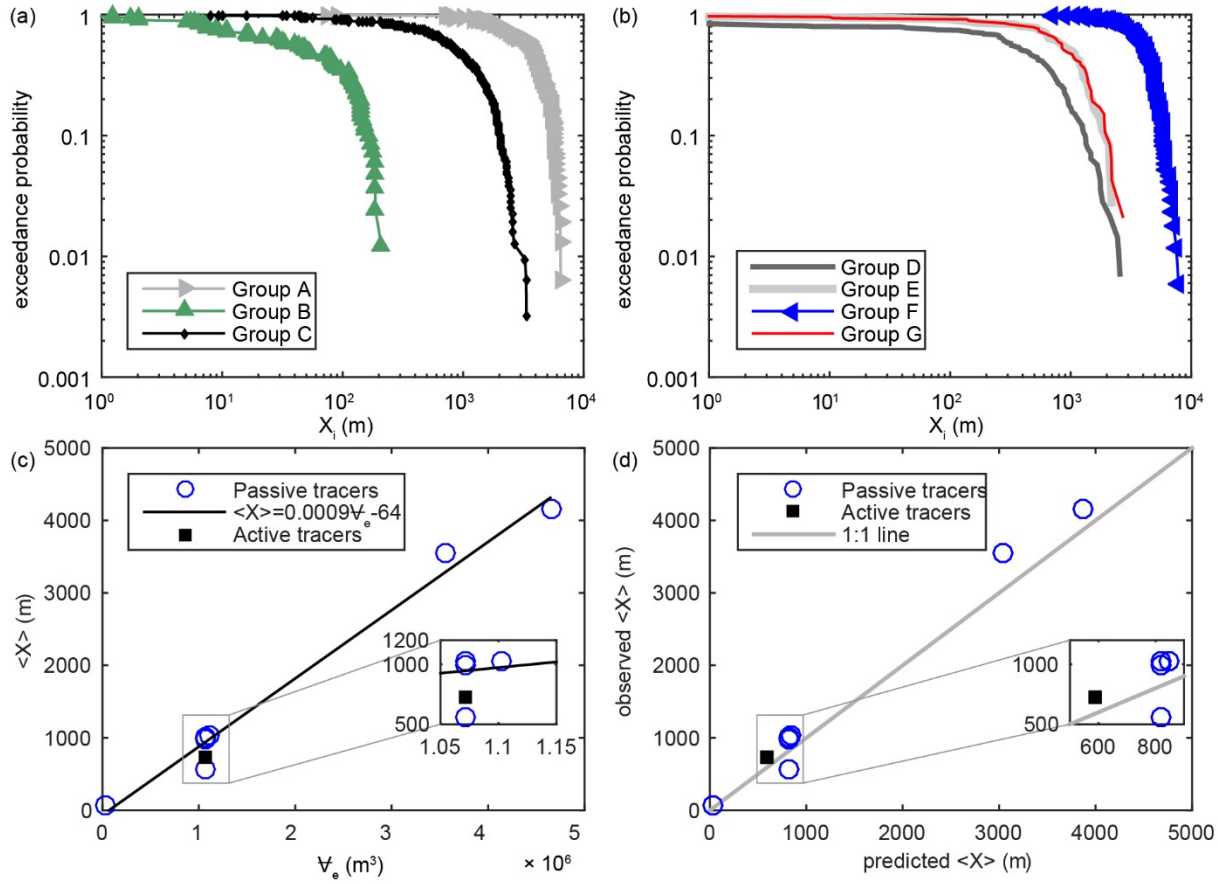

CHAPTER 3: FIELD-BASED INSIGHTS INTO THE TRANSPORT, DEPOSITION AND RE-ENTRAINMENT OF BEDLOAD CLASTS

3.1 Introduction

Understanding bedload transport, deposition and re-entrainment is necessary to predict stability and adjustments of coarse alluvial channels. Knowledge of when clast transport begins, when and where transport ceases, and when transport begins again can provide constraints on estimates of the extents to which channels are affected by flood events. However, field challenges associated with monitoring bedload have made characterizing the transport, deposition and re-entrainment of particles difficult, particularly in steep, alluvial channels. This study aims to address existing observational gaps by employing new bedload monitoring techniques.

A common means of estimating bedload transport rates is to apply empirical transport formulas [e.g., *Torizzo and Pitlick,* 2004; *Thompson and Croke,* 2008; *Wilcock et al.,* 2009]. These formulas are typically framed with transport being dependent on a given flow strength compared to the critical flow strength compared to a threshold flow strength assumed to be capable of initiation bedload motion. If all sizes of bedload clasts are capable of being entrained, then conditions of equal entrainment mobility prevail [e.g., *Ashworth and Ferguson,* 1989; *Wilcock and Crowe,* 2003; *Yager et al.,* 2012a]. If transport is more size selective, i.e., more dependent on grain size, then the thresholds increase with increasing grain size. The choice of the thresholds employed in empirical formulas is important in predicting bedload rates because nonlinear relations of flow strength and bedload cause predictions to be sensitive to errors related to threshold assumptions [e.g., *Church et al.,* 1991; *Lenzi et al.,* 2006b]. Such errors can in turn cause predictions to differ by orders of magnitude from field constraints [e.g., *Gomez and Church,* 1989; *Barry et al.,* 2008].

Constraining transport thresholds is challenging in mountain streams because field data are often unavailable and, when available, can vary depending on the methods employed. When

field data are unavailable, a critical flow value is commonly assumed for the channel's median grain size clasts [e.g., *Howard et al.*, 1994; *Andrews and Nankervis*, 1995; *Torizzo and Pitlick*, 2004]. However, these assumed values are typically not adjusted for morphological factors that influence threshold conditions, such as local bed slope [e.g., *Mueller et al.*, 2005; *Lamb et al.*, 2008; *Scheingross et al.*, 2013]. When field data are available for a reach, thresholds are frequently inferred from bedload grab samples, bedload deposited in bedload traps over a range of discharges or *a posteriori*, by measuring the largest caliber of bedload clasts that moved [e.g., *Church and Hassan*, 2002; *King et al.*, 2004; *Lenzi et al.*, 2006a; *Mao et al.*, 2008]. Limitations of these techniques include small sampler size compared to the coarse bedload transported and data only being collected during relatively low stages [e.g., *Buffington and Montgomery*, 1997; *Ashiq and Bathurst*, 1999; *Bunte et al.*, 2004].

Once a bedload particle begins to be entrained, it can roll, saltate or slide over a channel bed for short or extremely long distances before coming to rest [Ch. 2; *Drake et al.* 1988; *Schmidt and Ergenzinger*, 1992; *Habersack*, 2001]. Stochastic dispersion models interpret these displacements as a reflection of bedload grains moving and depositing in a random nature due to the multitude of compounding probabilistic channel factors affecting particle transport, such as local turbulence, varied hydrographs and burial and exposure sequences [e.g., *Einstein*, 1937; *Ganti et al.*, 2010; *Hill et al.*, 2010]. However, studies have shown that motion and deposition of bedload clasts are not entirely stochastic and can be affected by the morphologies the clasts move through. As indicated above, entrainment thresholds can be influenced by local bed slopes [e.g., *Mueller et al.*, 2005; *Lamb et al.*, 2008; *Scheingross et al.*, 2013]. The deposition of a small population of painted tracers qualitatively suggested that the deposition may preferentially correspond to lower sloped reaches [*Laronne and Carson*, 1976]. Bedload deposition has also been linked to the spacing of morphological features such as pools and bars [e.g., *Emmett et al.*, 1983; *Kondolf and Matthews*, 1986; *Pyrce and Ashmore*, 2003]. Despite these indications that morphologies influence deposition, more quantitative examinations of channel features with

respect to transport and deposition are still needed to confirm their relevance for dispersion models.

Following deposition, it is expected that for a particle to be re-entrained, the flow strength must be equal to or exceed the conditions of when the clast came to rest. This expectation is largely based on the pioneering work of *Hjulström* [1935], who performed flume experiments with uniform grains. He found that the velocities required to entrain a particle from rest were higher than those required to keep transporting the particle, and that velocities that allowed for deposition were lower than those required to entrain and transport a particle. Factors that may contribute to this also being observed in mixed-grain settings may include the structure of the bed surface adjusting after deposition, becoming stronger due to imbrication or clustering and thus requiring larger forces to subsequently remove a clast from the bed. [e.g., *Hassan and Church*, 2000; *Papanicolaou et al.*, 2003; *Strom et al.*, 2004]. Another factor may be related to burial after deposition, because scour at larger thresholds may ultimately re-entrain the particle [*Wong et al.*, 2007]. *Turowski and Rickenmann* [2011] used bedload impact sensors in steep alluvial streams and found that the discharge corresponding to the end of nominal transport for an event was equal to or exceeded the discharge corresponding to the initiation of transport in a subsequent event. Due to the scarcity of field-based datasets, additional testing is needed to evaluate the universality of *Hjulström's* [1935] theory.

New datasets are presented here that characterize the transport, deposition and re-entrainment of bedload clasts in a mountain stream. The fundamental questions that motivate the analyses are i) To what extent are transport thresholds dependent on bedload grain size? ii) How well does the utilization of single thresholds predict transport conditions? iii) Are transport and deposition correlated with particular stream morphologies and hydraulic conditions? and iv) Are flow conditions when a clast is re-entrained always equal to or larger than at deposition? These questions are evaluated by analyzing records of particle mobility that were collected over length scales spanning from several clast diameters to multiple kilometers, and over time scales spanning from less than a second to multiple seasons. Applied technologies included passive

tracers that were gravels and cobbles embedded with Radio Frequency Identification (RFID) tags, active tracers that were cobbles embedded with accelerometers, in-stream RFID antennas and numerical flow modeling using the Hydrologic Engineering Centers River Analysis System (HEC-RAS) [*U.S. Army Corps of Engineers*, 2010]. Airborne digital elevation models (DEMs) and HEC-RAS computations were used to characterize channel morphologies and hydrologic conditions such as bed slopes, widths, flow depths, shear stresses stream power and flow velocity.

This chapter is organized as follows. First, the study area and methods of tracer deployment, stationary antennas, and flow modeling are described. Then, results show the flow conditions corresponding to when tracers were transported past the RFID antenna reach, flow conditions and channel morphologies when and where the tracers deposited, and comparisons of discharges when tracer deposition and re-entrainment occurred. The subsequent discussion section explores the significance of identifying thresholds of motion over time and compares the finding with to more traditional field techniques, and examines the implications of the findings that width and slope influence transport and that thresholds covered a range of conditions.

3.2 Methods

3.2.1 FIELD SITE

Reynolds Creek is a snowmelt dominated tributary to the Snake River and is located in the Owyhee Mountains in southwest Idaho. The USDA-Agricultural Research Service (USDA-ARS) manages Reynold Creek and the surrounding land as part of the Reynolds Creek Experimental Watershed. Reynolds Creek cuts through granitic and basaltic formations [*Ross and Forrester*, 1958; *Seyfried et al.*, 2001]. The 11 km study area was located downstream of the tributaries that deliver the snowmelt discharge to the channel (Figure 3.1a). Over the study area, channel morphologies were mostly plane-bedded interspersed with pool-riffle, step-pool and unorganized sections of large boulders (Figures 3.1b-d).

Pebble counts collected at 11 reaches along the study length [*Wolman*, 1954] were used to calculate grain size distributions (Figures 3.1a,f). Median diameters (D_{50}) over the sites ranging from 42 mm to 90 mm. The beds consisted predominantly of gravels and cobbles, many of which were composed of vesicular basalt. Samples of local vesicular surface grains had mean densities of 2400 kg m^{-3} [Ch. 2]. Samples of local non-vesicular clasts had mean densities of 2700 kg m^{-3}.

Channel geometries were constrained with measurements from the field and DEMs. Bankfull widths measured during the field campaigns had a median of 5.10 m, mean of 5.42 m, standard deviation of 1.73 m and standard error of 0.12 m (among 208 cross sections across the study area). The extents of bankfull widths were estimated based on the stream-to-floodplain transition when floodplains were present [e.g., *Nolan et al.*, 1987]. At cross sections with one bank consisting of bedrock cliffs, widths were measured based on the elevation of the estimated floodplain on the opposing bank. Cross sections of channel elevation were extracted every 2 m over the study area using a 1-m DEM based on airborne LiDAR over the watershed [*Northwest Watershed Research Center*, 2009]. The 2009 LiDAR was acquired in November when stream flow was low or absent (shown as background of Figure 3.1a). Longitudinal profiles extracted from the DEM indicated that channel slopes averaged over moving windows of approximately two channel widths (i.e., 10 m) varied from approximately 0.005 to 0.07 m/m (mean 0.026 m/m; median 0.022 m/m; Figure 3.1g).

Discharges were calculated every 15 minutes at the "Tollgate" gauging station (USDA-ARTS gauge ID 116b) (Figure 3.2) [*Northwest Watershed Research Center*, 2015]. Bedload transport was monitored over the spring 2011, winter 2011 and spring 2012 snowmelt seasons. The spring 2011 snowmelt lasted the longest of the monitored seasons, with high flows spanning several months. The winter 2011 season consisted of several short, rain-on-snow floods. The discharges at Tollgate gauging station were similar to the gauge that was 18 km downstream (USDA-ARS gauge ID 36), indicating that the discharge along the entire study length could be modeled with the Tollgate records.

3.2.2 BEDLOAD TRACERS

The bedload-tracer technologies utilized in the study are only briefly summarized here because they have been detailed previously [Ch. 2]. Passive tracers consisted of natural and artificial gravel and cobble particles that were embedded with RFID tags, similar to other bedload tracer studies [e.g., *Nichols*, 2004; *Bradley and Tucker*, 2012; *Phillips et al.*, 2013]. The intermediate diameters of the passive tracers ranged from 45 mm to 160 mm, with a mean of 60 mm. The artificial clasts consisted of concrete with mean densities of 2300 kg m^{-3}, comparable to local vesicular basalt clasts (Section 3.2.1). The tracers were deployed in April 2011, October 2011 and March 2012 (Figure 3.2). Tracer positions were later located using mobile RFID antennas in low flows during July 2011, March 2012 and June 2012 and locations were recorded with GPS units (accuracies of ±1 m to ±4 m). Flows were unsafe for wading when the discharges exceeded approximately 0.3 m^3s^{-1}.

Active tracers made of artificial cobbles embedded with Hobo 3G accelerometers and RFID tags were also deployed in March 2012 and recovered in July 2012. Comparable to the artificial RFID tracers and local vesicular clasts, the mean densities of the accelerometer clasts were also 2300 kg m^{-3}. The study conducted by Tremblay et al. [2010] assisted in the design of the active tracers. The accelerometers performed as motion sensors during diurnal transporting events, logging accelerations every 10 or 15 minutes throughout the season (example shown in Figure 3.3). The sampling intervals of the accelerometers were prescribed by their limited 64 kb memory and the necessity to record motion over several months of potential snowmelt flows.

The passive and active tracers that were deposited in an excavated pool were excluded from the channel morphology analyses presented below. In September 2011, the USDA-ARS excavated and area just upstream of the Tollgate gauge to improve the gauge's performance. The excavation removed approximately 230 m^3 of bulk sediment and vegetation (mostly willows) that had accumulated in the gauge pool and adjacent point bars just upstream of the Tollgate gauge (Zane Cram, personal communication). After the excavation, the pool continued

to create a backwater effect and the area adjusted significantly during subsequent flood events. The DEM used to build the HEC-RAS models (Section 3.2.4) no longer represented the pool area.

3.2.3 STATIONARY RFID ANTENNAS

In addition to the active tracers, three in-stream RFID antennas also collected bedload transport data during the spring 2012 flood events (Figure 3.4). Stationary antennas were installed directly onto the channel bed at a reach that was approximately 70 m upstream from the Tollgate gauging station. Multiple antennas were installed to minimize the risk of missing a passing tracer [Ch. 2]. The slope over the 30 m reach was 0.018 m/m. Bankfull discharge was estimated as 2.5 m^3s^{-1} at the reach using a series of time lapse pictures over a range of discharges. It is expected that this approximates bankfull discharge at most sites along the stream [discussed further in Ch. 4].

Each of the antennas recorded the time that passive tracers passed through the reach, at a resolution of 0.2 seconds. Antennas spanned the channel width and were spaced 15 m apart from each other. Due to non-systematic drifts in the time settings of the antenna data loggers (< 5min), tracer velocities through the reach could not be calculated. One antenna dislodged during the final and peak event of April 26, 2012 due to local bed and bank scour. The flume experiments of Schneider et al. [2010] assisted in the design of the stationary RFID antenna system used in this study.

3.2.4 HEC-RAS FLOW MODELING

3.2.4.1 Model description and computations

In order to complement the field datasets, HEC-RAS was employed to better understand the hydraulic conditions when tracers were transported and deposited. HEC-RAS is a flow modeling tool developed by the U.S. Army Corps of Engineers. Cross-sectional geometries over

a 14 km length of channel were extracted from the 1-m DEM every 2 m using HEC-GeoRAS, an add-in extension for ArcGIS, and then imported into HEC-RAS [e.g., *Snyder,* 2010]. The 11 km study area was located in the middle of the 14 km model, such that there were additional 1.5 km lengths of channel modeled in HEC-RAS at both the upstream and downstream boundaries of the study area.

Steady-state flow conditions were modeled with discharges from 0.3 to 21 m^3s^{-1} in 0.1 m^3s^{-1} intervals (208 models). For each modeled discharge (Q_m), HEC-RAS computed the energy-balanced water surface elevations at each cross section by using a step backwater method based on energy losses (determined by contraction and expansion coefficients) and resistance (determined by Manning's *n*) [e.g., *Goode and Wohl,* 2010]. The upstream and downstream boundary conditions were based on critical depths (discussed further in Section 3.2.4.2), and expansion and contraction coefficients were kept to their respective default values of 0.3 and 0.1, similar to other mountain stream models that have utilized HEC-RAS modeling [e.g., *Chin*, 2003; *Thompson and Croke*, 2008; *Scheingross et al.*, 2013].

Form drag was specified with a Manning's *n* of 0.05 over the upland section based on a previous bedload study in the section [*McNamara and Borden,* 2004]. A Manning's *n* of 0.04 was used over the slightly flatter and finer-textured section downstream, based on comparisons to other natural streams [*Chow*, 1959]. The Manning's *n* values were kept constant with discharge due to a lack of water surface measurements for calibrations. In any case, the results were fairly similar whether the constant Manning's *n* was set as 0.04, 0.05 or 0.06. For example, when the model was run with *n*=0.04 versus *n*=0.06 over the upland section, the computed flow depths only differed on average by 0.04 m when Q_m=2 m^3s^{-1} and by 0.05 m when $Q_{m=}$4 m^3s^{-1}. Additionally, computed widths differed only by 0.75 m when Q_m=2 m^3s^{-1} and by 0.79 m at 4 m^3s^{-1} when $Q_{m=}$4 m^3s^{-1}.

Flow strength was characterized for each modeled discharge based on shear stress (τ_{Q_m}), unit discharge (q_{Q_m}), stream power (Ω_{Q_m}) and flow velocity (U_{Q_m}) calculations in HEC-RAS

[*Brunner*, 2010]. The HEC-RAS solution of the water surface elevations determined the cross section's hydraulic radius (R_{Q_m}), which was then used to calculate cross-sectional averaged shear stress as

$$\tau_{Q_m} = \rho g R_{Q_m} S_{Q_m,EGL} \quad (3.1)$$

where ρ is the density of water (assumed to be 1000 kg m^{-3}), g is acceleration due to gravity (9.81 m s^{-2}) and $S_{Q_m,EGL}$ is the HEC-RAS calculated slope of the energy grade line. Unit discharge was computed with wetted width (w_{Q_m}) as

$$q_{Q_m} = \frac{Q_m}{w_{Q_m}}, \quad (3.2)$$

Stream power was calculated in HEC-RAS as

$$\Omega_{Q_m} = \tau_{Q_m} U_{Q_m} \quad (3.3)$$

3.2.4.2 Performance based on field constraints

The HEC-RAS computed Froude numbers (*Fr*) suggested that the models approximated natural flow conditions. The non-dimensional Froude number represents the ratio of inertial to gravitational forces as

$$Fr = \frac{U_{Q_m}}{\sqrt{gh}} \quad (3.4)$$

where *h* is average cross-sectional flow depth. In agreement with expectations for steep and rough channels [e.g., *Jarrett*, 1984; *Grant*, 1997], the HEC-RAS models indicated that subcritical flow conditions (*Fr*<1) dominated the study area during the floods. HEC-RAS predicted supercritical flow only at a few, short lengths. For example, at the highest discharges modeled, supercritical conditions persisted only over an average of three consecutive cross sections (i.e., 6 m). The 1.5 km model buffers both upstream and downstream of the study area caused model flow conditions over the study area to be unaffected by any boundary conditions chosen for the models, such as forcing a critical depth at the boundaries (*Fr*=1), normal depths from local bed slope (i.e. uniform flow) or a range of water surface elevations.

Water surface elevations were unavailable to calibrate the model's Manning *n* roughness coefficients. However, comparisons of 208 measured and modeled flow widths at the lower discharges indicated that the roughness values chosen approximated field conditions. For example, the widths estimated during field surveys and from the model at Q_m=1 m^3s^{-1} differed on average by only 0.58 m with a standard error of 0.15 m (median was 0.42 m). The average measured width was 5.42 m (Section 3.2.1).

3.2.4.3 Application in transport and deposition analyses

This study employed HEC-RAS computations for three sets of analyses. First, HEC-RAS was used to simulate transport conditions for the times when the tracers passed the stationary antennas. The discharges corresponding to the antenna records were used to calculate corresponding shear stresses and unit discharges. Since the antennas also recorded the unique identification numbers of each RFID tag and the tracer diameters (D_i) were known, shear stresses were normalized with grain weight per area to calculate Shields numbers (τ^*_{i,Q_m}) corresponding to transport:

$$\tau^*_{i,Q_m} = \frac{\tau_{Qm}}{(\rho_s - \rho)gD_i} \quad (3.5)$$

where ρ_s represents the density of sediment. The densities of passive and active artificial tracers were approximated as 2300 kg/m^{-3} and the densities of the natural passive tracers were approximated as 2650 kg/m^{-3} (Section 3.2.2).

The second analysis that utilized the HEC-RAS computations characterized the channel sections where passive tracers deposited, compared to sections without tracer deposition. The deposition locations were based on the tracer locations observed during the three field surveys. Due to the variation in channel morphology over the study area and the accuracy of the GPS units (± 1 m to ±4 m; Section 3.2.2), the channel was discretized into 10 m sections (approximately two average channel widths). HEC-RAS calculations were averaged over each 10 m section to compare areas with and without tracers. Flow was modeled at stages of 2 m^3s^{-1}

and 4 m^3s^{-1} because the times and flows when the tracers deposited were unknown. The 2 m^3s^{-1} and 4 m^3s^{-1} discharge conditions were chosen as constraints because critical entrainment threshold at one reach was estimated as 3 m^3s^{-1} (detailed below in Section 3.3.1).

The third use of HEC-RAS models involved the deposition conditions of the active tracers. Unlike the passive tracers, the times when the active tracers were last deposited were well constrained by the last record of movement for each accelerometer. Deposition positions and discharges when deposition occurred (Q_{dep}) were used to constrain the shear stresses in HEC-RAS at the deposition place and time, and to calculate corresponding Shields numbers ($\tau^*_{dep,i}$). Similar to the deposition analyses for the passive tracers, the shear stresses were averaged over 10 m.

3.3 Results

In the following section, thresholds of motion are first shown based on records of transport from the passive tracers crossing the stationary antenna reach. Results related to channel morphology and hydrologic conditions during deposition are subsequently presented based on passive and active tracers datasets. Comparisons of discharges during re-entrainment are then compared to those of deposition using the active tracers.

3.3.1 TRANSPORT AND HIDING FUNCTIONS

The times when the passive tracers crossed the stationary antennas were recorded during eleven diurnal snowmelt events (Figure 3.5a). The peak discharges during events 2 through 11 exceeded the 2.5 m^3s^{-1} bankfull estimate. The first event had a peak discharge of 2.5 m^3s^{-1}, the second through tenth events had peak discharges ranging from 3.2 m^3s^{-1} to 3.9 m^3s^{-1} and the eleventh event had a peak discharge of 7.9 m^3s^{-1}. The HEC-RAS computed Shields numbers and unit discharges associated with tracers passing the antennas were compared to relative grain size (D_i/D_{50}) by fitting hiding functions to the datasets (Figures 3.5b-e; discussed further below). The relative grain sizes of the antenna recorded tracers ranged from 0.75 to 2.4 for the artificial

tracers and 1.62 and 2.73 for the natural tracers. Fewer records exist for the natural tracers because most of the tracers deployed prior to the spring 2012 season were artificial [Ch. 2]. For the artificial tracers, the Shields numbers and unit discharges corresponding to the initial three events included values that were slightly lower than the subsequent events (Figures 3.5 b,c).

Hiding functions were constrained by fitting power law regressions to the minimum Shields numbers ($\tau^*_{c,i}$) and unit discharges ($q_{c,i}$) for each tracer size (Figures 3.5b-e; Table 3.1) [e.g., *Buffington and Montgomery*, 1997]. Hiding functions can have the form of

$$\tau^*_{c,i} = \tau^*_{c,50}\left(\frac{D_i}{D_{50}}\right)^b \quad (3.6)$$

and

$$q_{c,i} = q_{c,50}\left(\frac{D_i}{D_{50}}\right)^c \quad (3.7)$$

where $\tau^*_{c,50}$ and $q_{c,50}$ are the critical Shields number and unit discharge for the D_{50} sized grains, respectively. Values of b=-1 and c=0 indicates equal entrainment mobility. Events 4 through 11 were used for these calculations to minimize effects of initial deployment [detailed in Ch. 2].

The hiding functions were fit separately for the artificial and natural tracers due to the different densities. Despite the differences in densities, the regressions for the hiding functions of the two tracer groups were within the uncertainty of each other. The hiding functions for the artificial tracers resulted in $\tau^*_{c,50}$=0.072±0.002 and b= -0.965±0.061 (correlation p-value<0.05; R^2=0.97) and $q_{c,50}$=0.184±0.012 and c=0.109±0.156 (correlation p-value>0.05; R^2=0.06; RMSE: 0.025). Uncertainty here represents 95% confidence bounds around the parameters, and correlation p-value<0.05 indicates that the correlation between the observations and the regression fits were statistically significant at the 95% confidence level. The $\tau^*_{c,i}$ function was significant, but the $q_{c,i}$ function was not. The discharges corresponding to the $\tau^*_{c,50}$ and $q_{c,50}$ for the artificial tracers are 3.1 m^3s^{-1} and 3.0 m^3s^{-1}, respectively. The hiding functions for the natural tracers resulted in $\tau^*_{c,50}$=0.064±0.007 and b= -1.130±0.160 (correlation p-value<0.05, R^2=0.95) and $q_{c,50}$=0.250±0.074and c= -0.312±0.440 (correlation p-value>0.05; R^2=0.17; RMSE: 0.11). Again, the $\tau^*_{c,i}$ function was significant, but the $q_{c,i}$ function was not. The discharges

corresponding to the $\tau^*_{c,50}$ and $q_{c,50}$ for the natural tracers are 4.8 m^3s^{-1} and 5.9 m^3s^{-1}, respectively. Combining the minimum records from the artificial and natural records, the hiding functions resulted in $\tau^*_{c,50}$=0.072±0.003 and *b*= -1.175±0.081 (correlation *p*-value<0.05; R^2=0.95) and $q_{c,50}$=0.100±0.117and *c*=0.184±0.010 (correlation *p*-value>0.05, R^2=0.06; RMSE: 0.14).

3.3.2 DEPOSITION

3.3.2.1 Channel morphologies and flow conditions at deposition locations

Sections with and without tracer deposition were compared based on local bed slope and HEC-RAS computed wetted width, flow depth, shear stress, stream power and flow velocity. While these parameters clearly are inter-related, they were chosen for comparison in case the combination of values (e.g., stream power, Equation 3.3) or separation (e.g., shear stress and velocity) affected results. Due to the variability in distributions of tracers along the channel and in average bed slopes over hundreds of meters (e.g., the flatter section upstream from the Tollgate gauge and the steeper section just downstream the Tollgate gauge, Figure 3.1g), the study area was delineated into seven zones denoted A through G (Figure 3.6a; Table 3.2). The zones were delineated so that each zone contained more than 30 deposited tracers and had lengths of less than 1 km. The criteria of mean tracer concentrations caused the analysis to cover approximately 6 km of channel and led to a few sections between zones not to being evaluated.

The average slope of each zone was calculated with linear regression using the bed elevations over the entire zone. Within each zone, local bed slopes (i.e. not the whole-zone averages) were then calculated with linear regression over 10 m moving windows to better capture smaller features such as pools, steps and plane-bedded reaches that were not resolved in the zonal slope calculations. Within each zone, channel slopes were relatively uniform. Zone C had the steepest overall slope (0.060 m/m), and zones A and G had the flattest slopes (0.02 m/m).

Each 10 m section within the seven zones was evaluated as either having or not having tracer deposition. Within each zone, the corresponding bed slope, wetted widths, flow depths, shear stresses, stream powers and flow velocities were compared between the sections with and without tracers. Changes in these six parameters with respect to the upstream section were also compared to assess whether deposition was affected by longitudinal differences, e.g., assessing if the downstream sections of expansion corresponded to deposition (dw/dx, where dx=10 m). Additionally, changes in the parameter with respect to the discharge at each section were calculated to determine whether deposition was influenced by differences in how the hydraulic conditions varied, e.g., determining if the sections where the wetted widths receded more rapidly as discharge fell corresponded to deposition (dw/dQ_m, where dQ_m=4m^3s^{-1} – 2 m^3s^{-1}). The 17 parameters explored in the deposition analysis are listed in Table 3.3 and Table 3.4.

Of the parameters evaluated, channel width was the only one that showed statistically significant differences between the sections with and without tracer deposition for the majority of zones (Table 3.3; Figures 3.6b,c). Table 3.3 lists all resulting *p*-values basef on nonparameteric Wilcoxon Rank-Sum tests. Table 3.4 summarizes the percent differences between in the medians of each parameter, comparing sections without tracers to sections with tracers. Both the 2 m^3s^{-1} and 4 m^3s^{-1} models indicated that tracers deposited at wider sections within zones A, B, C and G (Rank-Sum *p*-value<0.05, where *p*-value <0.05 indicates a rejection at the 95% confidence of the null hypothesis that the samples were from the same population). Rank-sum comparisons within zones A, B and G also showed that tracers deposited in sections where the wetted widths receded more rapidly as discharge fell (i.e., dw/dQ_m results). While not statistically different from the sections without tracers (i.e., Rank-Sum *p*-value >0.05), zones A, B, C and G also had median slopes, shear stresses, stream powers and velocities that were lower than the medians of sections without tracers. This results was generally the case for the other zones as well.

3.3.2.2 Flow conditions at time of deposition

The spring 2012 flows transported the active tracers 10 m to 2140 m downstream of their deployment sites. The last record of motion for these tracers constrained the timing of deposition and corresponded to discharges ranging from 3.0 m^3s^{-1} to 6.9 m^3s^{-1}. The modeled shear stresses for these deposition discharges and locations ranged from 30 N m^{-2} to 270 N m^{-2}. Respective Shields numbers ($\tau^*_{dep,i}$) were between 0.016 and 0.12 (median of 0.060) (Figures 3.7a,b). The hiding function based on the stationary antenna records (Section 3.3.1) did not predict the deposition of the active tracers well (Figure 3.7c; correlation not significant, *p*-value>0.05). The D_{50} values used in comparing active tracers with the hiding function were approximated by the grain size distribution of the nearest point count (Figure 3.1f). The active tracers analyzed were those not deposited in the excavated pool area (discussed in Section 3.2.2). Tracers were only used in this analysis that had full records of motion throughout the season, to be certain that the last motion recorded corresponded to its final location.

3.3.3 RE-ENTRAINMENT

The records from the active tracers also enabled comparisons of flow conditions at re-entrainment to those at deposition. While the locations of the tracers were not known throughout the season, the timing of deposition and re-entrainment were known from the indications of motion and rest from the accelerometers. Hence, discharges rather than location-dependent shear stresses were employed for this analysis. The discharge when each tracer came to rest during one flood event (Q_{dep}) was compared to the discharge when the tracer was next re-entrained by a subsequent event (Q_{re}). In this manner, a series of re-entrainment to deposition discharges ratios (Q_{re}/Q_{dep}) were calculated for each tracer over the spring 2012 season. A Q_{re}/Q_{dep} ratio exceeded one when a tracer was re-entrained from a resting position at a discharge that was higher than the discharge when the tracer previously deposited into the position.

Over the season, the re-entrainment discharges varied from 0.5 to 2.5 times the respective deposition discharges (Figures 3.8a,b). The median of the Q_{re}/Q_{dep} ratios for the 30 records corresponding to the first three, mid-March events was 1.13 (mean ± standard error of 1.22±0.06). The median of the Q_{re}/Q_{dep} ratios for Events 4 to 11 (70 records) was 1.04 (mean ± standard error of 1.14±0.05). The distributions of the Q_{re}/Q_{dep} ratios during Events 1-3 were not statistically different from Events 4-11 (Wilcoxon Rank-Sum p-value>0.05). However, the distribution of the deposition discharges during Events 1-3 were significantly lower than during Events 4-11 (Wilcoxon Rank-Sum p-value<0.05). The deposition discharges were likely lower during Events 1-3 due to the initial movements of the tracers into more natural positions from the deployment positions [Ch. 2]. For Events 4 through 11, deposition discharges varied from 1.2 m^3s^{-1} to 3.9 m^3s^{-1} and re-entrainment discharges varied from 1.6 m^3s^{-1} to 7.9 m^3s^{-1} (Figure 3.8c).

3.4 Discussion

3.4.1 HIDING FUNCTIONS

The hiding functions based on the Shields numbers of the antenna records had b-exponents near -1 (Equation 3.6; Figures 3.5b,d; Table 3.1), indicating near equal entrainment mobility conditions. This finding suggests that the thresholds capable of entraining the range of tracer sizes (0.75 to 2.74 times the D_{50} of the reach) were similar, i.e. not significantly grain size dependent over this clast size range. It is important to note that the near equal entrainment mobility results are restricted to bedload clasts of similar sizes to the tracers recorded. With the advent of RFID tags now as small as 8 mm (e.g., a $D_i/D_{50} \approx$=0.1 for the antenna reach) instead of the 23 mm smallest tags used in this study, future studies can employ stationary antennas and passive tracers to investigate hiding functions over a wider range of grain sizes.

Due to the unique method of the tracers and antenna system employed to compute the hiding functions, the hiding functions are calculated again with the method of flow competence to compare results to previous efforts. The flow competence technique is typically performed by

collecting grab samples over a range of shear stresses, and for each shear stress measured, comparing the maximum grain size in the grab samples with their respective Shields number [e.g., *Ashworth and Ferguson*, 1989; *Marion and Weirich*, 2003; *Lenzi et al.*, 2006a]. Like the records of the tracers crossing the antennas, the grab samples also represent clasts that have already been entrained and, thus, approximates critical conditions. *Yager et al.* [2012a] also applied the flow competence concept to constrain hiding functions by evaluating the D_{84} of passive tracers that became mobile during an event ($D_{84\text{-}m}$, determined by surveys before and after floods), and comparing the $D_{84\text{-}m}$ /D_{50} values to the respective Shields numbers using each event's peak shear stress. Due to the lack of grab samples available from Reynolds Creek, this latter method used by *Yager et al.* [2012a] is applied to the tracer-antenna dataset to compare flow competence results. Only the artificial tracers are examined with this method due to the limited number of the natural tracers. The events compared occurred after the initial mid-March events and each included records of at least 10 tracers (i.e., events 4, 5, 6, 7, 8, 9 and 11; Figure 3.5a).

The hiding function based on the tracer flow competence method showed $\tau^*_{c,50}$ and *b*-exponent values that were within the uncertainty range of those found with by fitting minimum Shields numbers for each tracer grain size (Figure 3.9). The flow competence values of $\tau^*_{c,50}$ and *b* were 0.075±0.022 and -0.88±1.02, respectively (where uncertainty represents 95% confidence bounds; R^2=0.50; not significant correlation *p*-value=0.11). The $\tau^*_{c,50}$- $D_{84\text{-}m}$ /D_{50} point for event 11 plotted well above the others and contributed to the large uncertainties. This discrepancy of the event 11 point was likely due to the $D_{84\text{-}m}$ not being representative of the largest bedload clasts that moved during the highest flows, the peak of which was approximately twice those of the previous events. Excluding event 11, the flow competence hiding function values were similar but have lower uncertainty ($\tau^*_{c,50}$=0.073±0.005 and *b*=-0.90±0.19; R^2=0.98; significant correlation *p*-value<0.05). This new analysis demonstrates that the tracer-based flow competence method employed by *Yager et al.* [2012a] can reasonably approximate the threshold of motion conditions. However, as evident by the outlier from event 11, careful consideration

into choice of tracer sizes should be exercised to avoid under estimating the largest mobile grain sizes, which is a common concern with flow competence-based methods [e.g., *Ashworth and Ferguson*, 1989; *Ferguson et al.*, 1989; *Wilcock*, 1992].

The near equal entrainment threshold results, supported by both the antenna and flow competence techniques that calculated *b* and *c* exponents (Equations 3.6 and 3.7), were also generally consistent with the previous studies that collected bedload samples in similar sloped channels (resulting in *b*-exponent values closer to -1 than 0, i.e., $-1<b<-0.75$; Table 3.5) [e.g., *Andrews*, 1983; *Ferguson et al.*, 1989; *Parker*, 2008]. Most of these previous studies used the flow competence method based on grab samples. Some of these *b*-exponents in previous studies may be even closer to -1 than reported because flow competence methods potentially underestimate maximum grain sizes due to small sampler sizes and short sample durations. For example, *Ferguson* [2005] found that both *b* and *c* exponents based on flow competence methods falsely indicated that bed behavior was more size selective than actual conditions. Values of *b*- and *c*-exponents estimated for reaches having steeper gradients ($S\geq0.08$ m/m) with immobile boulders showed more size selective behavior than that observed in the antenna reach (b-exponents between -0.78 and -0.62; Table 3.5) [e.g., *Marion and Weirich*, 2003; *Mao et al.*, 2008]. This difference in the steeper channels is due in part to the wider range of grain sizes and tendency for the coarser beds to rarely become fully mobile [e.g., *Yager et al.*, 2012a]. While there were some sections in Reynolds Creek with large, immobile boulders, most reaches in the study area had plane beds consisting predominantly of gravels and cobbles. Thus, it is expected that near equal entrainment mobility approximated many of the areas across the study area for the coarse bedload grains (i.e., similar to the tracers).

3.4.2 CHANNEL MORPHOLOGY

The results from combining tracer positions with flow modeling over multiple kilometers (Section 3.3.2.1; Tables 3.3 and 3.4) represent a new approach in quantifying the effects of channel morphology on transport. Previously, field studies have concluded that channel

morphology plays a role in determining particle displacements [e.g., *Kondolf and Matthews*, 1986; *Hassan et al.*, 1992; *Pyrce and Ashmore*, 2003], but technological limitations have restricted these efforts from being able to systematically address this hypothesis. Differences in the results amongst the seven delineated channel zones suggest that the degree to which bedload grains are influenced by local channel morphology can vary spatially. The demonstrated influence of width on the majority of zones further indicates that transport may not be solely stochastic process in natural channels [e.g., *Einstein*, 1950].

Field observations collected during the stream surveys support the interpretation that channel width can affect bedload transport in steep channels. I observed that the plane-bed sections confined by bedrock sidewalls or thick willow stands typically had alluvial beds with few sediment accumulation features such as point bars (e.g., Figures 1b,c). It is expected that the confined channel conditions in steep streams can cause increases in water velocities that in turn decrease the prevalence for depositional areas compared to the flatter morphologies of lowland rivers, which often have extensive depositional features such as large scale-point bars [*Montgomery and Buffington*, 1997]. The median velocities in zones A, B, C and G were calculated as slightly lower at the sections with tracers than without (6% to 15% depending on zone; Table 3.4). The slightly less confined, wider sections of the study area still had plane-bed morphology; however, these sections also had notably more sediment patches. The deposition patches in these wider sections consisted of gravel and cobble deposits on the order of 1 to 2 m^2 and small point bars ranging from approximately 5 to 15 m in length (e.g., Figures 3.1d,e).

The lack of statistical significance being found for the majority of parameters (except width) in the majority of zones does not preclude the potential that these parameters play a role in transport. The statistical results were influenced in part by the lower sample sizes available for the sections without tracers (Table 3.2). Although statistically not significant in the model-based analysis of flow parameters, prior study qualitatively suggested that clasts may show preferential deposition in lower-sloped reaches [*Laronne and Carson*, 1976].

The influence of slope was also investigated in this study using the active tracers and previous datasets because the hiding function from the antenna records failed to predict the deposition conditions of the active tracers at other reaches having differing slopes (Figure 3.7c). Values of $\tau^*_{c,50}$ must first be estimated for the active tracers for comparison to previous field interpretations. The $Q_{re} \approx Q_{dep}$ portion of the Q_{re}/Q_{dep} results from the accelerometer records (Section 3.3.3) are employed to approximate the threshold conditions such that $\tau^*_{c,i}=\tau^*_{dep,i}$. The *b*-exponent of -0.965 from the hiding function for the artificial tracers (Section 3.3.1) is then used for the conversion from $\tau^*_{c,i}$ to $\tau^*_{c,50}$. While *b*-exponents may vary spatially, the -0.965 value is utilized due to the lack of other field constraints from the field datasets over the study area and its broad consistency with previous studies (Table 3.5).

The calculated $\tau^*_{c,50}$ results from the active tracers overlap with the results of previous studies from similar sloped reaches (Figure 3.10) [compiled in *Buffington and Montgomery*, 1997; compiled in *Mueller et al.*, 2005; *Scheingross et al.*, 2013]. The $\tau^*_{c,50}$ from the active tracers increased with slope as

$$\tau^*_{c,50} = 0.51S^{0.46} \quad (p<0.05, R^2=0.67) \tag{3.8}$$

The constraints around the 0.51 coefficient and 0.46 exponent are large (95% confidence bounds are ±0.42 and ±0.26, respectively). However, the combination of the active tracer records with the previous field studies shows a fairly similar relation with improved uncertainty

$$\tau^*_{c,50} = 0.52S^{0.51} \quad (p<0.05, R^2=0.61) \tag{3.9}$$

where the 95% confidence bounds are 0.52±0.19 and 0.51±0.10 (Figure 3.10).

The demonstrated change in the thresholds with slope highlights the inadequacy of assuming a single $\tau^*_{c,50}$ value to characterize bedload transport across the study area [e.g., *Andrews*, 1980; *Torizzo and Pitlick*, 2004; *USDA-NRCS*, 2007]. The slope-threshold relations of Equations 3.8 and 3.9 provide further evidence that channel morphology influences transport as well as deposition since the entrainment and deposition thresholds were near symmetric in the Q_{dep}/Q_{re} rations (Figure 3.8b). Further, these relations suggest that the degree to which thresholds increase with slope is somewhat higher than the relation presented by *Lamb et al.*

[2008] ($\tau^*_{c,50} \propto 0.15S^{0.25}$) (also plotted in Figure 3.10). This relation presented by *Lamb et al.* [2008] had an R^2=0.4, and was based on compiling field and flume data from slopes of 0.0002 m/m to 0.37 m/m (including the previous studies used in Equation 3.9). This distinction of slope sensitivity is significant for fluvial studies and projects that model bed stability and bedload transport in channels in steep reaches based on empirical relations of $\tau^*_{c,50}$ [e.g., *Torizzo and Pitlick*, 2004; *Niezgoda et al.*, 2014]. The consideration of threshold sensitivity to slope could also improve landscape models that commonly apply a single threshold values [e.g., *Howard et al.*, 1994; *Whipple and Tucker*, 1999].

3.4.3 DISTRIBUTION OF TRANSPORT THRESHOLDS

The findings of re-entrainment discharges approximating deposition discharges ($Q_{re} \approx Q_{dep}$; Section 3.4.3; Figure 3.8) are in line with the use of a single Shields number as a transport threshold (e.g., $\tau^*_{c,i}$) values based on field-derived hiding functions. However, the range of Q_{re}/Q_{dep} ratios from 0.5 to 2.5 indicates that $\tau^*_{c,i}$ thresholds are a distribution rather than a single value. Given that the median of the Q_{re}/Q_{dep} ratio was near 1, predicting that re-entrainment thresholds equaled or exceeded those of deposition would have failed to predict almost half the observations [e.g., *Hjulström*, 1935; *Turowski et al.*, 2011]. The Q_{re}/Q_{dep} results suggest that river management projects with objectives of estimating bedload budgets and bed stability would better plan for possible project outcomes by evaluating transport using a range of thresholds. The threshold distribution also suggests that larger uncertainties are likely associated with paleohydrologic studies that have constrained the magnitudes of peak flood events based on assuming a single critical Shields numbers for the largest found in grains deposits [e.g., *Baker*, 1974; *Sugai*, 1993; *Grossman*, 2001].

3.5 Conclusions

This study examined whether conceptual and numerical bedload models could be improved by characterizing bedload transport, deposition and re-entrainment behavior in terms

of stochastic hydrologic forcing and channel morphology. Bedload was monitored in a mountain stream using RFID and accelerometer embedded tracers and stationary RFID-antennas over a series of snowmelt floods. Hydrologic forcing and channel morphologies relating to transport, deposition and re-entrainment were compared in terms of relative grain size, bed slope, channel width, flow depth, shear stress, stream power and flow velocities. Tracers tended to deposit in wider channel sections, and transport thresholds were higher in steeper sloped reaches. In the reach with the RFID antennas, grain size was not shown to influence the threshold conditions for deposition and re-entrainment of the coarse bedload particles, i.e., tracers showed near equal entrainment mobility. A distribution of thresholds was observed, and almost half of the observations contrasted with the classic theory of *Hjulström* [1935] by demonstrating that deposition occurred at flow strengths lower than re-entrainment.

Tables

Table 3.1: Hiding functions from stationary antenna records

Hiding functions based on the minimum Shields numbers and unit discharges recorded for each grain size in the 0.018 m/m stationary antenna reach (Equations 3.6 and 3.7). The Shields number regressions were significant but the unit discharge regressions were not significant (95% confidence).

Shields numbers

tracer type	Event IDs	$\tau^*_{c,50}$ ± 95% confidence bounds	*b*-exponent ± 95% confidence bounds	Goodness of power fit: sum of squares due to error	Goodness of power fit: root mean square error	R^2
artificial	1 to 11	0.066±0.001	-0.932±0.070	0.0004	0.003	0.96
	4 to 11	0.072±0.002	-0.965±0.061	0.083	0.050	0.97
natural	4 to 10	0.064±0.007	-1.13±0.16	0.019	0.039	0.95

Unit discharges

tracer type	Event IDs	$q_{c,i}$ ± 95% confidence bounds	c-exponent ± 95% confidence bounds	Goodness of power fit: sum of squares due to error	Goodness of power fit: root mean square error	R^2
artificial	4 to 11	0.184±0.012	0.109±0.156	0.021	0.025	0.06
natural	4 to 10	0.250±0.074	-0.312±0.44	0.006	0.021	0.17

Table 3.2: Summary of channel zones evaluated for sections with and without tracer deposition

Zone	*L* (m)	*S* (m/m)	number of tracers deposited in section	tracer concentration over zone (tracer/m)	number of 10 m sections with tracers	without tracers
A	660	0.022	121	0.18	42	24
B	260	0.039	37	0.14	17	9
C	270	0.060	60	0.22	20	7
D	480	0.037	76	0.16	39	9
E	740	0.037	100	0.14	46	28
F	360	0.026	41	0.11	21	15
G	350	0.021	32	0.09	18	17

Notation) *L*: Length; *S*: average slope over zone

Table 3.3: Results of Wilcoxon Rank-Sum *p*-values between sections with and without tracer deposition

The results with Rank-Sum *p*-value<0.05 indicated a rejection of the null hypothesis at a 95% confidence level that the samples were from the same population, i.e. areas with and without tracers were statistically different. Zones with p<0.05 are indicated in bold and underlined.

Rank-Sum *p*-value for main parameters

		$Q_m = 2m^3s^{-1}$					$Q_m = 4\ m^3s^{-1}$				
Zone	*S*	τ	*w*	Ω	*h*	*U*	τ	*w*	Ω	*h*	*U*
A	0.65	0.09	***0.01***	0.08	***0.04***	***0.04***	***0.03***	***0.01***	***0.03***	***0.02***	***0.01***
B	0.11	0.11	***0.01***	0.11	0.94	0.11	***0.00***	***0.01***	***0.01***	0.19	***0.00***
C	0.10	0.80	***0.04***	0.98	0.07	0.98	0.18	***0.03***	0.11	0.11	0.14
D	0.60	0.67	0.94	0.58	0.62	0.72	0.71	1.00	0.58	0.79	0.71
E	***0.02***	***0.01***	0.61	***0.01***	0.14	***0.02***	0.08	0.92	0.07	0.22	0.09
F	0.48	0.95	0.70	0.95	0.53	0.81	0.87	0.36	0.90	0.30	0.83
G	0.19	0.16	***0.03***	0.14	0.82	0.16	0.48	***0.02***	0.35	0.39	0.36

Rank-Sum *p*-value for change in parameters with respect to the 10 m section upstream, where d*x*=10 m

		$Q_m = 2\ m^3s^{-1}$					$Q_m = 4\ m^3s^{-1}$				
Zone	d*S*/d*x*	dτ/d*x*	d*w*/d*x*	dΩ/d*x*	*dh*/d*x*	*dU*/d*x*	dτ/d*x*	d*w*/d*x*	dΩ/d*x*	*dh*/d*x*	*dU*/d*x*
A	0.95	0.65	0.85	0.66	0.88	0.79	0.45	0.34	0.39	0.97	0.49
B	0.16	0.09	***0.02***	0.07	0.67	0.11	0.08	***0.01***	***0.04***	0.52	0.06
C	0.07	0.52	***0.04***	0.49	0.20	0.68	0.06	***0.03***	***0.03***	0.49	0.19
D	0.21	0.71	0.65	0.49	0.94	0.98	1.00	0.34	1.00	0.87	0.84
E	0.83	0.62	0.15	0.51	0.18	0.73	0.58	0.28	0.44	0.26	0.73
F	0.35	0.92	0.85	0.85	0.70	0.97	0.77	0.44	0.72	0.64	0.37
G	0.17	0.61	0.07	0.70	0.88	0.46	0.78	0.07	0.80	0.47	0.56

Rank-Sum *p*-value for change in parameters within a 10 m section with respect to discharge, where dQ_m=2 m^{3}s^{-1} (4m^{3}s^{-1} – 2 m^{3}s^{-1})

Zone	dτ/dQ_m	d*w*/ dQ_m	dΩ/ dQ_m	*dh*/ dQ_m	*dU*/ dQ_m
A	***0.02***	***0.02***	***0.01***	0.07	***0.02***
B	***0.00***	***0.02***	***0.00***	0.06	***0.00***
C	0.16	0.42	0.08	0.74	0.23
D	0.14	0.96	0.14	0.67	0.22
E	0.99	0.45	0.52	0.51	0.46
F	0.59	0.10	0.87	0.24	0.56
G	0.80	***0.03***	0.52	0.06	0.61

Notation) Q_m: modeled discharge; *S*: averaged 10 m bed slope; τ: averaged shear stress over 10 m sections; *w*: averaged wetted widths over 10 m sections; Ω: averaged stream power over 10 m sections; *h*: averaged flow depths over 10 m sections; U: averaged flow velocity over 10 m sections.

Table 3.4: Comparison of median results between sections with and without tracer deposition

The percent differences represent the median values from sections without tracers (*ND*) compared to those with tracers (*D*) within each zone (i.e., $(D - ND)/ND$). A negative result indicates the median of that parameter was lower in the sections with tracers than those without tracers (highlighted in blue). A positive result are highlighted in red. The results that correspond to statistically significant differences at a 95% confidence level are also underlined (i.e., Rank-Sum *p*-value<0.05 per Table 3.3). Results corresponding to p>0.05 are indicated as "NS" for not significant at a 95% confidence level (i.e., Rank-Sum *p*-value>0.05 per Table 3.3).

Percent differences for the main parameters

	$Q_m = 2m^3s^{-1}$						$Q_m = 4\ m^3s^{-1}$				
Zone	*S*	τ	*w*	Ω	*h*	*U*	τ	*w*	Ω	*h*	*U*
A	NS (-24%)	NS (-27%)	***17%***	NS (-43%)	***-14%***	***-15%***	***-25%***	***18%***	***-36%***	***-14%***	***-13%***
B	NS (-27%)	NS (-22%)	***5%***	NS (-28%)	NS (1%)	NS (-13%)	***-25%***	***8%***	***-27%***	NS (12%)	***-15%***
C	NS (-32%)	NS (-16%)	***16%***	NS (-16%)	NS (-20%)	NS (-9%)	NS (-25%)	***12%***	NS (-35%)	NS (-14%)	NS (-12%)
D	NS (-4%)	NS (4%)	NS (3%)	NS (6%)	NS (-12%)	NS (2%)	NS (-7%)	NS (0%)	NS (-10%)	NS (-7%)	NS (-2%)
E	***-26%***	***-27%***	NS (2%)	***-38%***	NS (4%)	***-12%***	NS (-17%)	NS (0%)	NS (-28%)	NS (7%)	NS (-8%)
F	NS (-22%)	NS (10%)	NS (-1%)	NS (5%)	NS (-5%)	NS (2%)	NS (3%)	NS (12%)	NS (7%)	NS (-10%)	NS (0%)
G	NS (-25%)	NS (-17%)	***23%***	NS (-28%)	NS (-6%)	NS (-7%)	NS (2%)	***21%***	NS (-5%)	NS (-4%)	NS (-6%)

Percent differences for the change in parameters with respect to the 10 m section upstream, where d*x*=10 m

	$Q_m = 2\ m^3s^{-1}$						$Q_m = 4\ m^3s^{-1}$				
Zone	d*S*/d*x*	dτ/d*x*	d*w*/d*x*	dΩ/d*x*	*dh*/d*x*	*dU*/d*x*	dτ/d*x*	d*w*/d*x*	dΩ/d*x*	*dh*/d*x*	*dU*/d*x*
A	NS (-173%)	NS (-1249%)	NS (225%)	NS (-192%)	NS (100%)	NS (600%)	NS (-130%)	NS (-95%)	NS (-130%)	NS (81%)	NS (-51%)
B	NS (-187%)	NS (-185%)	***-249%***	NS (-226%)	NS (-267%)	NS (-174%)	NS (-76%)	***-229%***	***-93%***	NS (-450%)	NS (-82%)
C	NS (-97%)	NS (-98%)	***-148%***	NS (-121%)	NA	NS (-40%)	NS (-111%)	***-112%***	***-105%***	NS (-50%)	NS (-112%)

Notation) Q_m: modeled discharge; *S*: averaged 10 m bed slope; τ: averaged shear stress over 10 m sections; *w*: averaged wetted widths over 10 m sections; Ω: averaged stream power over 10 m sections; *h*: averaged flow depths over 10 m sections; and NA: not applicable due to d*h*/d*x* medians being equal to 0.

Table 3.4 (continued): Comparison of median results between sections with and without tracer deposition

Percent differences for the change in parameters with respect to the 10 m section upstream, where d*x*=10 m

		$Q_m = 2\ m^3s^{-1}$					$Q_m = 4\ m^3s^{-1}$				
Zone	d*S*/d*x*	dτ/d*x*	d*w*/d*x*	dΩ/d*x*	*dh*/d*x*	*dU*/d*x*	dτ/d*x*	d*w*/d*x*	dΩ/d*x*	*dh*/d*x*	*dU*/d*x*
D	NS (56%)	NS (-124%)	NS (-70%)	NS (-119%)	NA	NS (-663%)	NS (-321%)	NS (-76%)	NS (-274%)	NS (-200%)	NA
E	NS (-91%)	NS (-57%)	NS (-155%)	NS (-61%)	NS (-383%)	NS (-51%)	NS (-65%)	NS (-142%)	NS (-62%)	NS (-142%)	NS (-57%)
F	NA	NS (88%)	NS (-66%)	NS (-1132%)	NS (25%)	NA	NS (431%)	NS (-154%)	NS (-3010%)	NS (-143%)	NS (563%)
G	NS (-436%)	NS (-305%)	NS (-813%)	NS (-260%)	NS (0%)	NS (-395%)	NS (14%)	NS (-482%)	NS (17%)	-110%	NA

Percent differences for the change in parameters within a 10 m section with respect to discharge, where dQ_m=2 m^{3}s^{-1} (4m^{3}s^{-1} – 2 m^{3}s^{-1})

Zone	dτ/dQ_m	d*w*/ dQ_m	dΩ/ dQ_m	*dh*/ dQ_m	*dU*/ dQ_m
A	***-25%***	***27%***	***-37%***	NS (-10%)	***-17%***
B	***-36%***	***15%***	***-48%***	NS (14%)	***-23%***
C	NS (-33%)	NS (7%)	NS (-50%)	NS (-9%)	NS (-10%)
D	NS (-24%)	NS (-3%)	NS (-30%)	NS (-2%)	NS (-10%)
E	NS (-7%)	NS (-9%)	NS (-20%)	NS (8%)	NS (2%)
F	NS (-19%)	NS (19%)	NS (-28%)	NS (-5%)	NS (-12%)
G	NS (15%)	***25%***	NS (22%)	NS (-8%)	NS (6%)

Notation) Q_m: modeled discharge; *S*: averaged 10 m bed slope; τ: averaged shear stress over 10 m sections; *w*: averaged wetted widths over 10 m sections; Ω: averaged stream power over 10 m sections; *h*: averaged flow depths over 10 m sections; and NA: not applicable due to d*h*/d*x* medians being equal to 0.

Table 3.5: Summary of hiding function exponents from previous studies for comparison to those from the 0.018 m/m antenna reach

Study	Channel	Stream type	S (m/m)	D_{50} (mm)	Threshold method	sampler size (mm)	duration of samples	D_i/D_{50} range	b-exponent	c-exponent
[*Andrews*, 1983]	Snake River	Sinuous river	0.001	54	flow competence (D_{max} with Helley Smith)	76	NR	0.3-6	-0.872**	NA
	Clearwater River	Sinuous river	0.0001	74	flow competence (D_{max} with Helley Smith)	76	NR			
	East Fork River	sinuous river	0.007	1.3*	flow competence- D_{max} in slot-style bedload trap	NA	NA			
[*Parker*, 1990a]	Oak Creek	plane-bed reach	0.01	54	reference values (low transport rates using bedload trap)	NA	NR	NR	-0.905	NA
[*Whitaker and Potts*, 2007]	Dupuyer Creek	riffle reach	0.01	56	flow competence (D_{max} with larger bedload sampler)	450	1 min at peak flow to 60 min at low flow	1.57-3	-0.59	0.84
[*Andrews and Erman*, 1986]	Sagehen Creek	plane-bed reach	0.014	60	flow competence (D_{max} with Helley Smith)	150	4 min	1-3	-0.87**	NA
[*Parker*, 2008]	Compilation of datasets	varied	0.01-0.015		varied	NR	NR	NR	-0.79 (95% conf. -0.63 to -0.95)	NA
[*Ferguson et al.*, 1989]	White River	braided river	0.017	73	flow competence (D_{max} with Helley Smith)	76	15 s to 2 min	0.05-1	-0.88	NA
[*Ashworth and Ferguson*, 1989]	Dubhaig	riffle-pool	0.004-0.021	23-98	flow competence (D_{max} with Helley Smith)	76	30 s to 10 min at low flow	0.1-1.5	-0.74 (95% conf. -0.5 to -1)	NA
	Feshie	riffle-pool	0.009	52-63						
	Lyngsdalselva	braided proglacial stream	0.020-0.028	69						
[*Marion and Weirich*, 2003]	Toots Creek	step-pool	0.08	80	flow competence (D_{95} with Helley Smith)	73	60 s	0.01-0.6	-0.73	NA
[*Yager et al.*, 2012a]	Erlenbach	boulder- bedded torrent	0.098	141	flow competence (D_{84} of moved tracers)	NA	NA	0.2-0.7	-0.62	NA
[*Mao et al.*, 2008]	Rio Cordon	boulder- bedded step pool	0.17	119	flow competence (D_{max} with Helley Smith)	NA	NA	1-9	-0.639	0.619
	Tres Arroyos	step-pool	0.21	67	flow competence (D_{max} with Helley Smith)	152	60 s	0.01-0.2	-0.787	0.372

Notation) S: slope; D_{50}: median grain size; D_i/D_{50}: Relative grain size; *b*-exponent: Shields number hiding function (Equation 3.6); *c*-exponent: unit discharge hiding function (Equation 3.7); NA: Not applicable to study; NR: not reported; *: mostly sand bedded river with some gravels. **: used D_{50} subsurface

Figures

Figure 3.1: Study area, slope and grain size distribution study area

(a) Map of the study area and 1 m airborne LiDAR DEM [*Northwest Watershed Research Center*, 2009]. Locations of grain size point counts are indicated by triangles.
(b-e) Stream images across study area.
(f) Grain sizes determined by pebble counts [*Wolman*, 1954] [Ch. 2]. X-axis distance is the length downstream from the study's upstream boundary, which was a wooden bridge approximately 700 m upstream from the USDA-ARS Tollgate gauge (Station 116b) [Ch. 2].
(g) Slope averaged over 10 m moving windows over the study area. Slopes were based on the 1 m airborne LiDAR. The Tollgate gauge is located at where slope becomes 0.2 m/m.

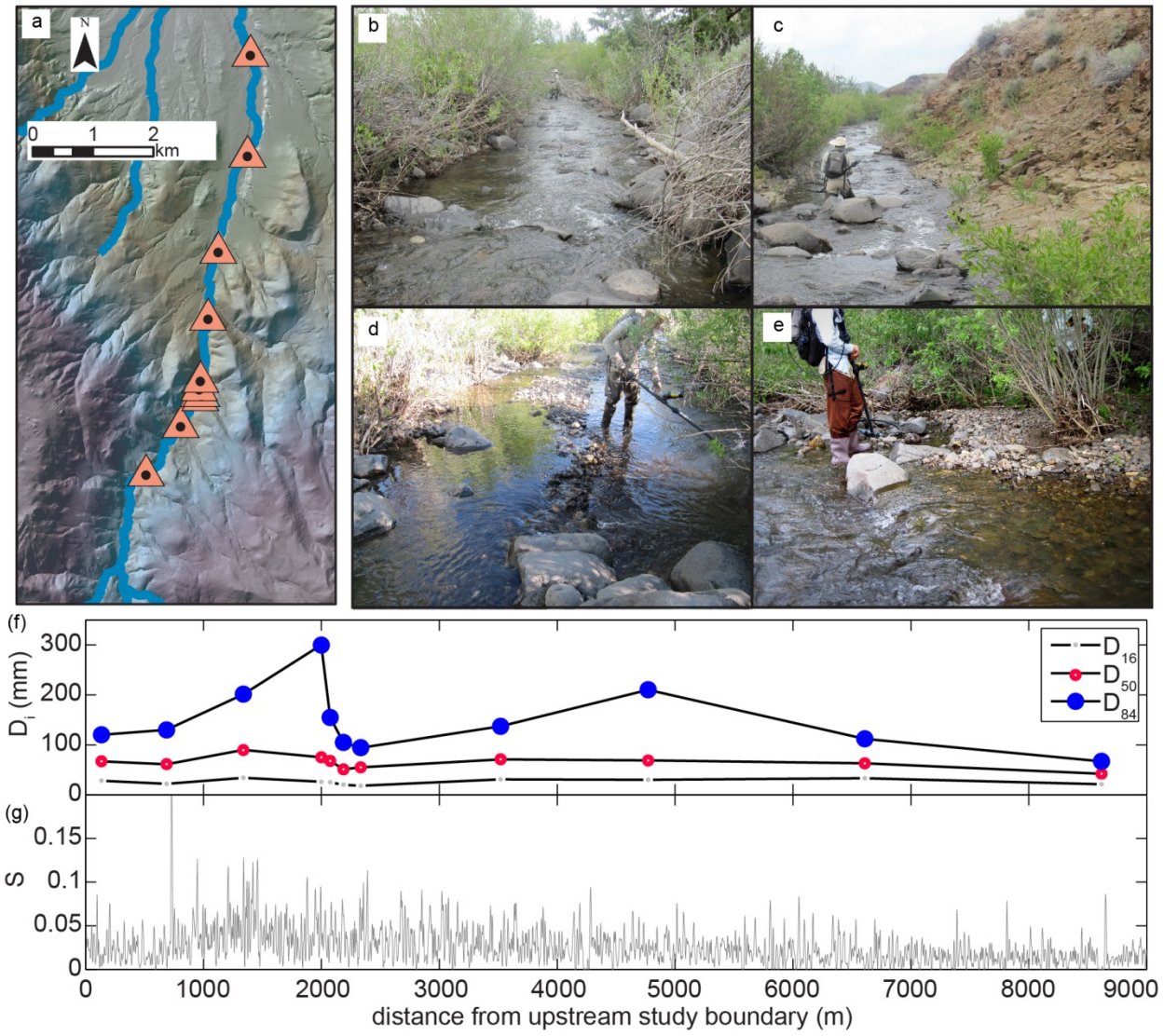

Figure 3.2: Hydrograph over monitored study period

Discharge (Q) over study period with vertical lines indicating deployment of passive tracers [*Northwest Watershed Research Center*, 2015]. Active tracers were also deployed in March 2012 with the passive tracers.

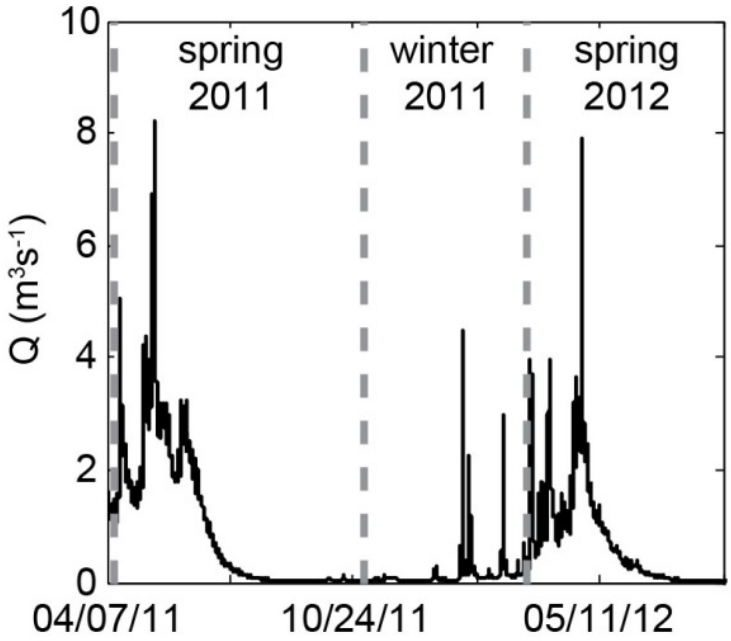

Figure 3.3: Example of motion and rest records from the active tracers

Spring 2012 discharge overlaid with the motion of one of the active tracers. Tracer motion is indicated by vertical line; no line indicates that the tracer was at rest. Triangle point corresponds to when the tracer was identified as passing stationary antennas.

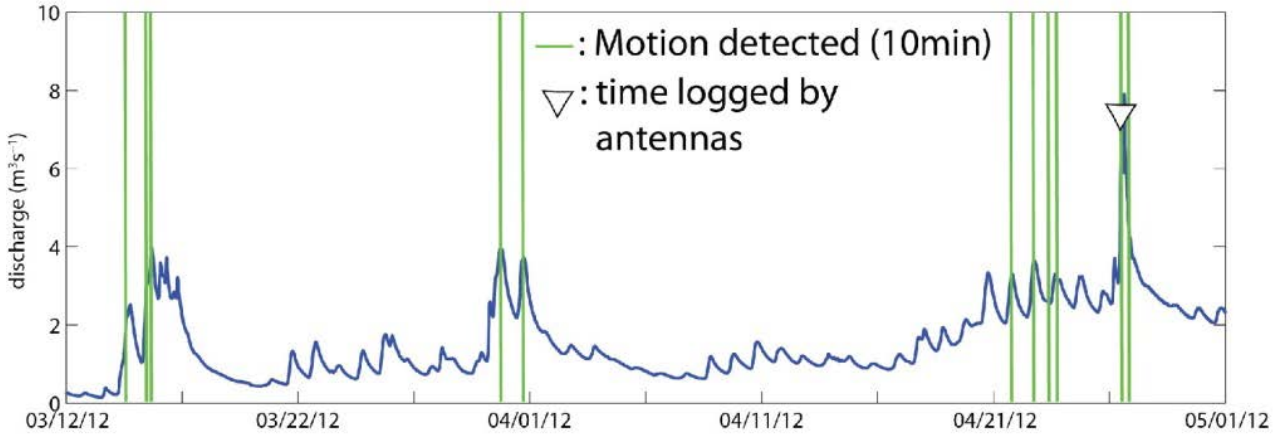

Figure 3.4: In-stream stationary RFID antennas

One of the 7 m by 0.5 m in-stream stationary RFID antennas.

Figure 3.5: Shields numbers and unit discharges corresponding to stationary antenna records

(a) Spring 2012 discharge (Q) from the Tollgate gauge [*Northwest Watershed Research Center*, 2015] with filled points indicating instances when at least one RFID-tracer was recorded in the stationary antenna reach. Event IDs are identified above peak discharges.
(b) For artificial tracers: Reach averaged Shields numbers (τ_i^*) (y-axis) versus the relative grain size of the tracer (D_i) to the reach's D_{50} (60 mm) (x-axis). The hiding function (solid line) is over the minimum Shields numbers recorded during events 4 through 11.
(c) For artificial tracers: Reach averaged unit discharges (q_i) versus the relative grain size. The hiding function (solid line) is over the minimum records from events 4 through 11.
(d) For natural tracers: Reach averaged Shields numbers versus the relative grain size. The hiding function (solid line) is over the minimum records from events 4 through 11.
(e) For natural tracers: Reach averaged unit discharges versus the relative grain size. The hiding function (solid line) is over the minimum records from events 4 through 11.

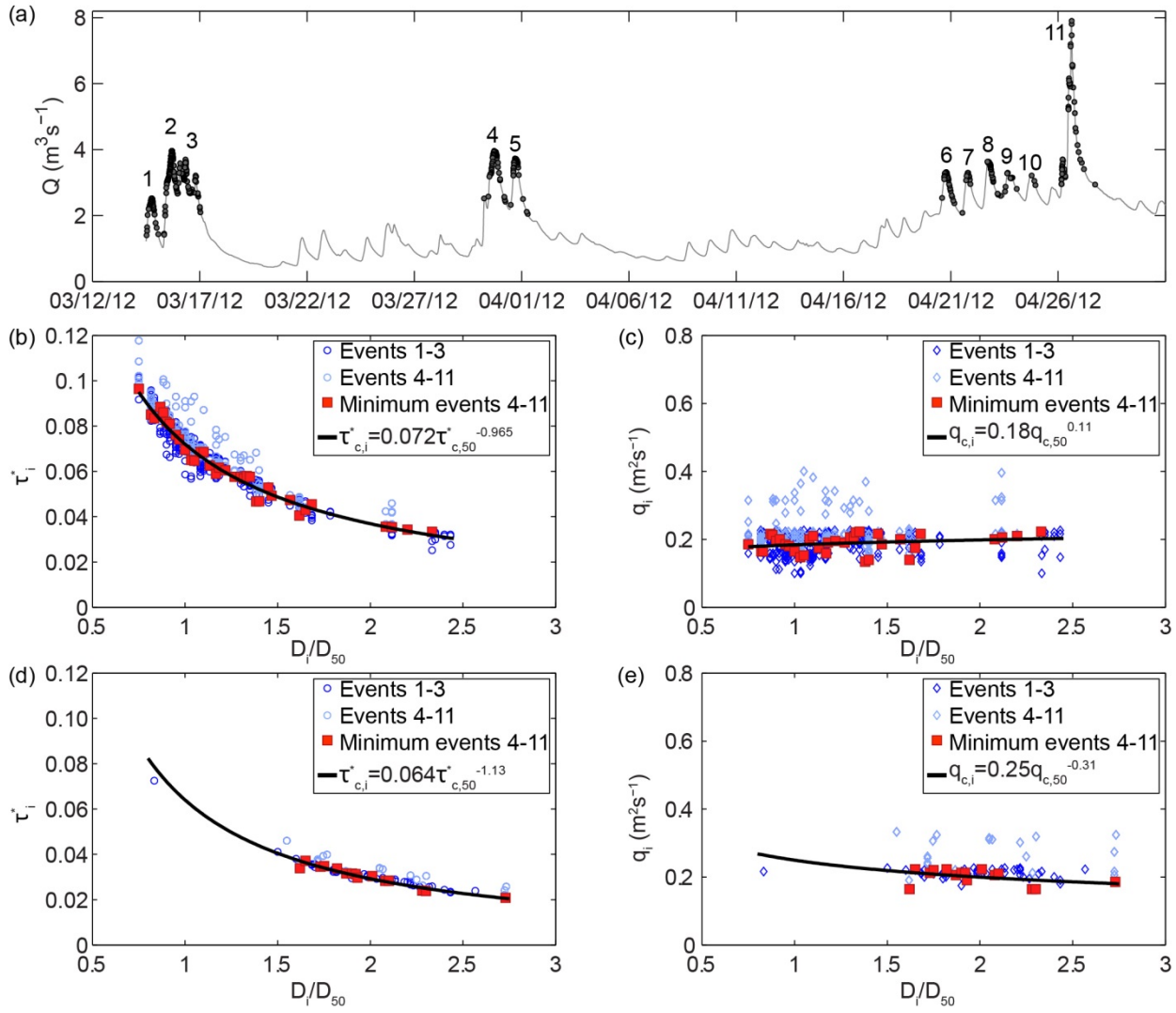

Figure 3.6: Comparison of channel widths in areas with and without tracer deposition

(a) Stream profile indicating the seven zones used for comparisons between the section with and without tracer deposition. The distance shown on the x-axis refers to the upstream study boundary that was approximately 700 m upstream the USDA-ARS Tollgate gauging station.
(b) Comparison of median widths between sections with and without tracer deposition over the seven zones. Zones A, B, C and G show preferential deposition in wider sections (Wilcoxon Rank-Sum p-value<0.05). The dashed line indicates the unity condition. Plotting above the 1:1 indicates that the areas with tracer deposition had larger widths than those without tracer deposition.
(c) Mean widths ± their respective standard errors for the sections with and without tracer deposition. Line colors correspond to the legend in Figure 6a. The dashed line indicates the unity condition. Plotting above the 1:1 indicates that the areas with tracer deposition had larger widths than those without tracer deposition.

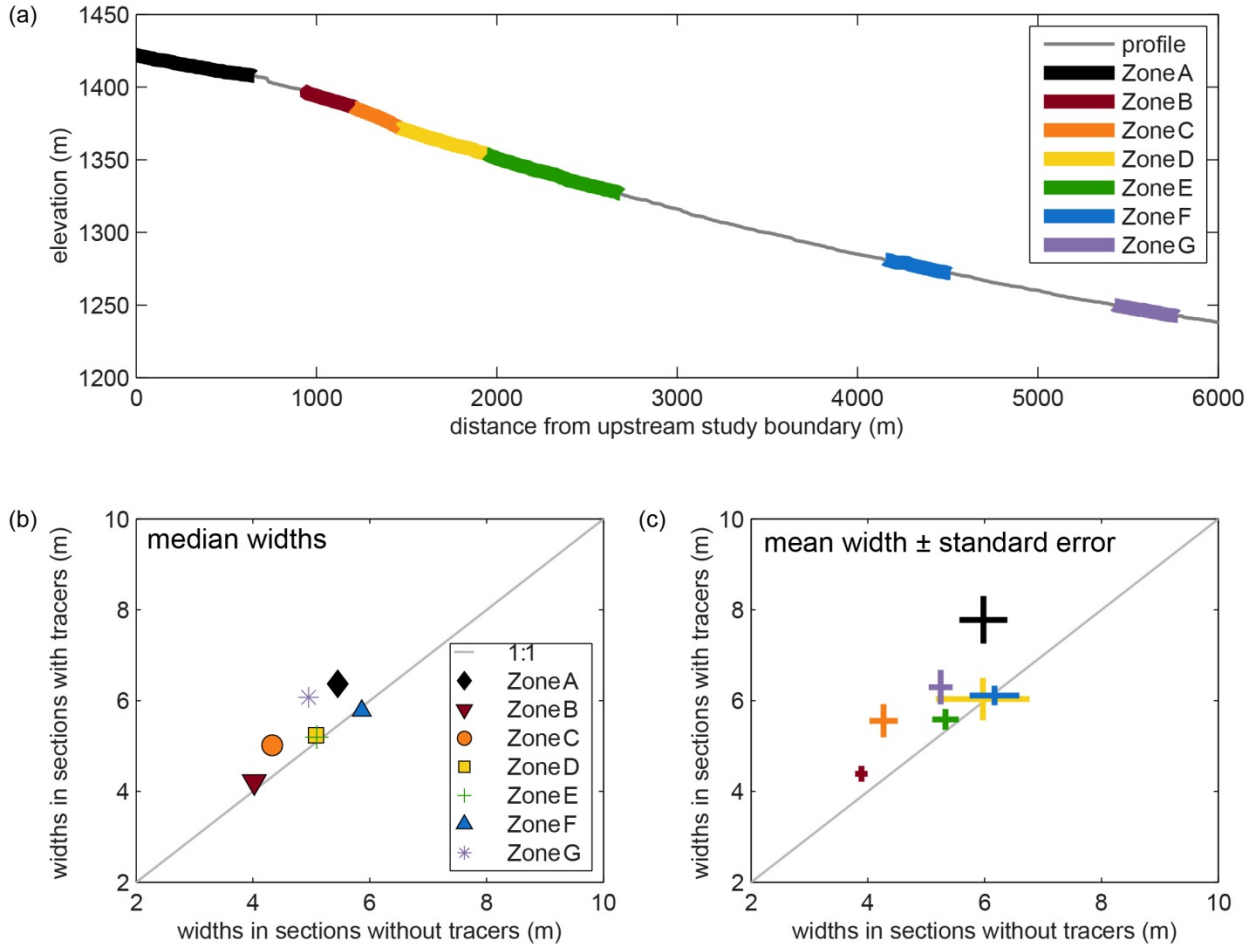

Figure 3.7: Deposition conditions of the active tracers

(a) Box plot of the shear stresses when and where the active tracers last deposited in spring 2012 ($\tau_{dep,i}$). The red horizontal line represents median (101 N m^{-2}), the box represents the 25th and 75th percentile (44 N m^{-2} and 153 N m^{-2}, respectively) and the whiskers represent the minimum and maximum values (33 N m^{-2} and 211 N m^{-2}, respectively).
(b) Box plot of the Shields numbers when and where the active tracers deposited last in spring 2012 ($\tau^*_{dep,i}$). The red horizontal line represents median (0.060 N m^{-2}), the box represents the 25th and 75th percentile (0.027 N m^{-2} and 0.095 N m^{-2}, respectively) and the whiskers represent the minimum and maximum values (0.020 N m^{-2} and 0.121 N m^{-2}, respectively).
(c) Shields stresses associated with the deposition of the active tracers versus relative grain size (D_i/D_{50}). The hiding function shown (solid line) is based on the stationary-antenna records of the artificial tracers (Figure 3.5b).

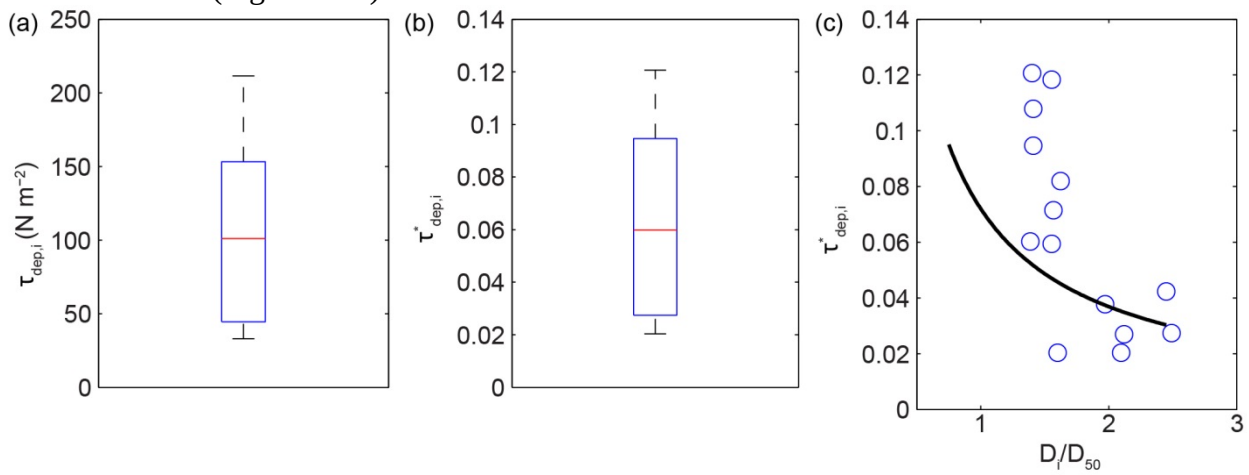

Figure 3.8: Comparisons of re-entrainment to deposition conditions from the records of the active tracers

(a) The Q_{re}/Q_{dep} ratios when clasts were re-entrained (primary y-axis) overlaid with spring 2012 discharge (Q) from the Tollgate gauge [*Northwest Watershed Research Center*, 2015] (secondary y-axis). Q_{dep} represents the discharge when each tracer deposited into a resting position and Q_{re} represents the discharge that re-entrained the tracer in a subsequent event. The open symbols correspond to the first three mid-March event that were not considered in further Q_{re}/Q_{dep} analyses to minimize potential influence of initial instabilities due to deployment. The dashed grey lines are at Q_{re}/Q_{dep} of 0.9 and 1.1. The Q_{re}/Q_{dep} ratios during Events 4 through 11 were as follows: 17% were $Q_{re}/Q_{dep} \leq 0.9$; 51% percent were $0.9 < Q_{re}/Q_{dep} \leq 1.1$; and 31% percent were $Q_{re}/Q_{dep} > 1.1$.
(b) Probability density function (*PDF*) of Q_{re}/Q_{dep} values associated with when clasts were re-entrained during events 4 to 11. The vertical line indicates the median (1.04).
(c) Comparison of each re-entrainment discharge with the respective previous deposition discharge. Points above the dashed 1:1 line correspond to when clasts were re-entrained at discharges larger than previous disentrainment conditions and points below the 1:1 line correspond to when clasts were re-entrained at discharges smaller than previous disentrainment conditions.

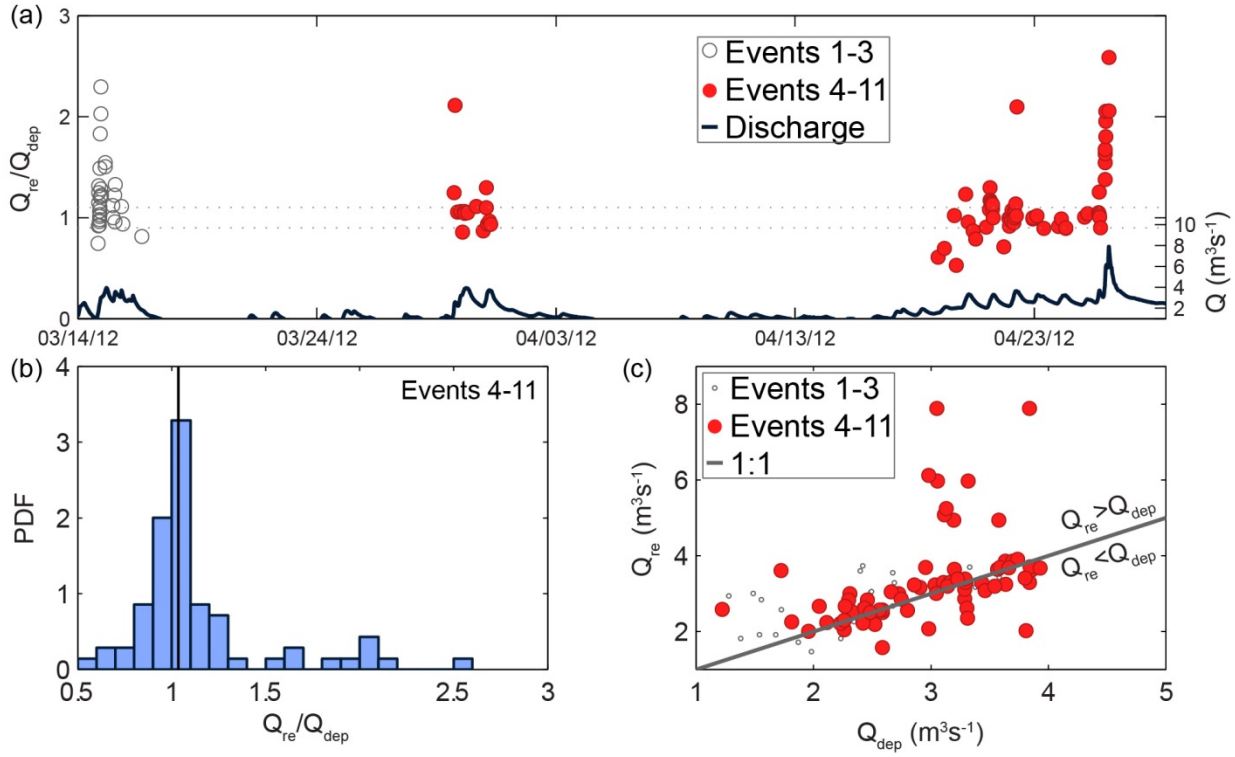

Figure 3.9: Hiding function using stationary antenna records and alternative flow competence method

The hiding function based on the minimum Shields numbers (τ_i^*) for each grain size based on the RFID antenna system during events 4 through 9 (blue line; as in Figure 3.5) is plotted with the hiding functions using the alternative flow competence method for each event. The flow competence points corresponding to events 4 and 5 closely overlap in the figure.

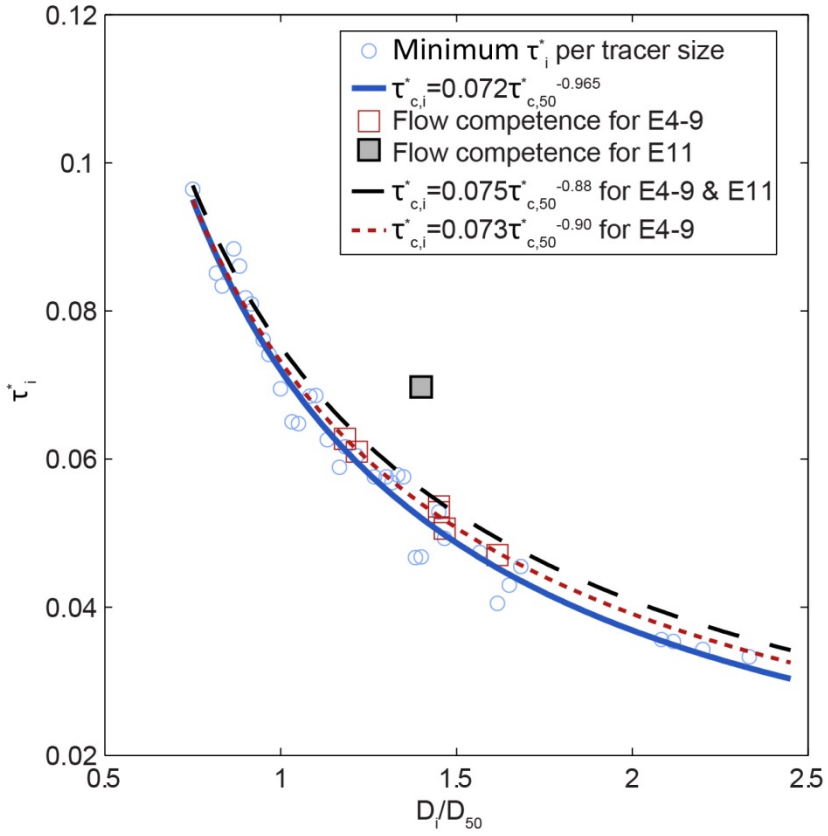

Figure 3.10: Threshold-slope evaluations using the active tracers

Critical Shields numbers ($\tau^*_{c,50}$) versus bed slope (S) from active tracers, stationary antenna and previous studies.

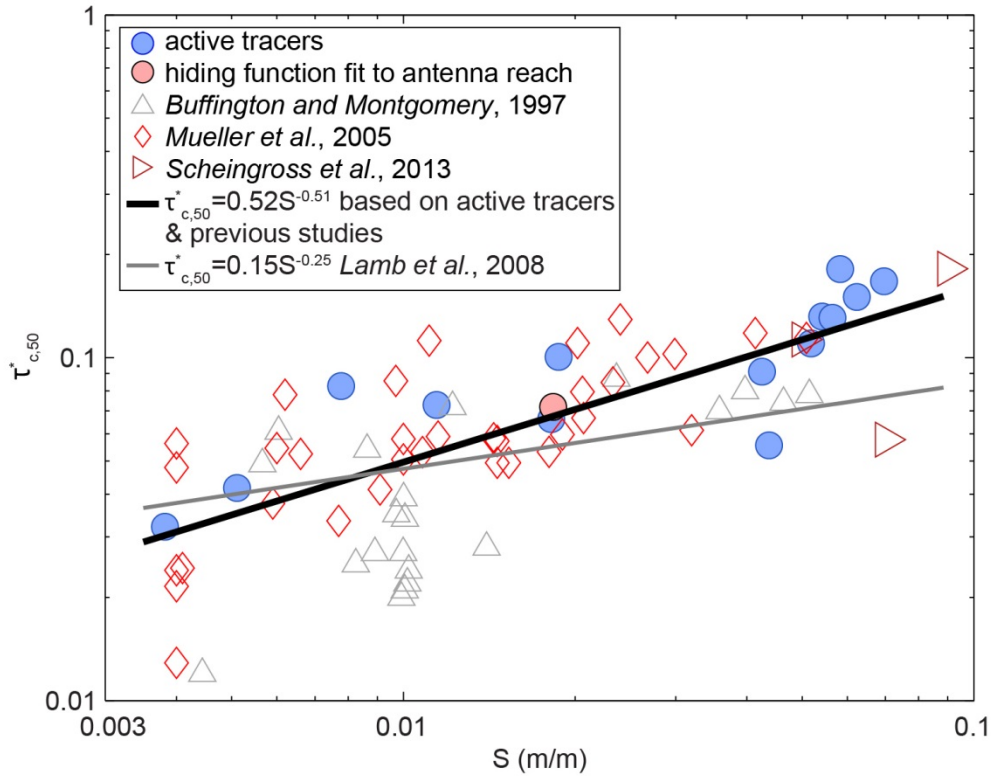

CHAPTER 4: MAGNITUDE-FREQUENCY ANALSYSIS OF BEDLOAD TRANSPORT IN A STEEP, COARSE CHANNEL

4.1 Introduction

The form of a channel in equilibrium is adjusted to the flows that are capable of conveying sediment supplied from upstream [e.g., *Mackin,* 1948]. Constraining the bedload that a given discharge (Q) conveys is central to river and reservoir management projects and landscape evolution models that estimate bedload budgets [e.g., *Howard et al.*, 1994; *Trush et al.*, 2000; *Ziegler et al.*, 2014]. In considering sediment budgets, Wolman and Miller [1960] identified the discharge most efficient at conveying a channel's sediment load, the effective discharge (Q_e), as the maximum product of flow frequencies and sediment transport rates. To apply this theory, Wolman and Miller [1960] used suspended sediment data from humid, lowland rivers that were near steady-state and capable of adjusting their boundaries.

While effective discharge has been commonly calculated based on the Wolman and Miller [1960] method [e.g., *Andrews and Nankervis,* 1995; *Emmett and Wolman,* 2001; *Sholtes et al.*, 2014], the original study also emphasized the importance of cumulative percentages of sediment transported over a range of discharges. In particular, they focused on the discharges in which 50 percent of the load was transported below (i.e., half-load discharge; $Q_{0.5}$) and 90 percent of the load transported below. Examining sediment magnitudes and flood event frequencies, Wolman and Miller [1960] found that transport occurring during the largest floods did not balance the rarity of the events. Instead, they found that the most cumulative transport was performed by flows associated with low to moderate frequency events (e.g., having recurrence intervals less than five to ten years). Beyond the interest of channel form maintenance, Wolman and Miller [1960] also proposed that flows responsible for rapid changes in channel shape may be associated with the rarer, extreme events, which has since been

supported by other studies in coarser alluvial systems [e.g., *Carling*, 1988; *Phillips*, 2002; *Lenzi et al.*, 2006b].

Regarding channel form, Wolman and Miller [1960] suggested that the most effective discharges at maintaining form corresponded to bankfull discharges (Q_{bf}). This conclusion was based on the maximum elevations of the aggrading inner banks being dependent on bankfull discharges. Since this work, effective discharges have since been commonly associated with bankfull conditions, which have frequent recurrence intervals of 1 to 2 years. Despite Wolman and Miller [1960] evaluating discharges effectiveness in terms of cumulative sediment transported, river management projects have mostly incorporated the concept of a single effective discharge comparable to bankfull discharge into channel design in an attempt to impose equilibrium conditions [e.g., *Shields et al.*, 2003; *Niezgoda and West*, 2007; *USDA-NRCS*, 2007].

The recurrence intervals of effective discharge in mountain stream settings remain unresolved. Magnitude-frequency analyses in these settings transitioned from suspended sediment to bedload due to the role that bedload has in channel form. The majority of studies in steep alluvial channels have inferred that effective discharges are comparable to bankfull floods [e.g., *Carling*, 1988; *Andrews and Nankervis*, 1995; *Emmett and Wolman*, 2001] (summarized in Table 4.1). However, recent a recent study by *Bunte et al.* [2014] concluded that the effective discharges in mountain streams corresponded to the rarest, most extreme events. Additionally, at some sites, the majority of a channel's bedload budget was found to be contributed by flows exceeding the identified effective discharges or bankfull discharges (e.g., Q_e or $Q_{bf} < Q_{0.5}$) [*Andrews and Nankervis*, 1995; *Emmett and Wolman*, 2001], whereas other sites have shown the opposite (Q_e or $Q_{bf} > Q_{0.5}$) [*Whiting et al.*, 1999; *Torizzo and Pitlick*, 2004] or that the discharges are the same (Q_e or $Q_{bf} \sim Q_{0.5}$) [*Emmett and Wolman*, 2001].

Variations in the previously described studies (Table 4.1) may be due to the sensitivity of results to the scaling of the bedload rates and flow distributions applied [e.g., *Bunte et al.*, 2014]. In the previous studies, some sites had neither bedload nor discharge records [*Whiting et al.*, 1999; *Torizzo and Pitlick*, 2004]. If locations had gauged discharges, then bedload

measurements were often unavailable, requiring the use of empirical transport formulas or regional scaling to sites with measurements [e.g., *Andrews and Nankervis*, 1995; *Torizzo and Pitlick*, 2004; *Bunte et al.*, 2014]. Due to the lack of field measurements, employing empirical formulas typically required assumptions of spatially constant entrainment thresholds. Recently, work has found that entrainment thresholds vary with bed slope [e.g., Ch. 3; *Lamb et al.*, 2008; *Scheingross et al.*, 2013].

If bedload measurements in these previous studies were available, then the streams were often ungauged or only a few years of gauged discharges were evaluated [e.g., *Carling*, 1988; *Whiting et al.*, 1999; *Bunte et al.*, 2014]. For these ungauged streams, regional flow duration curves were typically employed to establish the frequency of discharges. Available bedload measurements were typically collected using 7.6 cm Helley Smith samplers [e.g., *Whiting et al.*, 1999; *Emmett and Wolman*, 2001]. However, this bedload technique is frequently limited in coarse streams due to device capacity and size [e.g., *Johnson et al.*, 1977; *Vericat et al.*, 2006]. Additionally, bedload rates were typically measured for discharges up to only 1 to 2 times that of bankfull discharge, then were extrapolated to examine the significance of rarer flows that were much larger than those measured [*Carling*, 1988; *Whiting et al.*, 1999; *Emmett and Wolman*, 2001]. In using measurements from bedload traps at ungauged streams, *Bunte et al.* [2014] showed that scaling relations for the bedload discharge-water discharge were steeper than those than based on Helley Smith measurements. However, like Helley Smith measurements in some other studies, bedload data in *Bunte et al.* [2014] were also limited to low discharges (most were between only 0.1 and 1 times bankfull discharge). Over these lower discharges when bedload was measured, coarse alluvial streams are typically more supply limited than during the larger discharges when more of the bed is mobilized, which may have affected the bedload scaling over these lower, measured flows [e.g., *Carling*, 1988].

As summarized above, the current ability to predict effective discharges and bedload budgets in mountain streams is limited in part due to the lack of field constraints. With this motivation, the objective of this study is to address i) how sensitive are effective discharge

calculations to the scaling of bedload relations? ii) how does transport at effective discharge compare to the overall bedload budget of a mountain stream? iii) Can empirical transport formulas predict bedload volumes in mountain streams that approximate field constraints? A unique combination of field records, numerical flow modeling and empirical transport formulas were employed for these analyses. Flow modeling provided rare constraints on shear stress-discharge relations for a range of discharges, from low flows up to over six times bankfull. Empirical bedload formulas were modified to incorporate entrainment thresholds that were slope-dependent and validated at the field site, rather than assuming spatially constant values. The revised formulas predicted bedload volumes near a field constraint while the original formulas predicted volumes an order of magnitude larger than the field constraint. The bedload predictions indicate that effective discharges in the study stream correspond to moderate, high frequency flows. Predictions also demonstrate that the majority of bedload is transported by flows exceeding the effective discharge and that a broad range of flows transport significant fractions of the bedload budget. The findings highlight the importance of considering changes in bedload discharge scaling relations with discharge (particularly over higher discharges) and effects of channel morphology on entrainment thresholds when quantifying bedload budgets.

The chapter is organized as follows. First, the study area and its hydrology are described. Then, bedload models using tracer displacements and the empirical transport formulas are detailed. In the subsequent results section, effective discharges and bedload budgets predicted by the models are presented. The effective discharge and bedload predictions are then compared, and the significance of considering bedload scaling and channel morphology in magnitude-frequency analyses for mountain streams are examined.

4.2 Methods

4.2.1 STUDY SITE

4.2.2.1 Channel and watershed

Reynolds Creek is a snowmelt-dominated tributary to the Snake River and is located in the Owyhee Mountains in southwest Idaho. The USDA-Agricultural Research Service (USDA-ARS) manages Reynolds Creek and the surrounding land as part of the Reynolds Creek Experimental Watershed. The land around the stream is typical of semi-arid rangeland in the Western United States with vegetation mostly consisting of sagebrush and some junipers. Wolman point counts [1954] were performed at sites A through G within a 3 km section of this study (Figure 4.1a) and the resulting grain size distributions applied in the empirical transport models (further detailed in Section 4.2.2.3). The channel morphologies fluctuated between plane-bed, pool-riffle and step-pool reaches as well as some reaches with large unorganized boulders lined by heavy willow vegetation or bedrock sidewalls (Figures 4.1b,c,d).

4.2.2.2 Hydrology

Approximately 70 m downstream of location A was the USDA-ARS "Tollgate" gauging station (USDA-ARS station 116b). Discharges have been recorded at the Tollgate gauge since 1966 [*Northwest Watershed Research Center*, 2015]. Discharge in Reynolds Creek is snowmelt-dominated and the highest discharges occur between March and May. Much of the stream runs nearly dry during the late summer. The study area was downstream of the major tributaries that conveyed most snowmelt runoff from higher watershed elevations. Similar discharges measured at Tollgate gauging station and at a gauge 18 km downstream (USDA-ARS Station 36) suggested that discharges were similar along the 3 km study length [*Northwest Watershed Research Center*, 2015]. Discharges were collected from 1966 through 1993 over variable

intervals ranging from every 4.5 minutes to daily. Beginning in 1994, discharges were measured every 15 minutes.

A frequency distribution was fit to the mean daily flows over the 48 water years from 1966 to 2014 using similar methods that were previously applied to other snowmelt-dominated mountain streams in the western United States [e.g., *Segura and Pitlick*, 2010; *Bunte et al.*, 2014] (Figure 4.2a). The probability density function (*PDF*; units of days per yr per m^3s^{-1}) is well described by two power law fits:

$$PDF = \begin{cases} \alpha_1 Q^{k_1} \; for \; Q < Q_{brk} \\ \alpha_2 Q^{k_2} \; for \; Q \geq Q_{brk} \end{cases} \quad (4.1)$$

where α_1 was 44.1±4.1, k_1 was -1.11±0.14, Q_{brk} represented the discharge at the slope break between the power fits and was found to be 2.44 m^3s^{-1}, α_2 was 831±414.34 and k_2 was -4.39±0.44. Here, the ± uncertainty represents 95% confidence bounds. The flow frequency distribution calculated from the mean daily discharges from 1966 to 2014 were similar to distributions fit using the 15-minute records from 1994-2014 and the mean daily records from 1994-2014 (Figure 4.2a).

The slope-break discharge of 2.44 m^3s^{-1} had a recurrence interval of 1.45 yr and represented near bankfull conditions. Flood recurrence intervals using the maximum mean daily discharges recorded each year from 1966 to 2014 were also calculated (Figure 4.2b). The slope-break discharge was similar to estimates of bankfull discharge at location A, which was just upstream from the Tollgate gauge (Figure 4.1a). Bankfull discharge was independently estimated at Location A using several time lapse pictures (average of 2.49 m^3s^{-1}). Given that slope breaks in flow frequency distributions for snowmelt-dominated mountain streams typically are bankfull [e.g., *Dodov and Foufoula-Georgiou*, 2005; *Segura and Pitlick*, 2010; *Bunte et al.*, 2014] and that all the sites experienced similar discharges due to their locations being downstream of snowmelt tributaries (Section 4.2.2.2), it is expected that 2.49 m^3s^{-1} approximates bankfull discharges at the other locations. Thus, Q_{brk} appears to be a good measure of bankfull

discharge in this channel. The power law exponents k_1= -1.11 and k_2= -4.39 in Equation 4.1 are similar to those calculated in other snowmelt dominated mountain streams [*Bunte et al.*, 2014].

4.2.2 PREDICTIONS OF BEDLOAD TRANSPORT

4.2.2.1 Previous bedload tracer study in Reynolds Creek

Passive and active tracers were monitored in Reynolds Creek between 2011 and 2012 [Ch.2, Ch.3]. The passive RFID-embedded clasts were deployed in Reynolds Creek to quantify bedload displacement distances over several snowmelt periods. Stationary RFID antennas also installed at location A constrained bedload entrainment thresholds by recording when tracers passed through the reach. The passive tracers approximated the mean D_{50} of the channel (60 mm). The active tracers (artificial cobbles embedded with accelerometers) recorded motion and rest intervals for each tracer during spring 2012. The active tracers approximated the mean D_{80} of the channel (125 mm). Further descriptions of these tracer and antenna technologies have been previously detailed [Ch.2, Ch.3]. Entrainment thresholds constrained from the tracer datasets were used in the bedload prediction models described below.

4.2.2.2 Bedload model I: Mean tracer displacements

The displacement distances of the bedload tracers were found to correlate well with effective runoff volume (V_e) [Ch. 2]. Effective runoff volume is the hydrograph volume exceeding a discharge threshold for coarse bedload transport (Q_t) [e.g., *Lenzi et al.*, 2004]. Discharge was used as a proxy for shear stress by calculating effective runoff volumes over periods of interest. The discharge thresholds applied were i) 2 m^3s^{-1} based on the mobility records of the active tracers across the study area and ii) 1.4 m^3s^{-1} based on the mobility of the passive tracers recorded by the stationary antennas [Ch. 2]. Mean displacements of the bedload tracers ($\langle X \rangle$) were shown to increase linearly with effective runoff, where

$$\langle X \rangle = 0.0009 \times V_e \text{ for } Q_t = 2 \text{ m}^3\text{s}^{-1} \quad (4.2)$$

and

$\langle X \rangle = 0.0005 \times \forall_e$ for Q_t=1.4 m^3s^{-1} (4.3)

The use of Equations 4.2 and 4.3 in the bedload predictions are designated herein as model I. For model I, the effective runoff (units of m^3) were estimated for each discharge interval (Q_i) up to the maximum mean daily value of 14.9 m^3s^{-1}, over the 1966-2014 period [*Northwest Watershed Research Center*, 2015]. Effective runoff volumes were calculated each discharge interval in model I as

$$\forall_e = (Q_i - Q_t)t_{Q_i} \; for \; Q_i > Q_t \quad (4.4)$$

where t_{Q_i} represents the duration in seconds of each discharge interval. The discharge intervals (ΔQ) were 0.1 m^3s^{-1} and duration for each discharge interval were calculated over the 48 years as

$$t_{Q_i} = f_{t_{Q_i}} \times \left(48 \; yrs \times \frac{365.25 \; days}{1 \; yr} \times \frac{24 \; hrs}{1 \; day} \times \frac{60 \; min}{1 \; hr} \times \frac{60 \; sec}{1 \; min}\right) \quad (4.5)$$

where $f_{t_{Q_i}}$ represents the frequency, or fraction of time, at each discharge interval. The frequency of each discharge was constrained with the mean daily flow frequency distribution (Equation 4.1; Figure 4.2a) as

$$f_{t_{Q_i}} = \begin{cases} 44.1Q^{-1.11}\Delta Q\left(\frac{1 \; yr}{365.25 \; days}\right) \; for \; Q < 2.44 \; m^3s^{-1} \\ 831Q^{-4.39}\Delta Q\left(\frac{1 \; yr}{365.25 \; days}\right) \; for \; Q \geq 2.44 \; m^3s^{-1} \end{cases} \quad (4.6)$$

4.2.2.3 Bedload models II and III: Empirical transport formulas

4.2.2.3.1 Shear stress modeling

The channel's hydraulic conditions were modeled over a range of discharges using HEC-RAS, a flow modeling tool developed by the US Army Corps of Engineers. For each modeled discharge (Q_m), shear stresses (τ_{Q_m}) were calculated at channel cross sections using steady and uniform flows assumptions as

$$\tau_{Q_m} = \rho g R S_{EGL} \quad (4.7)$$

where ρ is the density of water (assumed to be 1000 kg m^{-3}), g is gravity, R is the hydraulic radius at a given cross section and S_{EGL} is the calculated slope of the energy grade line at a given

cross section. The cross-sectional channel geometries were imported into the HEC-RAS models by extracting cross sections from a 1 m airborne LiDAR digital elevation model s[*Northwest Watershed Research Center*, 2009] (detailed in Ch. 3). Shear stress results were averaged using a moving window of 10 m.

Shear stress calculations were performed for each 0.1 m^3s^{-1} discharge interval modeled from 0.3 to 14.9 m^3s^{-1}. Discharges below 0.3 m^3s^{-1} magnitudes were not modeled due to HEC-RAS instabilities at extremely low flows. These low flows were not expected to be associated with significant bedload transport based on minimum discharges recorded by the passive tracers and stationary antennas (Section 4.2.2.2). HEC-RAS calculated widths and Froude numbers (*Fr*) over the discharges suggested that the models approximated natural flow conditions [Ch. 3].

4.2.2.3.2 Sites of interest

Bedload transport was predicted at seven specific sites, locations A through G, where surface grain size distributions were measured (Figure 4.1a). The reach at location A and the 700 km section upstream of Location A were in a flatter, wider valley compared to the narrower, canyon setting that locations B to G were in. Among the sites, the local bed slopes that were calculated over the length of pebble counts [*Wolman*, 1954] (approximately two channel widths, 10 m) varied between 0.011 and 0.042 m/m (Figure 4.3a; Table 4.2). The pebble counts provided grain size distributions of the bed surface. The D_{50} among the sites ranged from 51 mm to 90 mm (Figure 4.3b; Table 4.2). Location B had the steepest bed slope and the coarsest grain size distribution, while locations E and F had the flattest bed slopes and the finest grain size distributions.

The HEC-RAS models provided shear stress constraints over the discharges on record (Figure 4.3.c). Shear stresses were the highest at location B. Shear stresses scaled with discharge as $\tau \sim Q^j$, over the seven sites with the mean ± standard error being j=0.44±0.05 (j-values for each location given in Figure 4.3c caption). Using the grain size distributions of each

site (Figure 4.3b), the modeled shear stresses for each discharge (Figure 4.3c) were normalized with grain weight per area to calculate a dimensionless shear stress, or Shields number (τ^*_{i,Q_m}). For each clast diameter (*D*) of each *i*th size class and shear stress result, Shields numbers were calculated as

$$\tau^*_{i,Q_m} = \frac{\tau_{Qm}}{(\rho_s - \rho) g D_i} \quad (4.8)$$

where ρ_s represents the density of sediment, assumed to be 2650 kg/m^{-3}.

The transport stages of the median grain size ($\emptyset_{50,Q_m}$) at each site were next calculated as

$$\emptyset_{50,Q_m} = \frac{\tau^*_{50,Qm}}{\tau^*_{c,50}} \quad (4.9)$$

where $\tau^*_{c,50}$ is the critical Shields number corresponding to the entrainment threshold of the D_{50} sized clasts. For location A, the $\tau^*_{c,50}$ was constrained by the records of the stationary antennas as 0.061 [Ch. 3]. Because stationary antennas were only installed at Location A, the $\tau^*_{c,50}$ values at the other six sites were constrained with the bed slope relation presented in Chapter 3 as

$$\tau^*_{c,50} = 0.52 S^{0.51} \quad (4.10)$$

This slope-dependent relation was based on transport thresholds gleaned from the active tracers deployed in Reynolds Creek and bedload measurements from other studies [compiled in *Buffington and Montgomery*, 1997; compiled in *Mueller et al.*, 2005; *Scheingross et al.*, 2013].

For most sites, the transport stage-discharge trends were comparable (Figure 4.3d). The unique morphological conditions of locations E and F caused the transport stage-discharge trends modeled for the two sites to not collapse well with the other sites. While Locations E and F have the lowest local bed slopes (Figure 4.3a; Table 4.2) and finest grain size distributions (Figure 4.3b; Table 4.2), the predicted S_{EGL} results calculated in HEC-RAS were steeper than the local bed slopes (e.g., at Q=2.4 m^{3}s^{-1}, S_{EGL} was 0.03 m/m at both sites). Transport capacities at these locations were elevated because bank confinement from dense willows over narrow banks and the overall canyon settings did not allow for channel widening to balance the higher S_{EGL} results (Equation 4.7).

4.2.2.3.3 Parker [1990a] transport function

A modified version of the transport function proposed by Parker [1990a] was applied to estimate bedload transport rates in Reynolds Creek. The Parker [1990a] function was derived from vortex bedload trough in Oak Creek, Oregon. Comparable to Reynolds Creek, Oak Creek was a 6 m wide gravel channel with a surface D_{50} of 54 mm [*Milhous*, 1973]. Transport stages for the D_{50} clasts modeled in HEC-RAS (Equation 4.9) were first used to calculate a straining coefficient (ω_{Q_m}). The straining coefficient characterized the degree of armoring that a bed may experience, decreasing from 1 as transport stages increase, thus reducing the effects of armoring. The straining coefficients were calculated for each modeled discharge at each site as

$$\omega_{Q_m} = 1 + \frac{\sigma_\emptyset}{\sigma_0(\emptyset_{50,Q_m})}\left[\omega_0\left(\emptyset_{50,Q_m}\right) - 1\right] \quad (4.12)$$

where the $\sigma_0(\emptyset_{50,Q_m})$ and $\omega_0\left(\emptyset_{50,Q_m}\right)$ were graphical functions based on the $\emptyset_{50,Q_m}$ values [tabulated results available from *Parker*, 1990b], and $\sigma_\emptyset$ is the arithmetic standard deviation of the bed's grain size distribution. In the original Parker [1990a], $\tau^*_{c,50}$=0.039 was applied to calculate $\emptyset_{50,Q_m}$ (Equation 4.9). However, in this study, $\tau^*_{c,50}$ modified to field constrained values based on bed-slope (Equation 4.10). The use of the original 0.039 value at all sites is further explored in Section 4.4.3.2. Using the sediment phi scale, the arithmetic standard deviations were calculated using

$$\sigma_\emptyset = \sqrt{\sum_{i=1}^{N}\left(\frac{\ln(D_i/D_{50})}{ln2}\right)^2 F_i}, \quad (4.13)$$

where F_i is the fraction of bed sediment in the *i*th grain size class based on the pebble counts.

The calculated straining coefficients (Equation 4.12) were then applied to quantify the transport stage for the other grain sizes ($\emptyset_{i,Q_m}$) at each discharge. Transport stages were calculated as

$$\emptyset_{i,Q_m} = \omega\emptyset_{50,Q_m}\left(\frac{D_i}{D_{50}}\right)^{-(1+b)} \quad (4.14)$$

where the *b*-exponent in the Parker [1990a] model was -0.905, indicating near equal mobility conditions. The *b*-exponent applied in the original Parker [1990a] formula was kept in the model

because it was similar to the uncertainty bounds on the b-exponent constrained by the stationary antennas (95% confidence bounds of -0.94 to -1.19 [Ch. 3]).

Based on the transport stage calculations in Equation 4.14, the bedload function $G(\emptyset_{i,Q_m})$ was then evaluated depending on three transport stage conditions as

$$G(\emptyset_{i,Q_m}) = \begin{cases} 5474\left(1-\frac{0.853}{\emptyset_{i,Q_m}}\right)^{4.5} \; for \; \emptyset_{i,Q_m} > 1.59 \\ \exp\left[14.2(\emptyset_{i,Q_m}-1) - 9.28(\emptyset_{i,Q_m}-1)^2\right] \; for \; 1 \le \emptyset_{i,Q_m} \le 1.59 \\ \emptyset_{i,Q_m} \; for \; \emptyset_{i,Q_m} < 1 \end{cases} \quad (4.15)$$

Transport predicted from Equation 4.15 is designated herein as “model II”.

This original form of $G(\emptyset_{i,Q_m})$ (Equation 4.15) permits nominal transport even when transport stages for a given grain sizes is below 1 (i.e., $\emptyset_{i,Q_m} < 1$). The snowmelt regime of Reynolds Creek causes the stream to be at low flow conditions for the majority of time (Figure 4.2a). To evaluate the effect of nominal transport accumulating over these low stages, the original Equation 4.15 was also modified in “model III” whereby nominal transport was prevented at low stages. Models II and III are also used to compare the effects that predictions of nominal transport at low stages have on the scaling of water discharge-bedload rate relations. From the stationary antenna results [Ch. 3], the minimum recorded transport stage was 0.57 and corresponded to clast that was 2.7 times larger than the reach’s D_{50}. Thus, the alternative bedload function in model III depended on four transport stage conditions as

$$G(\emptyset_{i,Q_m}) = \begin{cases} 5474\left(1-\frac{0.853}{\emptyset_{i,Q_m}}\right)^{4.5} \; for \; \emptyset_{i,Q_m} > 1.59 \\ \exp\left[14.2(\emptyset_{i,Q_m}-1) - 9.28(\emptyset_{i,Q_m}-1)^2\right] \; for \; 1 \le \emptyset_{i,Q_m} \le 1.59 \\ \emptyset_{i,Q_m} \; for \; 0.57 \le \emptyset_{i,Q_m} < 1 \\ 0 \; for \; \emptyset_{i,Q_m} < 0.57 \end{cases} \quad (4.16)$$

The dimensionless transport rates for each discharge (W^*_{si,Q_m}) were subsequently calculated for models II and III at each location as

$$W^*_{si,Q_m} = 0.00218 \times G(\emptyset_{i,Q_m}) \quad (4.17)$$

Being a surface size-based empirical formula, Equation 4.17 applied in both models II and III assumes that supply was limited by the proportion of grains of a given size class that are

found on the bed (determined here by point counts). However, when Equation 4.17 was used with $G(\emptyset_{i,Q_m})$ from model II (Equation 4.15), the model assumed that sediment supply was not limited by factors affecting bed stability, such as clast packing and imbrication. Conversely, the $G(\emptyset_{i,Q_m})$ calculations from model III (Equation 4.16) assumed that sediment supply was limited by imposing conditions of no transport at low stages. The differences between these models were subsequently examined because sediment supply is often limited in mountain streams [e.g., *Yager et al.*, 2007; *Hassan et al.*, 2008; *Wohl*, 2010].

The dimensionless transport rates enabled the calculations of volumetric bedload transport rates per unit width (q_i) for each discharge and *i*th grain size class as

$$q_{i,Q_m} = \frac{W^*_{si,Qm}\left(\frac{\tau_{Qm}}{\rho}\right)^{1.5} F_i}{\left(\frac{\rho_S-\rho}{\rho}\right)g} \quad (4.18)$$

At each site, the HEC-RAS modeled channel widths for each flow (w_{Q_m}) were combined with Equation 4.18 to estimate bedload transport rates for each *i*th size class ($Q_{B,i}$) as

$$Q_{B,i,Q_m} = q_{i,Q_m} \times w_{Q_m} \quad (4.19)$$

The total bedload discharge ($Q_{B,total}$; units m^3s^{-1}) over all *N* number of coarse grains sizes were then calculated as

$$Q_{B,total,Q_m} = \sum_{i=1}^{N} Q_{B,i,Q_m} \quad (4.20)$$

Predicted bedload volumes contributed by each modeled discharge ($V_{B,total,Q_m}$; units m^3) were calculated over the discharge intervals as

$$V_{B,Q_m} = Q_{b,total,Q_m} \times t_{Q_m}. \quad (4.21)$$

where duration at each discharge interval (t_{Q_m}; units of seconds) was determined by applying the flow frequency distribution (Figure 4.2a; Equations 4.5 and 4.6). Total predicted bedload volumes ($V_{B,total}$) and bulk bedload volumes ($V_{B,bulk}$) were predicted across all discharges over the 48-year record as

$$V_{B,total} = \sum_{Q_m=0.3\ m^3s^{-1}Q_{min}}^{Q_m=14.9\ m^3s^{-1}} V_{B,Q_m} \quad (4.22)$$

and

$$V_{B,bulk} = \frac{V_{B,total}}{(1-\varepsilon)}, \quad (4.23)$$

where ε is porosity. Porosity was assumed to be 0.35 for unconsolidated, coarse alluvial sediment [*Yolcubal et al.*, 2004].

4.3 Results

4.3.1 Model I: Tracer Displacement Distances

The effective runoff relations from the passive tracers (Equations 4.2 and 4.3) were used with the frequency distribution (Equation 4.1; Figure 4.2a) to predict the fraction of displacement that each discharge interval contributed toward total displacements (i.e., $\langle X \rangle / \langle X \rangle_{total}$) (Figure 4.4a). When applying the discharge threshold of 1.4 m^3s^{-1} for the effective runoff calculations (Equation 4.2), the discharge with the maximum $\langle X \rangle / \langle X \rangle_{total}$, i.e., the effective discharge, was 2.4 m^3s^{-1}. The effective discharge increased slightly to 2.6 m^3s^{-1} when the discharge threshold was raised to 2 m^3s^{-1} (Equation 4.3). Both these effective discharges approximated the 2.44 m^3s^{-1} discharge that corresponded to the break in the power scaling of the flow frequency distribution.

The same data are also presented as a cumulative distribution to emphasize that much of the transport actually occurs at discharges higher than the calculated effective discharges (Figure 4.3b; Table 4.2). For the discharge threshold of 1.4 m^3s^{-1}, effective discharge of 2.4 m^3s^{-1} had a cumulative fraction of total transported displacements (*CFT)* of 0.31 and the half-load discharge was 2.9 m^3s^{-1}. For the discharge threshold of 2 m^3s^{-1}, effective discharge of the 2.6 m^3s^{-1} had a lower *CFT* (0.18) and a higher half-load discharge (3.6 m^3s^{-1}). The ratios of effective discharge to half-load discharges ($Q_e/Q_{0.5}$) for the 1.4 m^3s^{-1} and 2 m^3s^{-1} thresholds were 0.83 and 0.72, respectively.

4.3.2 MODELS II AND III: MODIFIED PARKER [1990A] TRANSPORT FORMULAS

4.3.2.1 Transport rates

Models II (transport permitted at low stage) and III (all transport prevented below transport stage $\emptyset_{i,Q_m} < 0.57$) predicted generally comparable bedload transport rates among the seven sites (Figures 4.5a,b). When transport was permitted at low transport stages, all sites predicted nominal transport to occur at the lowest modeled discharge (0.3 m^3s^{-1}; Figure 4.5a). For model III, only locations A and C showed nominal transport at the lowest modeled discharge interval (Figure 4.5b). Model III predicted nominal transport to begin for the smallest clast bin (2 to 7 mm grains) when discharge was 0.4 m^3s^{-1} at locations E and G, and near 1 m^3s^{-1} at locations B, D and F (Figure 4.5b). Transport rates at locations E and F were predicted to be higher at higher discharges than the other sties due to differences in their discharge-transport stage scaling (e.g., Figure 4.3d).

4.3.2.2 Bedload volumes and effective discharges

While the models unsurprisingly predicted that locations with higher bedload rates also had higher bedload volumes (Figures 4.5c,d), the objective of the analyses presented below is to compare overall trends rather than volumetric magnitudes because constraints on bedload volumes were not known over the 48-year period. Similar to normalizing the displacements predicted in model I (Section 4.3.1), the bedload volumes estimated for each discharge interval were normalized by the total volume predicted (i.e., volumetric bedload fractions, $V_{B,Qm}/V_{B,total}$). Overall trends in the volumetric bedload fractions with discharge were similar between models II and III over the larger discharges, but varied over the smaller discharges (Figures 4.5e,f). As expected, within the individual sites, the volumetric fractions predicted from model II (which permitted transport at all transport stages) were larger at lower discharges than those predicted with model III.

The discharges with the maximum $V_{B,Qm}/V_{B,total}$ values, i.e., the effective discharge, were generally similar among the locations for models II and III (Figures 4.5e,f; Table 4.2). The magnitudes of the effective discharges ranged from 2.4 m^3s^{-1} and 2.5 m^3s^{-1} for sites B-D and G, which corresponded to a 1.45 yr recurrence intervals. This range was comparable to the 2.44 m^3s^{-1} break in slope of the flow frequency distribution (Figure 4.2a) and the bankfull discharge (detailed in Section 4.2.2.2). Due to the scaling of bedload discharge-water discharge relations at location A, models II and III predicted a lower effective discharge at location A (Q_e=1.1 m^3s^{-1}) and 1.2 m^3s^{-1}, respectively), but the corresponding broader $V_{B,Qm}/V_{B,total}$ curves for location A fell similarly to the other locations (i.e., at 2.4 m^3s^{-1}). Due to the higher magnitude and steeper bedload discharge-water discharge relations predicted at locations E and F for the larger discharges (Figures 4.5e,f), the effective discharges at locations E and F were also larger than the other sites, respectively 3.4 m^3s^{-1} and 5.5 m^3s^{-1}. While these effective discharges were larger, the recurrence intervals for these discharges remained less than 5 years (respectively 2.12 and 4.3 years).

4.3.2.3 Cumulative fractions transported and half-load discharges

Similar to the tracer displacement predictions (model I; Section 4.3.1), models II and III also showed that the majority of transport was contributed from flows that exceeded the predicted effective discharges at all sites (Figures 4.5g,h; Table 4.2). While the effective discharges did not change within each site between models II and III, the results showed that, within each site, the cumulative fractions transported below the effective discharges associated were up to a factor of two larger for model II than model III. This trend of the effective discharge *CFT* results being larger for model II was expected given that model II permitted smaller flows to contribute more sediment than model III.

All predicted half-load discharges exceeded the effective discharges, and varied from 2.5 to 7.4 m^3s^{-1} among the sites (Figures 4.5g,h; Table 4.2). The recurrence interval for the half-load

discharges varied from 1.46 to 10.44 years. The mean ratios of $Q_e/Q_{0.5}$ ± standard errors across the sites were 0.31±0.05 for model II and 0.24±0.03 for model III. Model II predicted total bedload volumes at locations A, E, F and G that were less than 3% larger than volumes predicted by model III, and the respective half-load discharges at these sites also differed by less than 3% between models II and III. Conversely, model II predicted total bedload volumes at locations B, C and D that were 7% to 25% than volumes predicted by model III, and the respective half-load discharges at these sites for models II and III differed by 11% to 74%.

4.4 Discussion

In the following section, effective discharge and the effects of bedload scaling are first explored (Sections 4.4.1). Then, the relative contribution of effective discharge to bedload budgets are discussed (Sections 4.4.2). The applicability of the Parker [1990a] is also explored in the context of predicted volumes versus volumes constrained in the field, and the revision $\tau^*_{c,50}$ based on local channel morphology (Section 4.4.3). Model limitations are also examined (Section 4.4.4) and the study's approach reviewed (Section 4.4.5).

4.4.1 Effective discharge and bedload scaling

The predictions of effective discharge from the displacement-effective runoff method (model I) and the transport formulas derived from field revised Parker [1990a] formulas (models II and III) were generally similar. Most values ranged between 2.4 and 2.6 m^3s^{-1} (Figures 4.4 and 4.5; Table 2). The recurrence interval of the effective discharges between 2.4 and 2.6 m^3s^{-1} were between 1.5 and 2.4 years, indicating that both methods predict effective discharge in Reynolds Creek to be associated with moderate, high frequency flows rather than rarer, more extreme events. Models II and III only predicted higher effective discharges at locations E and F (3.4 m^3s^{-1} and 5.5 m^3s^{-1}, respectively) but, the recurrence intervals for the higher effective discharges at locations E and F remained moderate (2.1 and 4.3 years, respectively).

The computed effective discharges contradict the unique conclusions by *Bunte et al.* [2014] that motivated this study. *Bunte et al.* [2014] suggested that effective discharges in mountain streams were associated with the highest, rarest events. Instead, the results are consistent with the other studies showing that effective discharges in mountain streams correspond to moderate, high frequency flows (outlined in Table 4.1) [*Andrews and Nankervis,* 1995; *Whiting et al.*, 1999; *Emmett and Wolman*, 2001; *Torizzo and Pitlick*, 2004; *Lenzi et al.*, 2006b]. The correlation of the predicted effective discharge with bankfull discharge (Q_{bf} detailed in Section 4.2.2.2) is also consistent with several previous studies of coarse alluvial channels [*Andrews and Nankervis*, 1995; *Emmett and Wolman*, 2001; *Torizzo and Pitlick*, 2004; *Lenzi et al.*, 2006b]. To explore the difference between the Reynolds Creek results and those presented by *Bunte et al.* [2014], similarities and differences of the two studies is further explored below.

The scaling of the flow frequency distributions and bedload discharges directly determine the magnitude of the effective discharges because effective discharges are determined as the maximum product of flow frequency distributions and bedload discharges-water discharge relations. The scaling of the flow frequency distribution for Reynolds Creek with a_1 as -1.11±0.14 and a_2 as -4.39±0.44 (Equation 4.1) overlaps with the scaling from the 41 gauged mountain streams that *Bunte et al.* [2014] studied. *Bunte et al.* [2014] found that a_1 ranged from -2.40 to -0.65 and a_2 ranged from -7.45 to -3.23. These gauged streams did not have bedload measurements, so *Bunte et al.* [2014] applied bedload relations from comparable streams based on bedload measurements collected over discharges up to 1.5 times bankfull discharge and extrapolated to larger discharges. The bedload discharge (Q_B) relations applied to those 41 streams had the form of

$$Q_B = \beta Q^{b_1} \tag{4.24}$$

where the b_1-exponents ranged from 2 to 20 (most were between 3 and 10).

With these flow frequency and bedload scaling results, *Bunte et al.* [2014] found that i) all streams showed that $a_1 + b_1 > 0$, indicating that product of the flow frequency and bedload

relations were positive for discharges less than Q_{brk}, and ii) that most streams also showed that $a_2 + b_1 > 0$, indicating that product of the flow frequency and bedload relations remained positive for discharges exceeding Q_{brk}. The positive product for both flows below and above Q_{brk} for most streams caused the effective discharges of those streams to correspond to the maximum discharges evaluated. Should instead $a_2 + b_1$ had been negative, then *Bunte et al.* [2014] would have found the effective discharge to be less than the maximum discharges on record.

For comparison to the bedload scaling that *Bunte et al.* [2014] employed, power-law regression is also performed on the predicted bedload discharges by models II and III (shown in Figures 4.5 a,b) for discharges between 0.5and 3.8 m3s-1 (i.e., $0.2Q_{bf}$ and $1.5Q_{bf}$; fitting exponent b_1 in Equation 4.24). Scaling was also performed for discharges exceeding the range measured by *Bunte et al.* [2014] (i.e. Q>$1.5Q_{bf}$, and the scaling exponent designated as b_2). For the discharges less than $1.5Q_{bf}$, Model III indicated higher b_1 scaling exponents (i.e. more steep bedload discharge-water discharge relations) than Model II (Figures 4.6a,b; Table 4.3). The b_1 scaling at all sites using model III were in the range calculated by *Bunte et al.* [2014], and had a mean ± standard error of 4.91±0.82. The standard errors are represented by error bars in Figures 4.6a,b. Conversely, Model II b_1 exponents were all less than 2 and had a mean ± standard error of 1.73±0.23. The b_1 scaling predicted by model III overlap with the *Bunte et al.* [2014] findings for discharges up to $1.5Q_{bf}$. The overlap suggests that prevention of transport at low stages in model III better approximates bedload transport at low stages in mountain streams than model II (point further discussed in Section 4.4.4). However, the Reynolds Creek results overlapping in the lower end of the *Bunte et al.* [2014] may be due to most of the *Bunte et al.* [2014] measurements having been collected from 0.1 Q_{bf} to Q_{bf}, which may have slightly steeper scaling than if measurements up to 1.5 Q_{bf} had been available (discussed below).

Due to b_1 from model III being generally comparable to the calculated *b*-exponents by *Bunte et al.* [2014], the remaining discussion on scaling focuses on model III. Should the effective discharge analyses had been based on the b_1 bedload scaling across all the discharges

along with the k_1 and k_2 scaling from the flow duration curve (Equation 4.1), the majority of the Reynolds Creek sites would have demonstrated similar findings to most of the streams analyzed by *Bunte et al.* [2014]. The scaling showed that $k_1 + b_1 > 0$ for all sites, and rather than becoming $k_2 + b_1 < 0$ for discharges exceeding Q_{brk}, locations B, D, E and F continued to show that $k_2 + b_1 > 0$ like *Bunte et al.* [2014]. However, the scaling exponents decreased when flows exceeded $1.5Q_{bf}$, i.e. $b_2 < b_1$ for all sites except for locations A and C, which remained relatively low (Figure 4.6b; Table 4.3). The b_2 values ranged from 2.45 to 3.57, with a mean ± standard error of 2.95± 0.14. These differences in b_1 and b_2 depending on discharge show that, for all sites, $k_1 + b_1 > 0$ and $k_2 + b_1 < 0$, which is indicative of effective discharges corresponding to more moderate, high frequency events. This trend suggests that the limitations in the bedload measurements available to *Bunte et al.* [2014] may have been too high to be extrapolated to discharges exceeding $1.5Q_{bf}$, and subsequently affected their magnitude-frequency results.

4.4.2 EFFECTIVE DISCHARGE RELATIVE TO TOTAL BEDLOAD BUDGETS

If the cumulative distributions of bedload predictions had shown sharp changes in slope around each effective discharge (Figures 4.4b and 4.5g,h), then effective discharge would have signified that effective discharges are related to significant changes in bedload budgets. However, the lack of notable slope differences at the effective discharges caused by the generally smooth $\langle X \rangle / \langle X \rangle_{total}$ and $V_{B,Qm}/V_{B,total}$ curves suggests that a broader range of discharges beyond a single value of effective discharge significantly contributes to the bedload budget of Reynolds Creek. As channels adjust to convey the sediment supplied from upstream [e.g., *Mackin*, 1948], the consistent finding that the majority of the bedload volumes predicted by models I, II and III were contributed by flows that the exceeded effective discharges further demonstrates that a single discharge, such as effective discharge, cannot account for the maintenance of channel form of a mountain stream. Despite differing methods, *Andrews and Nankervis* [1995] also found that the majority of transported bedload was attributed to flows exceeding effective

discharges. Additionally, location A had characteristics most comparable to the steepest channel studied with bedload measurements in the *Emmett and Wolman* [2001] study, and both sites predicted similar $Q_e/Q_{0.5}$ (models II and III respectively having 0.83 and 0.8, and *Emmett and Wolman* [2001] showing 0.83). The previous study that reported the majority of transport occurring over flows less than effective discharges had to scale ungauged streams to regional flow frequency distributions and used the Parker [1982] formula with a spatially constant $\tau^*_{c,50}$=0.033 [*Torizzo and Pitlick*, 2004]. The methods may have contributed to the divergent findings since effective discharge is sensitive to the scaling of flow frequency distributions and bedload discharge relations (e.g., Section 4.4.1).

4.4.3 APPLICABILITY OF PARKER [1990A] MODEL

4.3.3.1 Field constraint

A crude estimate of the sediment deposit that filled the Tollgate station gauging pool during the spring 2012 snowmelt (Figure 4.1e) was compared to bedload volumes predicted by models II and III at location A to evaluate the appropriateness of the two models for the channel. Location A was approximately 70 m upstream from the pool and time lapse photos of location A and the pool area constrained the timing of when the pool was filled. The pool's bedload trap efficiency was estimated to be twenty-five percent during spring 2012 based on the percentage of passive RFID tracers that were found in the pool following the Spring 2012 season versus those that passed through the pool.

Comparison of total station surveys suggested that the deposit from the spring 2012 flows was more than 18.5 m^3 of sediment and less than 58.5 m^3. The minimum accumulated bulk volume was based on differencing 0.1 m x 0.1 m surface grids created in Matlab from i) a March 2012 survey where the channel thalweg on each side of the pool deposit was surveyed every 0.1 m and the pool deposit was surveyed every few square meters and ii) a June 2012 survey where the channel thalweg on each side of the pool deposit was surveyed every 0.1 m. Because the

June 2012 survey was only of the thalwegs flowing into the two Tollgate station inlets, the June 2012 surface included the lower elevations of the pool deposit from the March 2012 survey to constrain the 18.5 m^3 minimum estimate. The maximum accumulated bulk volume of 58.5 m^3 was based on differencing the March 2012 surface grid from a June 2012 grid that assigned the elevation of the pool points to the elevation of a control point that was higher than the entire deposit.

With the trap efficiency and survey constraints, the transported bulk volume at location A during the spring 2012 flow was estimated to be larger than 74 m^3 and less than 234 m^3 (i.e., 18.5 m^3/0.25 and 58.5 m^3/0.25). The transport formula using models II and III both predicted a bulk volume of approximately 95 m^3 during spring 2012 (93.1 m^3 and 94.5 m^3, respectively). This cumulative transport calculated with the modified Parker [1990a] models is broadly consistent with the deposit estimate, suggesting that the revised application of the Parker [1990a] formula was reasonable for the site.

The general alignment contrasts with previous indications that empirical transport formula models could be several orders of magnitude larger than bedload rating curves suggested [e.g., *Bathurst*, 1987; *Gomez and Church*, 1989; *Yager et al.*, 2007; *Barry et al.*, 2008]. Several factors may have contributed to models II and III generally predicting the pool deposit reasonably well. First, the continuous, during-flood antenna records provided field measured transport thresholds that could be incorporated into the models. Due to technological limitations, many previous field efforts relied on inferring transport thresholds from examining field conditions after floods, such as assuming that thresholds of the largest tracer clasts mobilized correspond to the peak discharge of the previous flood [e.g., *Andrews*, 1983; *Lenzi et al.*, 2006a; *Mao et al.*, 2008; *Yager et al.*, 2012a; *Scheingross et al.*, 2013]. Depending on the methods employed, interpreted thresholds could vary greatly [e.g. *Buffington and Montgomery*, 1997] and uncertainties in threshold values can significantly impact bedload predictions [e.g., *Barry et al.*, 2004; *Recking et al.*, 2012]. Thus, the consistency of the $\tau^*_{c,50}$ provided by the antenna

records throughout the spring 2012 season [Ch. 3] likely represented the transport conditions at the reach fairly well.

4.4.3.2 Model revision based on channel morphology

Due to the scarcity of bedload measurements in steep channels, assuming a spatially constant $\tau^*_{c,50}$ value ranging from 0.03 to 0.04 was practiced in previous magnitude-frequency analyses for mountain watersheds (Table 4.1) [e.g., *Andrews and Nankervis*, 1995; *Torizzo and Pitlick*, 2004; *Thompson and Croke*, 2008]. However, evidence exists that $\tau^*_{c,50}$ is higher for steeper channels [e.g., Ch.3; *Mueller et al.*, 2005; *Yager et al.*, 2012; *Scheingross et al.*, 2013], and at the sites investigated in this study, the slope-dependent $\tau^*_{c,50}$ values ranged from 0.051 to 0.102 (Table 4.2). Additional calculations of bedload transport rates are presented again using the constant $\tau^*_{c,50}$ value of 0.039 in the original Parker [1990a] formula (Section 4.2.2.3.3) to explore how excluding the effect of channel morphology on $\tau^*_{c,50}$ may change bedload budgets.

As expected, the use of the lower $\tau^*_{c,50}$ caused transport rates and volumes to be higher than when the slope-dependent $\tau^*_{c,50}$ were used, sometimes up to several orders of magnitude higher (e.g., location B in Figure 4.7b). The higher transport rates also diminished the differences between the model II and III bedload volumes; thus, for conciseness, only model II is plotted in Figures 4.7a,b. The increased volume predicted by the lower $\tau^*_{c,50}$ value also predicts an extensive increase in bulk bedload estimate for the spring 2012 season. The lower $\tau^*_{c,50}$ value predicted sediment at location A over spring 2012 to be 2,064 m^3 for both models II and III, significantly exceeding the 80 m^3 field constraint.

Despite the lower $\tau^*_{c,50}$ value increasing the transport stages, rates and volumes (Figures 4.7a,b), the higher transport rates over the largest discharges remained insufficient to balance the rarity of their occurrence (Figure 4.7c). Thus, like the slope-dependent $\tau^*_{c,50}$ results, the relative bedload volumes predicted using the spatially lower $\tau^*_{c,50}$ value still caused the predicted effective discharges to correspond to moderate, high frequency flows at all locations. This

agreement of the magnitude-frequency trends with slope-dependent $\tau^*_{c,50}$ results suggests that the previous studies that employed similar spatially constant $\tau^*_{c,50}$ values over comparable channel gradients likely correctly identified the trend of effective discharges being moderate, high frequency magnitudes. However, channels steeper than Reynolds Creek can have significantly higher $\tau^*_{c,50}$values [e.g., *Scheingross et al.*, 2013]; thus, such an assumption of a lower, spatially constant $\tau^*_{c,50}$ may not demonstrate comparable trends for steeper streams.

The degree of change in the effective discharges predicted using the lower $\tau^*_{c,50}$ versus those applied in models II and III varied slightly among the sites (Figure 4.7d). At location D, the higher transport stages at the higher discharges increased the effective discharge from 2.4 m^3s^{-1} to 2.8 m^3s^{-1}. Conversely, at locations E and F, the shift in higher and steeper bedload rates over smaller discharges caused the magnitudes of the respective effective discharges at the two sites to decrease from 3.4 m^3s^{-1} and 5.5 m^3s^{-1} to 2.5 m^3s^{-1} and 3 m^3s^{-1}. At locations A, B, C and G, the higher bedload rates over the larger discharges were not sufficient to significantly change the magnitudes of the effective discharge.

The observed variations in effective discharges with the lower $\tau^*_{c,50}$ compared to the slope-dependent $\tau^*_{c,50}$ highlight potential uncertainties in channel-engineering designs that identify effective discharges without consideration of local morphologies. For river management projects that engineer channel forms based on effective discharges calculations [e.g., *Andrews and Nankervis*, 1995; *Shields et al.*, 2003], an underestimated effective discharge could result in the channel being too small. Should effective discharge control channel form (which is a topic that data from this study do not directly address), then an under design of effective discharge could cause subsequent bed and bank instabilities as the channel adjusts to a larger effective discharge to efficiently convey sediment delivered from upstream reaches [e.g., *Mackin*, 1948; *Leopold et al.*, 1964; *Mao and Surian*, 2010].

The increase in transport rates with the use of the lower $\tau^*_{c,50}$ value caused more significant changes in the predicted bedload budget than the effective discharges. The half-load discharges changed at most sites (Figure 4.7e). The higher transport stages predicted by the

lower $\tau^*_{c,50}$ decreased the volumetric differences in models II and III, causing both models to predict the same half-load discharge for each site. The lower $\tau^*_{c,50}$ value predicted larger half-load discharges at location D and smaller half-load discharges at locations E and F, G (model II and III) and B (model III only). Despite the shift to having more sediment transported over the lower discharges under the lower $\tau^*_{c,50}$ conditions, the majority of sediment was still contributed by flows exceeding the effective discharges at all sites (Figures 4.7c and 4.7). The significant differences in the sediment volumes and volumetric contributions over the discharges illustrates that consideration of local channel morphology is needed when applying $\tau^*_{c,50}$ to constrain bedload budgets in mountain streams.

4.4.4 MODEL LIMITATIONS

Limitations of model I include clast size and constant, linear scaling of bedload with excess discharge volumes. Given that model I is based on a previous passive tracer study [Ch. 2, Ch. 3], the relations used in model I are explicitly from clasts that approximate the mean D_{50} of the channel rather than significantly finer or coarser clasts. With the recent advent of smaller RFID tags (now as small as 8 mm), future magnitude-frequency models using tracer displacements can further examine whether the linear scaling reflected in Equations 4.2 and 4.3 approximates the displacement trends over a range of bedload sizes. Additionally, future studies with tracer surveys that are more frequent (specifically after longer, smaller floods and after shorter, larger floods that have similar effective runoff volumes) could also examine if the linear scaling of mean displacements with effective runoff varies with the discharge magnitude.

The three models evaluated cannot explicitly account for changes in bedload supply over time, which is often the case for steep channels [e.g., *Moog and Whiting*, 1998; *Yager et al.*, 2012b]. Whether the tracer clasts that model I was derived represented supply limitations observed in mountain streams cannot be determined with this dataset. However, the overall magnitude-frequency results are similar to the other models, whose approximation to mountain

streams is better constrained. By permitting bedload transport at low transport stages in model II, more transport was permitted in model II than model III. This difference reflects model II approximating a scenario where bedload was less supply limited than model III, particularly at the lower discharges (Figures 4.5c,d,e,f). For model II, the larger bedload supply at lower discharges caused bedload discharges to increase at a slower rate with water discharge than in model III (e.g., comparison of b_1 values in Figure 4.6 and Table 4.3).

Conversely, the delay in transport for model III caused model III bedload discharge-water discharge relation to have steeper scaling relations over the lower discharges and generally less steep relations over the higher discharges (e.g., b_1 versus b_2 in Figure 4.6 and Table 4.3). These trends in the b_1 and b_2 scaling for model III better represent the partial transport scenario of coarse alluvial streams, where the coarser bedload clasts tend to remain immobile over low discharges and enable the bed to relatively quickly develop some degree of surface armoring [e.g., *Carling*, 1988]. This armoring causes sediment supply to be more limited at lower flows when the armoring decreases as coarser clasts are entrained by higher discharges. Additionally, the relatively low values of b_2 values over the larger discharges in model III compared to those extrapolated by *Bunte et al.* [2014] (particularly those on the order of 10 and 20) suggests that the higher b_1-values extrapolated to larger discharges by *Bunte et al.* [2014] represented supply limited scenarios that were too high for those larger discharges that moved coarser clasts.

While the $\tau^*_{c,50}$ values in model II and III were adjusted spatially according to local bed slopes (discussed in Section 4.4.3.2), another limitation of the transport formulas was that the *b* value in Equation 4.14 remained spatially constant. The *b* value of -0.905 was used because it was similar to the value found at location A with the passive tracers and stationary antennas [Ch. 3]. Constraints at the other sites were unavailable but may have varied from the Parker [1990a] value. For example, work in a significantly steeper channel with larger, immobile boulders (S=0.098 m/m) has suggested that *b* values could be as high as -0.16 [*Yager et al.*, 2012a]. However, the sites examined in this study were less steep and had generally comparable grain size distributions, so it is expected that the *b*-value approximation of -0.905 was fairly

reasonable. If the *b* value at these sites was larger than -0.905, then the bedload predictions from models II and III represented a maximum estimate because a value closer to 0 would indicate that transport exhibited more size selectivity. Future work is needed to evaluate the trends in effective discharges and bedload budgets over time for mountain channels with slopes steeper than 0.05 m/m, larger immobile structures and more size selective, field constrained *b* values.

4.4.5 METHOD EXPANSION

The integration of the displacement and entrainment datasets from Reynolds Creek tracer with numerical flow modeling and empirical transport functions represents a unique approach to estimate the bedload budget of a mountain watershed. The use of displacements from passive tracers and numerical flow modeling from HEC-RAS permitted bedload transport to be evaluated over a range of discharges and shear stress conditions. The tracer displacement and flow modeling methods provide constraints on bedload transport that are often unavailable, because bedload measurements in mountain streams rarely covering discharges that exceed two times that of bankfull discharge [e.g., *Whiting et al.*, 1999; *Emmett and Wolman*, 2001; *Barry et al.*, 2008]. This new use of HEC-RAS modeled shear stresses showed that bedload discharge-water discharge scaling measured at low discharges [e.g., *Bunte et al.*, 2014] could be too steep for extrapolation to higher discharges (Section 4.4.1). The significance of this finding is that the methods applied in this study demonstrate how conflicting conclusions from magnitude-frequency analyses in mountain streams can be affected by extrapolated bedload measurements (e.g., Table 4.1).

4.5 Conclusions

New analyses of effective discharge and relative bedload volumes were performed in a mountain stream using tracer displacements and flow modeling with empirical transport formulas that were revised based on local bed slopes (up to 0.042 m/m). All the bedload models evaluated predicted that effective discharges correspond to moderate, high frequency flows

rather than larger, rarer events as previously concluded [*Bunte et al.*, 2014]. Models also predicted that the majority of bedload transported was contributed by discharges exceeding the identified effective discharges, which indicates the significance of a broad range of discharges rather than the single discharge to total bedload transport of mountain streams. The demonstrated sensitivity in the scaling of bedload discharge over lower water discharges versus higher discharges highlights the need for careful consideration of scaling and extrapolation methods used in magnitude-frequency analyses, landscape evolution and river and reservoir management that estimate bedload budgets [e.g., *Howard et al.*, 1994; *Bunte et al.*, 2014; *Ziegler et al.*, 2014].

Tables

Table 4.1: Summary of magnitude-frequency analyses from previously reported coarse alluvial studies and presented study

Summary of studies using discharge and bedload relations to compare effective discharges (Q_e), bankfull discharges (Q_{bf}), and half-load discharges ($Q_{0.5}$). For the last two columns, the majority of the bedload was contributed by discharges larger than the effective or bankfull discharge when $Q_e < Q_{0.5}$ or $Q_{bf} < Q_{0.5}$ was found.

Study	**Number of sites**	***S* (m/m)**	**drainage area (km^2)**	**D_{50} (mm)**	**Flow regime**	**Bedload transport**	**Q_e magnitude-frequency conclusions**	***RI of* Q_e**	**Q_e vs. Q_{bf}**	**Q_e vs. $Q_{0.5}$**	**Q_{bf} vs. $Q_{0.5}$**
[*Carling*, 1988]	2	0.01 and 0.04	11 and 2	20 and 50	Binned frequency of peak discharges for over 6 years	Power scaling based on local bedload rating curves from on 7.6 cm Helley Smith samples	moderate magnitude-high frequency	0.9 yr for S=0.01; NR for S=0.04	$Q_e \sim Q_{bf}$; NR for S=0.04	NR	NR
[*Andrews and Nankervis*, 1995]	17	0.001 to 0.26*	3- 3700	24-91	Binned mean daily discharges	Parker [1982] formula, with entrainment thresholds held constant for most sites ($\tau^*_{c,50}$ assumed 0.038)	moderate magnitude-high frequency	NR	Average: $Q_e \sim Q_{bf}$	$Q_e < Q_{0.5}$	$Q_{bf} < Q_{0.5}$
[*Whiting et al.*, 1999]	23	0.004-0.075	1.3-381	4-207	Scaled ungauged streams to regional relations	Power scaling based on local bedload rating curves from on 7.6 cm Helley Smith samples	moderate magnitude-high frequency	1-2.8	$Q_e < Q_{bf}$	NR	$Q_{bf} > Q_{0.5}$
[*Emmett and Wolman*, 2001]	5	0.005-0.019	55-4950	60-173	Binned mean discharges	Power scaling based on local bedload rating curves from on 7.6 cm Helley Smith samples	moderate magnitude-high frequency	1.6	$Q_e \sim Q_{bf}$	$Q_e \sim Q_{0.5}$	$Q_{bf} \sim Q_{0.5}$

Table 4.1 (continued): Summary of magnitude-frequency analyses from previously reported coarse alluvial studies and presented study

[*Torizzo and Pitlick*, 2004]	12	0.004-0.043	31-231	23-80	Scaled to ungauged streams based on regional flow frequency distributions	Parker [1982] formula, with entrainment thresholds held constant for most sites ($\tau^*_{c,50}$ assumed 0.033)	moderate magnitude-high frequency	NR	Q_e~Q_{bf}	Q_e>$Q_{0.5}$	Q_{bf}>$Q_{0.5}$
[*Lenzi et al.*, 2006b]	1	0.13-0.17	5	90	Fit log-normal frequency distribution to 5-min discharge data	I) Fit power scaling relation between measured bedload rates II) Averaged sediment rates	moderate magnitude-high frequency	NR	Q_e~Q_{bf}	NR	NR
[*Bunte et al.*, 2014]	41	0.007-0.193	4-239	NR	Fit two-part power law, flow frequency distributions to mean daily flows	Unmeasured at sites, assumed power scaling relations based on each site's watershed and channel characteristics	High magnitude-low frequency	NR	Q_e>Q_{bf}	NR	NR
[*Sholtes et al.*, 2014]	NA (theoretical investigation)	NA	NA	NA	Explored several two-parameter lognormal distributions	Several power scaling relations. Evaluated one sediment size per analysis ($\tau^*_{c,50}$ assumed 0.047)	NA	NA	NA	NA	NA
Presented study	7	0.01-0.04	55	51-90	Fit two-part power law, flow frequency distributions to mean daily discharges over 48 years	I) Field-based bedload displacement-hydrologic forcing relations II) Parker [1990a] formula, revised with field-based transport thresholds	moderate magnitude-high frequency	1.2-3.5	Q_e~Q_{bf}	Q_e<$Q_{0.5}$	Q_{bf}<$Q_{0.5}$

S: Slope; D_{50}: Median grain size; $\tau^*_{c,50}$=critical Shields stress for entrainment of D_{50} clasts; *: Only water surface slopes reported.

Table 4.2: Summary of predicted effective discharges (Q_e) and half loads ($Q_{0.5}$) from models I, II and III

Model I) Displacement-effective runoff relations (Section 4.3.1)

Q_t (m^3s^{-1})	Q_e (m^3s^{-1})	*CFT*	*RI* (yr)	$Q_{0.5}$ (m^3s^{-1})	*RI* (yr)
1.4	2.4	0.314	1.44	2.9	1.54
2	2.6	0.175	1.48	3.6	2.43

Models II and III) Empirical transport formulas (Section 4.3.2)

			Model II) Transport permitted at low stage					**Model III) Transport prevented at low stage**				
			Q_e			$Q_{0.5}$		Q_e			$Q_{0.5}$	
Site	***S*** **(m/m)**	D_{50} **(mm)**	(m^3s^{-1})	*CFT*	*RI* (yr)	(m^3s^{-1})	*RI* (yr)	(m^3s^{-1})	*CFT*	*RI* (yr)	(m^3s^{-1})	*RI* (yr)
A	0.018	61	1.1	0.166	1.16	3.4	2.12	1.2	0.146	1.16	6.0	4.79
B	0.042	90	2.4	0.363	1.44	3.5	2.36	2.4	0.171	1.44	6.1	4.89
C	0.016	75	2.4	0.441	1.44	2.7	1.51	2.4	0.396	1.44	3	1.56
D	0.014	68	2.4	0.479	1.44	2.5	1.46	2.4	0.305	1.44	3.3	2.07
E	0.010	51	3.4	0.205	2.12	5.5	4.30	3.4	0.204	2.12	5.5	4.30
F	0.013	55	5.5	0.312	4.30	7.3	9.69	5.5	0.300	4.30	7.4	10.44
G	0.012	71	2.5	0.206	1.46	5.1	3.72	2.5	0.186	1.46	5.2	3.80

Notation) Q_t: Threshold discharge for Equations 4.2 and 4.3; Q_e: Effective discharge; $Q_{0.5}$: Half-load discharge; RI: Recurrence interval; *S*: local bed slope; *CFT*: Cumulative fraction transported for a given discharge of interest

Table 4.3: Summary of power-scaling exponents for the bedload discharge-water discharge relations

Table lists the power-scaling exponents for the various models over discharges up to 1.5 times bankfull (b_1) and exceeding 1.5 times bankfull (b_2). The 95% confidence bounds around the exponents are indicated by the symbol ±. The regression analyses was performed in Matlab and the corresponding R^2 are presented. All correlation *p*-values are less than 0.05, which is indicative of the correlation between the observations and the regression fit being statistically significant at the 95% confidence level. Figure 4.6 also shows the exponents.

	Model II: 0.5 m^3s^{-1}<*Q*<3.8 m^3s^{-1}			**Model II: *Q*>3.8 m^3s^{-1}**		
Location	b_1	±	R^2	b_2	±	R^2
A	1.460	0.130	0.9703	2.937	0.014	0.9997
B	1.462	0.013	0.9997	3.566	0.040	0.9987
C	1.188	0.254	0.8816	2.452	0.024	0.9988
D	1.335	0.007	0.9999	3.266	0.057	0.9967
E	2.988	0.502	0.9404	2.606	0.024	0.9989
F	1.982	0.876	0.7124	3.044	0.033	0.9986
G	1.666	0.528	0.8117	2.875	0.018	0.9995
	Model III: 0.5 m^3s^{-1}<*Q*<3.8 m^3s^{-1}			**Model III: *Q*>3.8 m^3s^{-1}**		
Location	b_1	±	R^2	b_2	±	R^2
A	2.445	0.380	0.893	2.937	0.014	0.9997
B	6.779	3.154	0.4013	3.566	0.040	0.9987
C	2.097	0.160	0.9797	2.452	0.024	0.9988
D	5.939	2.786	0.2982	3.266	0.057	0.9967
E	6.727	0.933	0.9522	2.606	0.024	0.9989
F	6.952	0.391	0.9923	3.044	0.033	0.9986
G	3.551	0.193	0.9920	2.875	0.018	0.9995

Figures

Figure 4.1: Study area

(a) Site map of the Reynolds Creek study area. The triangles indicate Locations A through G. The stationary antenna reach (location A) was just upstream of the Tollgate discharge gauge (USDA-ARS gauge 116b), and has a drainage area of approximately 55 km^2.
(b) Riffle reach at location A.
(c) Plane-bed reach with bedrock sidewall on river left, approximately 100 m downstream of location B.
(d) Reach just upstream location E having unorganized boulders and narrow channel widths due to banks of dense willows and canyon setting. Image is representative of upstream and downstream sections of Location F as well.
(e) Deposit at the pool upstream of USDA-ARS Tollgate station. Circled person to the right of center wall in background provides scale.

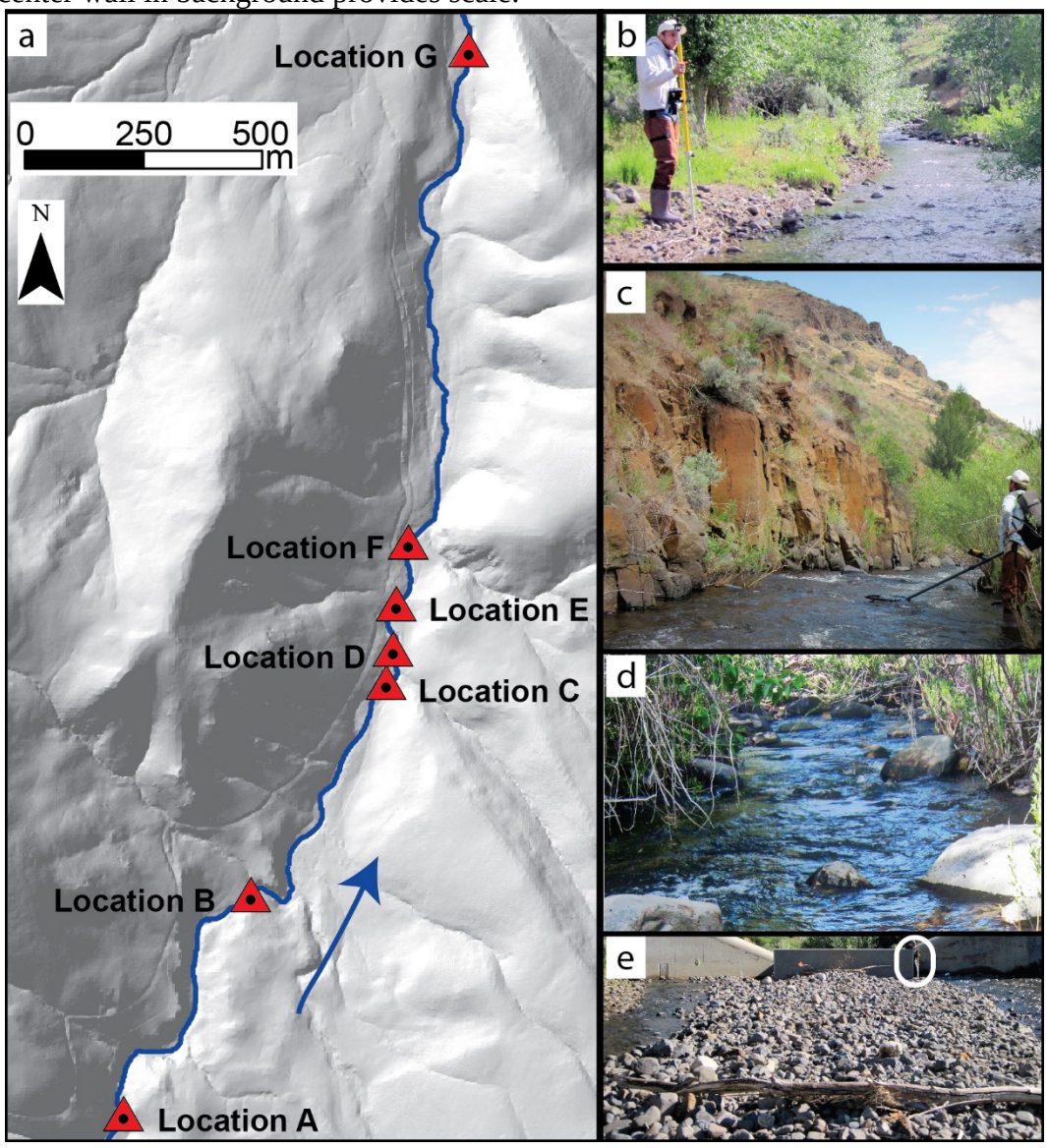

Figure 4.2: Flow frequency distribution

(a) Probability density functions (*PDF*) of the discharges (*Q*) calculated at the Tollgate station (USDA-ARS gauge 116b, data from *Northwest Watershed Research Center* [2015]). *PDF*s shown correspond to the 15-minute discharge records over the water years from 1994 through 2014 (grey circles), mean daily discharges based on 15-minute records from 1994 through 2014 (blue triangles), and the mean daily records from 1966 through 2014 records (magenta squares). Due to the consistency among the *PDFs*, the flow frequency curve is fit to the mean daily records from 1966 to 2014, similar to methods performed in other mountain streams in the western United States [e.g., *Segura and Pitlick*, 2010; *Bunte et al.*, 2014].
(b) Flood frequency plot based on the maximum mean daily discharges recorded each year at the USDA-ARS Tollgate gauge from 1966 through 2014.

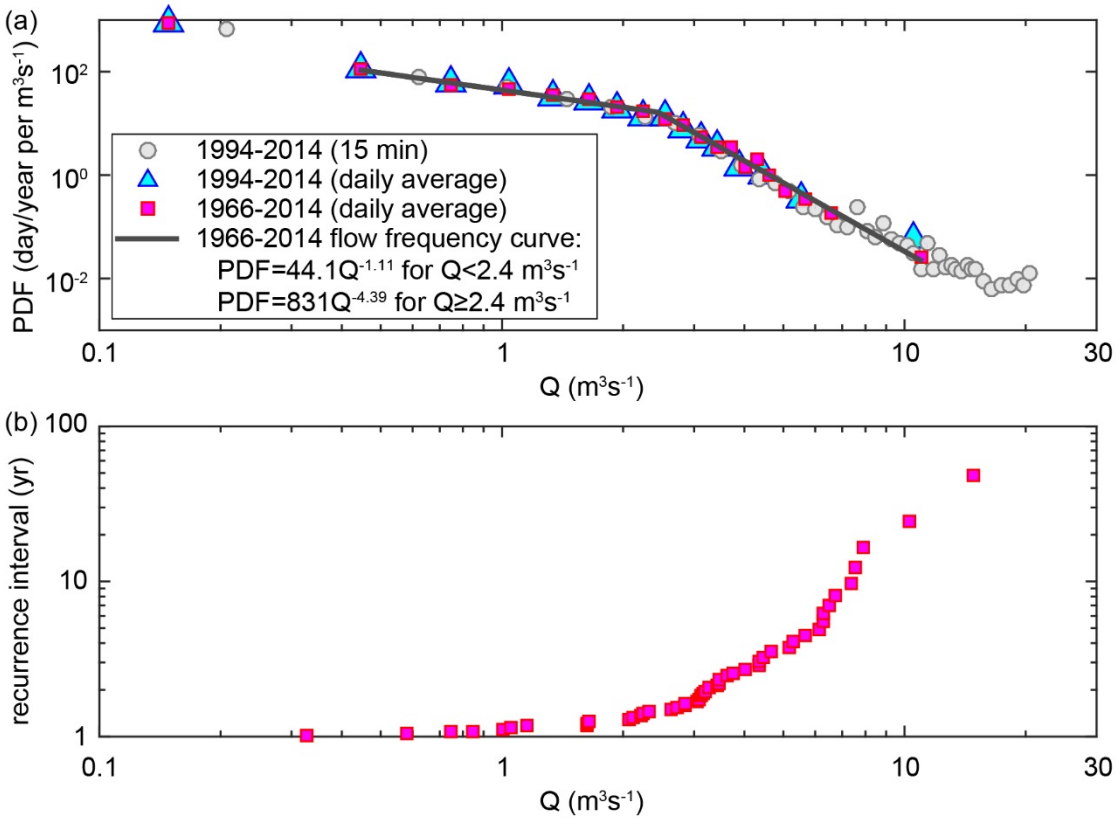

Figure 4.3: Site characteristics at locations A through G

(a) Local bed slope averaged over moving 10 m windows shown in light grey. Locations A through G are identified by the symbols corresponding to the legend above.
(b) Grain size distribution at sites of interest. Clasts were aggregated at bins of 2 to 7 mm, >7 to 15 mm, >15mm to 25 mm, and so on at increments of 10 mm until 765 mm. Inset: D_{16}, D_{50} and D_{84} lines correspond to the size in which 16, 50 and 84% of the coarse surface grains were finer.
(c) HEC-RAS calculated shear stress (τ) versus water discharge (Q). Shear stress scaling for locations were as follows: A was $\tau \sim Q^{0.33}$; B was $\tau \sim Q^{0.48}$; C was $\tau \sim Q^{0.28}$; D was $\tau \sim Q^{0.40}$; E was $\tau \sim Q^{0.62}$; F was $\tau \sim Q^{0.63}$ and G was $\tau \sim Q^{0.36}$.
(d) The transport stages ($\tau^*_{50}/\tau^*_{c,50}$; Equation 4.9) versus water discharge.

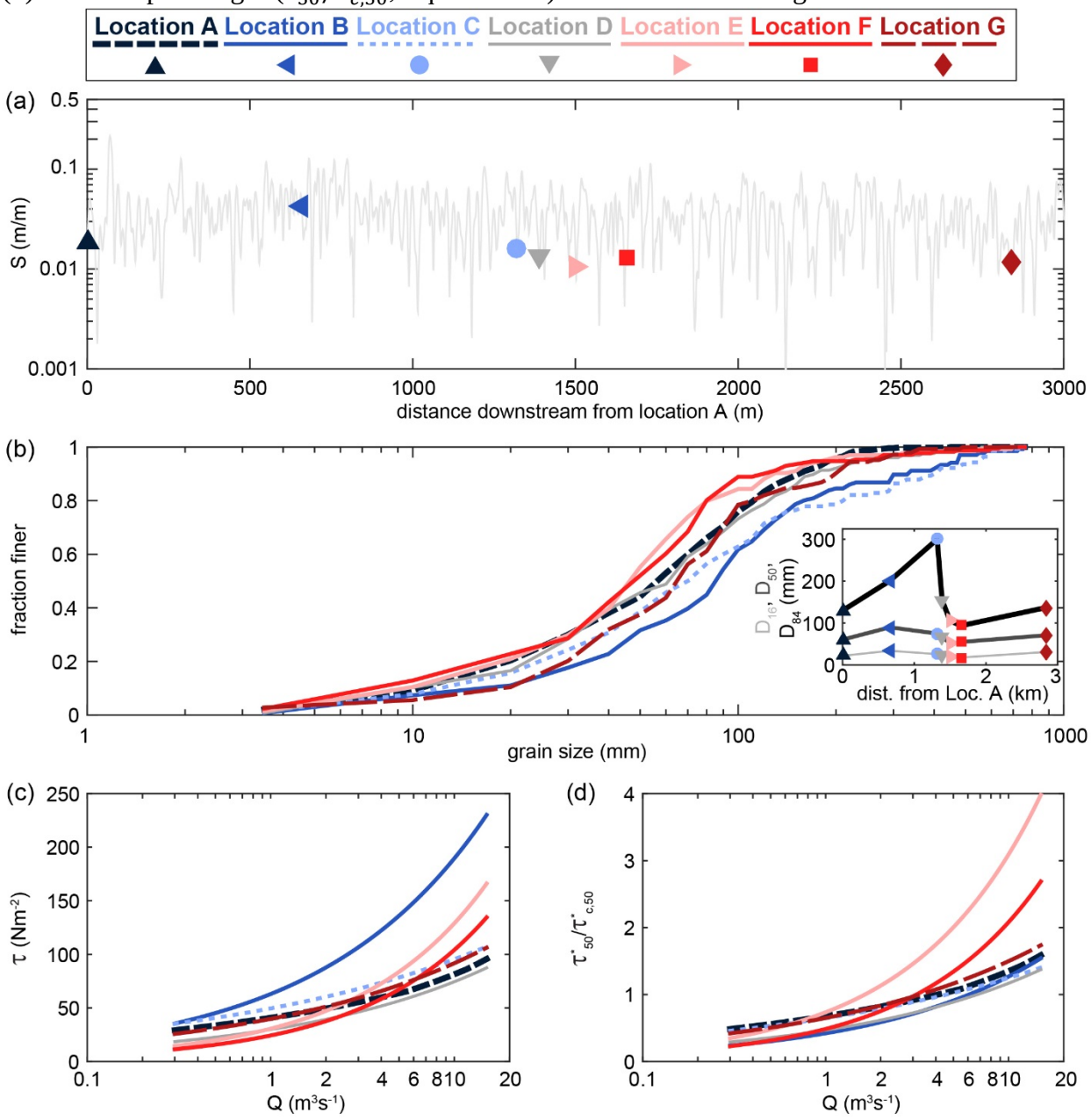

Figure 4.4: Effective discharges and half load discharges predicted by model I

(a) Fraction of mean displacement to total mean displacement ($<X>/<X>_{total}$) with respect to water discharge (Q) using the tracer displacement relations that had a transport threshold (Q_t) of 1.4 m^3s^{-1} (Equation 4.2) and 2 m^3s^{-1} (Equation 4.3). Effective discharges corresponded to the peak fractions.
(b) Cumulative fractions of total displacements from subplot a with respect to discharge. The effective discharges (Q_e) and half-load discharges ($Q_{0.5}$) are also indicated.

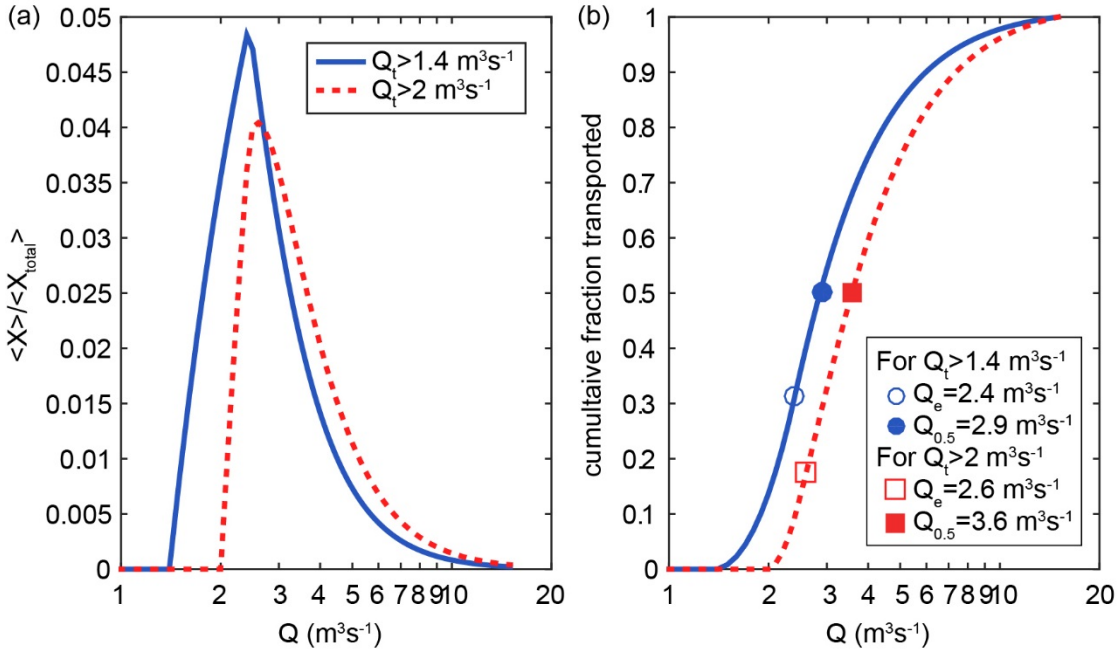

Figure 4.5: Bedload transport rates, fraction transported, effective discharge and half-load discharges predicted by models II and III

(a, b) Bedload rates ($Q_{B,total,Qm}$) versus water discharge (Q) for Model II and Model III (Equations 4.15 and 4.16).
(c, d) Resulting bedload volumes (V_{B,Q_m}) versus water discharge (Q) predicted over 1966-2014. Results are the product of bedload rates and flow frequency distribution (Equation 4.21).
(e,f) The fraction of sediment volume to total bedload volume ($V_B/V_{B,total}$) with respect to discharge. Effective discharges corresponded to the peak fractions.
(g,h) Cumulative fraction of transported bedload versus water discharge. The effective discharges (from subplots c and d) are indicated with open symbols, and half-load discharges are indicated with filled symbols (due to the overlap, see also Table 4.2).

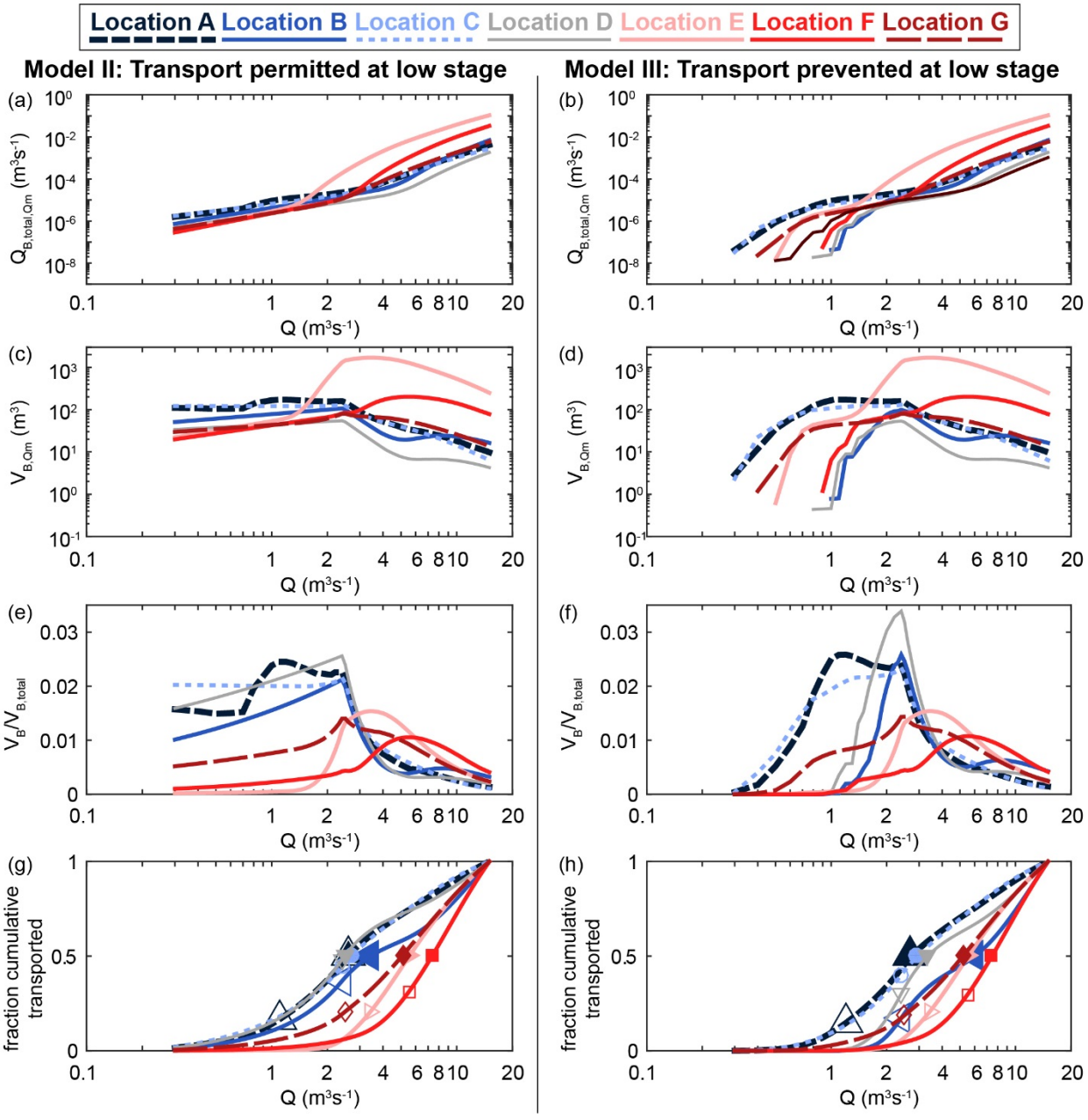

Figure 4.6: Power-scaling exponents for bedload discharge-water discharge relations from Model II, Model III, and the spatially constant shear stress

(a,b) Open symbols correspond to the b_1 exponents calculated from the bedload discharge-water discharge (Q_B-Q) power scaling relations for discharges between 0.5 m^3s^{-1} and 3.8 m^3s^{-1} (i.e., up to 1.5 times that of bankfull discharge). Filled symbols correspond to the b_2 exponents calculated from the bedload discharge-water discharge power scaling relations for discharges exceeding 1.5 times bankfull.

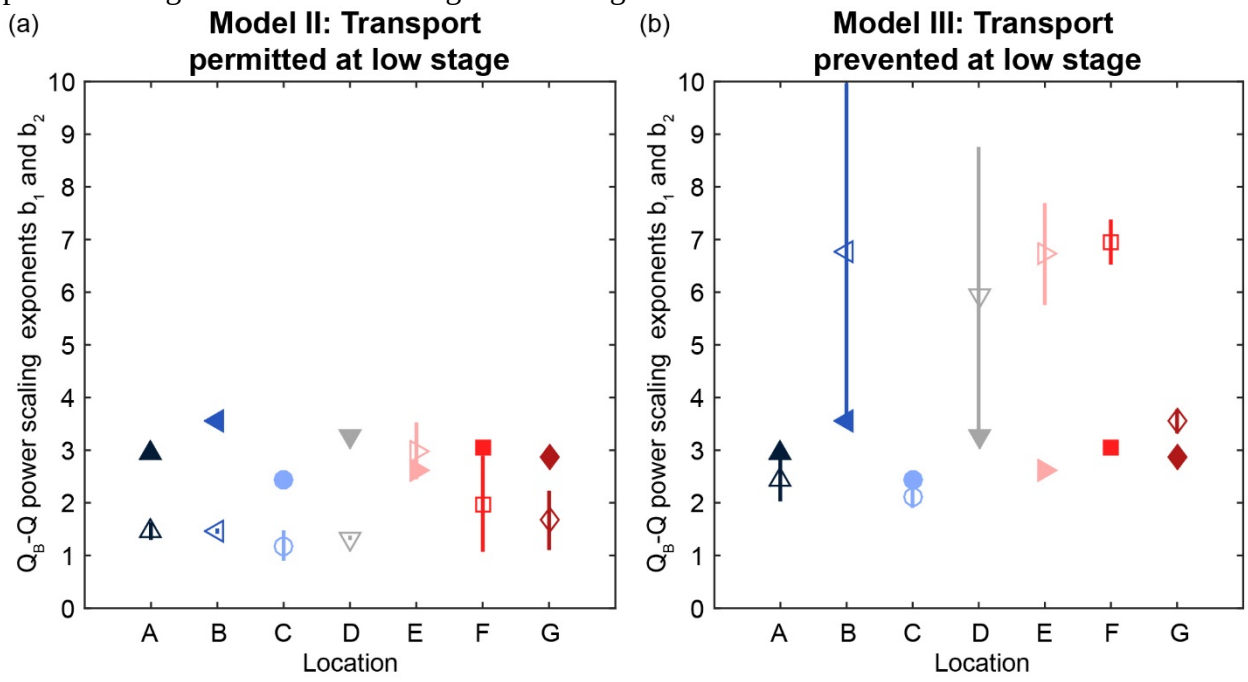

Figure 4.7: Comparison of bedload transport rates, fraction transported, effective discharges and half-load discharges predicted assuming a lower, spatially constant entrainment threshold versus slope-dependent thresholds

(a) Bedload discharge ($Q_{B,total,Qm}$) predicted by assuming a constant critical Shields number for the median sized clasts ($\tau^*_{c,50}$) of 0.039 at all sites.
(b) Total bedload volumes for a given discharge ($V_{B,Qm}$) using $\tau^*_{c,50}$=0.039 versus the volumes from slope-dependent $\tau^*_{c,50}$. Grey line represents 1:1 line.
(c) The fraction of sediment volume to total bedload volume ($V_B/V_{B,total}$) with respect to discharge. Effective discharges corresponds to the peak fractions.
(d) Effective discharge (Q_e) found for $\tau^*_{c,50}$=0.039 predictions versus that found with the slope-dependent $\tau^*_{c,50}$ predictions. Open symbols represent model II; closed symbols represent model III. Grey line represents 1:1 line.
(e) Half-load discharges ($Q_{0.5}$) found for $\tau^*_{c,50}$=0.039 predictions versus that found with the slope-dependent $\tau^*_{c,50}$ predictions. Open symbols represent model II; closed symbols represent model III. Grey line represents 1:1 line.

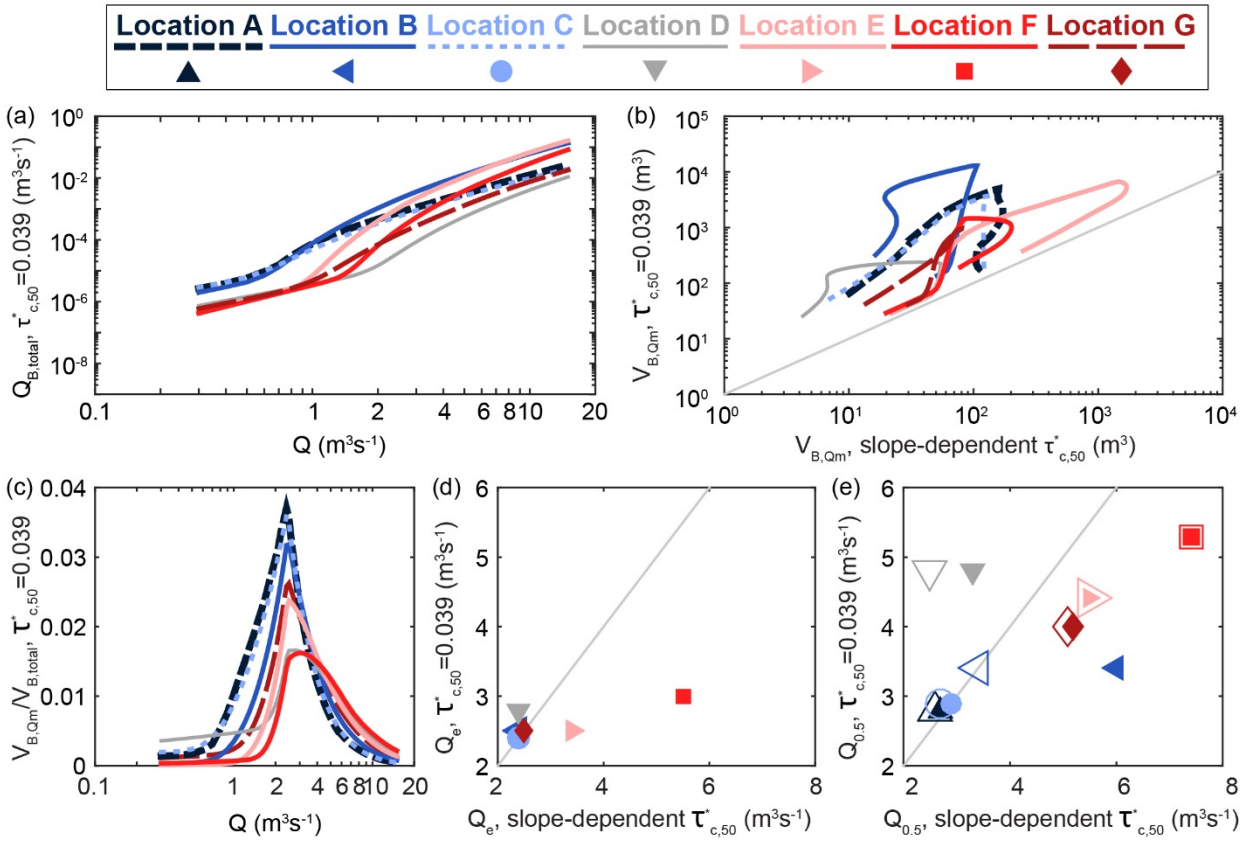

CHAPTER 5: SUMMARY

The work presented in this dissertation aimed to address gaps in understanding the displacement and entrainment behavior of bedload clasts in mountain streams. The rare, field-based datasets from active and passive tracers and numerical flow modeling enabled the characterization of morphologic and stochastic hydrologic influences that drive bedload dispersion. Key findings in the presented studies include the following:

- Probabilities of transport for coarse bedload particles increase with increases in discharge [Ch. 2]
- Step lengths and cumulative displacements also increase with increases in hydrologic forcing [Ch. 2]
- Heavy-tailed rest time distributions suggest superdiffusive dispersion in mountain streams [Ch. 2]
- Bedload exhibits equal entrainment mobility in plan-bedded coarse alluvial reaches [Ch. 3]
- Thresholds of motion are more appropriately represented by a distribution rather than a single, spatially constant value [Ch. 3]
- Thresholds of motion increase with increases in local bed slope [Ch. 3]
- Deposition can frequently occur at flow strengths lower than re-entrainment [Ch. 3]
- Preferential bedload deposition can occur at slightly wider reaches in mountain streams [Ch. 3]

- Effective discharges in mountain streams correspond to moderate, high frequency flows [Ch. 4]
- A broad range of discharges rather than a single effective discharge contributes the most significantly to total bedload transport [Ch. 4]
- Sensitivity in the scaling of bedload discharge-water discharge relations can cause significant extrapolation errors for flow conditions outside those measured [Ch. 4]

The presented findings reveal several new distinctions applicable to conceptual and prediction models of bedload transport. The indication of superdiffusive dispersion signifies that the hypothesis of subdiffusive transport persisting over timescales longer than tens of seconds, i.e. over a "global range", does not apply in coarse alluvial channels [*Nikora et al.*, 2002]. The distributions of thresholds of motion suggest that river management projects and fluvial prediction studies with objectives of estimating bedload budgets and bed stability would better predict the range of possible project outcomes by evaluating transport using a range of thresholds [e.g., *Andrews and Nankervis*, 1995; *Torizzo and Pitlick*, 2004; *USDA-NRCS*, 2007]. These distributions also suggest that larger uncertainties are likely associated with paleohydrologic studies that have constrained the magnitudes of peak flood events based on assuming a single critical Shields numbers for the largest grains found in deposits [e.g., *Baker*, 1974; *Sugai*, 1993; *Grossman*, 2001]. Additionally, observing almost half of deposition occurrences corresponding to flow strengths that were lower than those of re-entrainment showed that the classic theory proposed by *Hjulström* [1935] does not fully describe transport behavior in natural streams. The observed sensitivity in the scaling of bedload discharge-water discharge relations highlights the need for careful consideration in the choice of

scaling and extrapolation methods used in magnitude-frequency analyses, landscape evolution and river and reservoir management that estimate bedload budgets [e.g., *Howard et al.*, 1994; *Bunte et al.*, 2014; *Ziegler et al.*, 2014]. Finally, the demonstrated influence of hydrologic forcing and channel morphology on bedload transport highlight the need for their incorporation into dispersion models to better approximate natural settings [e.g., *Ganti et al.*, 2010; *Hill et al.*, 2010; *Bradley and Tucker*, 2012].

Future work remains warranted to determine how hydrologic and morphologic parameters can be included in bedload models to adequately reflect a range of conditions. For example, direct measurements of bedload transport are needed throughout low to high discharges in step-pool and boulder-bedded reaches to quantify the extent to which transport in these steeper settings deviate from the near equal entrainment mobility observed in plane-bedded reaches. Such measurements in both plane-bedded and steeper reaches should also include a broad grain size distribution that represents the range of fine to coarse bedload clasts. Field constraints are also needed to estimate the degree that particle mobility and bed stability varies after floods that have significantly differing peak discharges. Despite progress made by this study and others like it, considerable technical challenges remain in being able to relate such bedload measurements to during-flood variations in the structure of channel beds over time.

APPENDIX: RFID AND ACCELEROMETER TECHNOLOGIES

Below provides additional details to the RFID and accelerometer technologies described in Chapter 2.

Table A1: Design considerations related to the RFID and accelerometer technologies applied to Reynolds Creek

Technological limitation	Design approach & considerations
RFID tags	
• Smaller RFID tags have shorter read ranges.	• Used largest RFID tag possible for each tracer clast.
• Likelihood of a RFID tag being read depends on its orientation relative to an antenna. Tags are often not read at all when oriented parallel to an antenna plane.	• Embedded tracers with tags parallel to the clasts' intermediate axes. Presumably it is more likely that a clast rotates parallel to its longest axis as it passes an antenna, so aligning tags parallel to the shortest or intermediate axes could be helpful. However, choosing the shortest increases risk of rock fracturing.
• Antennas cannot read RFIDs that are immediately adjacent to metal.	• Having no metal in the active tracers was not feasible because of accelerometer batteries and lead weights. However, separating tags ~1 cm away from these components was sufficient for antenna readings.
Mobile antennas	
• If more than one particle is within the antenna read range, signals interfere and typically no tags are read.	• If one finds an area with a large number of particles, change to a smaller mobile antenna. However, a smaller antenna may not be sufficient if tracers are very closely spaced as data logger corruption due to radio interference may occur. • By decreasing the read range in high tracer deposition areas, one can decrease the likelihood that more than one tracer is read at one time. However, decreasing antenna read distance also decreases vertical read depth into the bed.

Table A1 (continued): Design considerations related to the RFID and accelerometer technologies applied to Reynolds Creek

Technological limitation	Design approach & considerations
Stationary antennas	
• Antenna read distances decrease when immediately adjacent to metal.	• Used as little metal as possible when securing antennas on streambed. • Used largest RFID tag possible for each clast because, when some metal was present, antennas read larger tags better than smaller ones.
• If more than one particle is within an antenna read range, typically no tags are read.	• Staggered tracer deployment locations so that dispersion with distance decreases likelihood of being read within a given antenna scan. • Configured antennas widths to be fairly narrow (0.5 m) and tuned their read distances (0.25 m) to decrease the likelihood of multiple tagged rocks passing through an antenna field at a given time. • Placed several antennas in same reach to minimize tracers passing through reach unread.
• Antennas must be individually tuned for each shape to optimize tag reading. Retuning may be required if antenna shape changes.	• After large transport events, checked antenna read ranges and made adjustments as needed. If logistically feasible, strongly recommend to reassess the shape of antennas after large floods.
• If a reader is powered but not connected to an antenna, the reader can overheat causing permanent damage to the circuit board.	• Staked antennas to bed to prevent antennas from being entirely eroded away from the site while the reader was still powered on.
• If data logger scanning rate is too slow, tracers moving very fast may pass over an antenna without being read.	• Set antenna read rate settings to ~5-10 scans per second. Monitored power consumption and read range when setting scan rate. Increasing number of scans per second could increase probability of recording a tracer within antenna read distance; however, increasing scan rates can also increase the required antenna power.
• Single antenna data loggers can be located up to 130 m from its antenna. Multiple antenna data loggers (MUX) perform best when located within 20 m from their antennas (Leach, pers. comm.).	• Positioned the solar panels, the MUX readers, batteries and power regulators 50 m from the antennas to keep the equipment above the floodplain. While this slightly decreased antenna performance, data loggers were required to stay dry.
• Between the fall installation and the spring events, the data loggers experienced non-systematic time drifts of ±5 min and thus prevented calculation of particle velocity.	• Recommend resetting data logger time every couple of weeks when transport is expected.
Active tracers	
• Accelerometer memory limited to 64kb.	• To collect data over several months, before embedding in tracer, set device sampling times to 10-minutes, and delayed sample start until date of expected deployment

Table A2: Procedure for the preparation of artificial tracers.

Using the procedure outlined below, one batch has approximately 30 min of workability. This short duration required mixing several batches a day to fill all accelerometer and RFID molds. The coarse aggregate in the concrete mixture consisted of pea gravel from hardware stores, but density could be increased by using denser aggregate such as crushed basalt or garnet sand. None of the recovered accelerometer particles cracked during transport, suggesting that these concrete casting methods produce sufficiently strong cobbles to withstand energetic transport. Mixture was developed by collaborating with students in the structural materials department at the University of Texas.

1. Mix cementitious material in a dry container.
    - White Portland Type 1 Cement: 1815 g (4 lbs)
    - Silica Fume: 140 g (0.3 lbs). Increases concrete and durability.
    - Powdered concrete pigment: 50 g (0.1 lbs)
2. Mix liquids in a separate container.
    - Water: 680 g (1.5 lbs). Maximum cement to water ratio should be less than 0.4 by weight to maintain high strength.
    - Sika 2100 ViscoCrete plasticizer: 9 ml. Plasticizer increased workability without additional water, allowing to transfer concrete into molds while keeping water-to-cement ratios low.
3. Mix aggregates in a separate container.
    - Coarse aggregate (pea pebbles): 4355 g (9.6 lbs)
    - Fine aggregate (sand): 2720 g (6 lbs)
4. Add liquids to cementitious material and mix.
5. Add aggregates to liquid/cementitious material and mix.
6. Pour concrete into the two-piece rubber molds. Fill the bottom halves; then, place the top mold onto the bottom. Finish filling mold from small hole in the top (Figure 4b).
7. Tag casts while concrete is still wet (Figure 4c). See Table 1 for tag orientation considerations.
8. After at least 12 hours, remove tracers from molds and submerge in water for a couple weeks to improve strength as concrete fully cures.

Figure A1: Shape diagram of local clasts and the deployed passive and active tracers

Shape measurements based on longest (a), intermediate (b) and shortest axes (c). Plot created with the Graham and Midgley [2000] program.

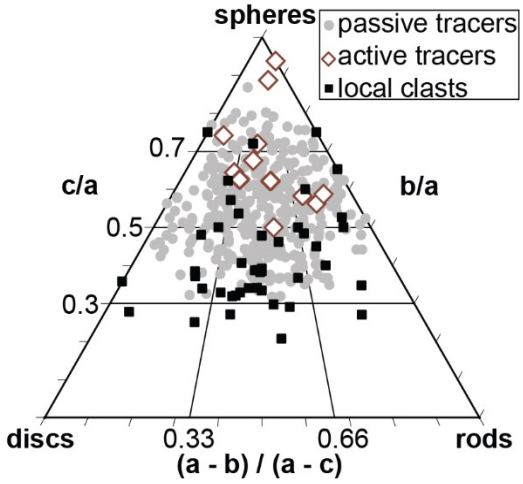

Figure A2: Shape Additional images of passive and active tracer production.

(a) 32 mm RFID tag, coarse gravel and protective silicon sleeve. (b) As part of the artificial clast production, filled the two part molds from the top with wet concrete. (c) RFID tags in silicon sleeves were inserted into wet concrete casts from the top molds. Tags were maneuvered to be perpendicular to the mold's intermediate axis (Table S1). (d) A recovered artificial passive tracer (red) on bed surface. (e) Hobo 3G accelerometer with 30 mm RFID disc. (f) Cobbles suspended in containers to produce two part rubber molds. (g) Top and bottom half of one rubber mold-set; cured active tracers is shown in bottom half. (h) An active tracer after extraction from a mold. (i) Example acceleration readings over an accelerometer's x, y and z axes at different static configurations. (j) An accelerometer tracer broken opened after recovery in Reynolds Creek.

REFERENCES

Allan, J. C., R. Hart, and J. V. Tranquili (2006), The use of Passive Integrated Transponder (PIT) tags to trace cobble transport in a mixed sand-and-gravel beach on the high-energy Oregon coast, USA, *Mar. Geol.*, *232*(1–2), 63–86, doi:10.1016/j.margeo.2006.07.005.

Andrews, E. D. (1980), Effective and bankfull discharges of streams in the Yampa River basin, Colorado and Wyoming, *J. Hydrol.*, *46*(3–4), 311–330, doi:10.1016/0022-1694(80)90084-0.

Andrews, E. D. (1983), Entrainment of gravel from naturally sorted riverbed material, *Geol. Soc. Am. Bull.*, *94*(10), 1225–1231, doi:10.1130/0016-7606(1983)94<1225:EOGFNS>2.0.CO;2.

Andrews, E. D., and D. C. Erman (1986), Persistence in the Size Distribution of Surficial Bed Material During an Extreme Snowmelt Flood, *Water Resour. Res.*, *22*(2), 191–197, doi:10.1029/WR022i002p00191.

Andrews, E. D., and J. Nankervis (1995), Effective Discharge and the Design of Channel Maintenance Flows for Gravel-Bed Rivers, in *Natural and Anthropogenic Influences in Fluvial Geomorphology*, pp. 151–164, AGU, Washington, D. C.

Ashiq, M., and J. Bathurst (1999), Comparison of Bed Load Sampler and Tracer Data on Initiation of Motion, *J. Hydraul. Eng.*, *125*(6), 661–664, doi:10.1061/(ASCE)0733-9429(1999)125:6(661).

Ashworth, P. J., and R. Ferguson (1989), Size-Selective Entrainment of Bed Load in Gravel Bed Streams, *Water Resour. Res.*, *25*(4), PP. 627–634, doi:198910.1029/WR025i004p00627.

ASTM Standard C127-07 (2007), *Standard Test Method for Density, Relative Density (Specific Gravity), and Absorption of Coarse Aggregate*, ASTM International, West Conshohocken, PA.

Baker, V. R. (1974), Paleohydraulic interpretation of Quaternary alluvium near Golden, Colorado, *Quat. Res.*, *4*(1), 94–112, doi:10.1016/0033-5894(74)90067-2.

Barry, J., J. M. Buffington, P. Goodwin, M. Asce, J. King, and W. Emmett (2008), Performance of bedload transport equations relative to geomorphic significance: Predicting effective discharge and its transport rate, *J. Hydraul. Eng.*, *143*(5), 601–615, doi:10.1061/ASCE0733-9429.

Barry, J. J., J. M. Buffington, and J. G. King (2004), A general power equation for predicting bed load transport rates in gravel bed rivers, *Water Resour. Res.*, *40*(10), W10401, doi:10.1029/2004WR003190.

Bathurst, J. (1987), Critical conditions for bed material movement in steep, boulder-bed streams, in *the Corvallis Symposium*, vol. 165, pp. 309–318, International Association of Hydrological Sciences, Corevallis, OR.

Bradley, D. N., and G. E. Tucker (2012), Measuring gravel transport and dispersion in a mountain river using passive radio tracers, *Earth Surf. Process. Landf.*, *37*(10), 1034–1045, doi:10.1002/esp.3223.

Brunner, G. (2010), *HEC-RAS River Analysis System User's Manual*, U.S. Army Corps of Engineers, Davis, CA.

Buffington, J. M., and D. R. Montgomery (1997), A systematic analysis of eight decades of incipient motion studies, with special reference to gravel-bedded rivers, *Water Resour. Res.*, *33*(8), PP. 1993–2029.

Bunte, K., S. R. Abt, J. P. Potyondy, and S. E. Ryan (2004), Measurement of Coarse Gravel and Cobble Transport Using Portable Bedload Traps, *J. Hydraul. Eng.*, *130*(9), 879–893, doi:10.1061/(ASCE)0733-9429(2004)130:9(879).

Bunte, K., S. R. Abt, K. W. Swingle, and D. A. Cenderelli (2014), Effective discharge in Rocky Mountain headwater streams, *J. Hydrol.*, *519, Part B*, 2136–2147, doi:10.1016/j.jhydrol.2014.09.080.

Carling, P. (1988), The concept of dominant discharge applied to two gravel-bed streams in relation to channel stability thresholds, *Earth Surf. Process. Landf.*, *13*(4), 355–367, doi:10.1002/esp.3290130407.

Chacho, E., W. Emmett, and R. L. Burrows (1994), Monitoring gravel movement using radio transmitters, *Hydraul. Eng.*, *2*, 785–789.

Chacho, E., R. L. Burrows, and W. Emmett (1996), Motion characteristics of coarse sediment in a gravel bed river, vol. Vol. 2, pp. 1–8, Las Vegas, NV.

Chin, A. (2003), The geomorphic significance of step–pools in mountain streams, *Geomorphology*, *55*(1–4), 125–137, doi:10.1016/S0169-555X(03)00136-3.

Chow, V. T. (1959), *Open-channel hydraulics*, McGraw-Hill.

Church, M., and M. A. Hassan (2002), Mobility of bed material in Harris Creek, *Water Resour. Res.*, *38*(11), 1237, doi:10.1029/2001WR000753.

Church, M., J. F. Wolcott, and W. K. Fletcher (1991), A Test of Equal Mobility in Fluvial Sediment Transport: Behavior of the Sand Fraction, *Water Resour. Res.*, *27*(11), 2941–2951, doi:10.1029/91WR01622.

Dietrich, W. E., and T. Dunne (1978), c, *Z. Für Geomorphol. Suppl.*, (29), 191–206.

Dodov, B., and E. Foufoula-Georgiou (2005), Fluvial processes and streamflow variability: Interplay in the scale-frequency continuum and implications for scaling, *Water Resour. Res.*, *41*(5), W05005, doi:10.1029/2004WR003408.

Doyle, M., D. Shields, K. Boyd, P. Skidmore, and D. Dominick (2007), Channel-Forming Discharge Selection in River Restoration Design, *J. Hydraul. Eng.*, *133*(7), 831–837, doi:10.1061/(ASCE)0733-9429(2007)133:7(831).

Drake, T. G., R. L. Shreve, W. E. Dietrich, P. J. Whiting, and L. B. Leopold (1988), Bedload transport of fine gravel observed by motion-picture photography, *J. Fluid Mech.*, *192*, 193–217, doi:10.1017/S0022112088001831.

Einstein, H. (1937), Bedload Transport as a Probability Problem, Mitteilung der Versuchsanstalt fuerWasserbau an der Eidgenössischen Technischen Hochschule, Zürich.

Einstein, H. (1950), The bed load function for sediment transport in open channel flows, *U. S. Dep. Agric. Tech. Bull.*, *1026*(September).

Emmett, W., R. L. Burrows, and E. Chacho, Jr. (1996), Coarse−particle transport in a gravel−bed river, *Int. J. Sediment Res.*, *11*(2), 8−21.

Emmett, W. W., and M. G. Wolman (2001), Effective discharge and gravel-bed rivers, *Earth Surf. Process. Landf.*, *26*(13), 1369–1380, doi:10.1002/esp.303.

Emmett, W. W., L. B. Leopold, and R. H. Myrick (1983), Some characteristics of fluvial processes in rivers, in *Proceedings of the Advanced Seminar on Sedimentation*, U.S. Geological Survey, Denver, CO.

Ergenzinger, P., and K.-H. Schmidt (Eds.) (1994), *Dynamics and Geomorphology of Mountain Rivers*, Springer Berlin Heidelberg, Berlin, Heidelberg.

Ferguson, R. I. (2005), Estimating critical stream power for bedload transport calculations in gravel-bed rivers, *Geomorphology*, *70*(1-2), 33–41, doi:10.1016/j.geomorph.2005.03.009.

Ferguson, R. I., and S. J. Wathen (1998), Tracer-pebble movement along a concave river profile: Virtual velocity in relation to grain size and shear stress, *Water Resour. Res.*, *34*(8), 2031–2038, doi:10.1029/98WR01283.

Ferguson, R. I., K. L. Prestegaard, and P. J. Ashworth (1989), Influence of sand on hydraulics and gravel transport in a braided gravel bed river, *Water Resour. Res.*, *25*(4), 635–643, doi:10.1029/WR025i004p00635.

Ferguson, R. I., D. J. Bloomer, T. B. Hoey, and A. Werritty (2002), Mobility of river tracer pebbles over different timescales, *Water Resour. Res.*, *38*(5), 3–1–3–8, doi:10.1029/2001WR000254.

Furbish, D. J., P. K. Haff, J. C. Roseberry, and M. W. Schmeeckle (2012), A probabilistic description of the bed load sediment flux: 1. Theory, *J. Geophys. Res.*, *117*(F3), F03031, doi:10.1029/2012JF002352.

Gaeuman, D. (2010), Mechanics of bedload rating curve shifts and bedload hysteresis in the Trinity River, California, Las Vegas, NV.

Ganti, V., M. M. Meerschaert, E. Foufoula-Georgiou, E. Viparelli, and G. Parker (2010), Normal and anomalous diffusion of gravel tracer particles in rivers, *J. Geophys. Res.*, *115*, F00A12, doi:10.1029/2008JF001222.

Gomez, B., and M. Church (1989), An assessment of bed load sediment transport formulae for gravel bed rivers, *Water Resour. Res.*, *25*(6), PP. 1161–1186, doi:198910.1029/WR025i006p01161.

Goode, J. R., and E. Wohl (2010), Substrate controls on the longitudinal profile of bedrock channels: Implications for reach-scale roughness, *J. Geophys. Res. Earth Surf.*, *115*(F3), n/a–n/a, doi:10.1029/2008JF001188.

Grant, G. E. (1997), Critical flow constrains flow hydraulics in mobile-bed streams: A new hypothesis, *Water Resour. Res.*, *33*(2), 349–358, doi:10.1029/96WR03134.

Grossman, M. (2001), Large floods and climatic change during the Holocene on the Ara River, Central Japan, *Geomorphology*, *2001*(1-2), 21–37, doi:10.1016/S0169-555X(01)00049-6.

Habersack, H. M. (2001), Radio-tracking gravel particles in a large braided river in New Zealand: a field test of the stochastic theory of bed load transport proposed by Einstein, *Hydrol. Process.*, *15*(3), 377–391, doi:10.1002/hyp.147.

Haschenburger, J. K., and M. Church (1998), Bed material transport estimated from the virtual velocity of sediment, *Earth Surf. Process. Landf.*, *23*(9), 791–808, doi:10.1002/(SICI)1096-9837(199809)23:9<791::AID-ESP888>3.0.CO;2-X.

Hassan, M. A., and M. Church (2000), Experiments on surface structure and partial sediment transport on a gravel bed, *Water Resour. Res.*, *36*(7), 1885–1895, doi:200010.1029/2000WR900055.

Hassan, M. A., and M. Church (2001), Sensitivity of bed load transport in Harris Creek: Seasonal and spatial variation over a cobble-gravel bar, *Water Resour. Res.*, *37*(3), 813–825, doi:10.1029/2000WR900346.

Hassan, M. A., M. Church, and P. J. Ashworth (1992), Virtual rate and mean distance of travel of individual clasts in gravel-bed channels, *Earth Surf. Process. Landf.*, *17*(6), 617–627, doi:10.1002/esp.3290170607.

Hassan, M. A., B. Smith, D. Hogan, D. Luzi, A. Zimmermann, and B. Eaton (2008), Sediment storage and transport in coarse bed streams: scale considerations, in *Gravel-Bed Rivers VI: From Process Understanding to River Restoration*, pp. 473–496, Elsevier Science.

Hassan, M. A., H. Voepel, R. Schumer, G. Parker, and L. Fraccarollo (2013), Displacement characteristics of coarse fluvial bed sediment, *J. Geophys. Res. Earth Surf.*, *118*, 155–165, doi:10.1029/2012JF002374.

Hill, K. M., L. DellAngelo, and M. M. Meerschaert (2010), Heavy-tailed travel distance in gravel bed transport: An exploratory enquiry, *J. Geophys. Res.*, *115*, F00A14, doi:10.1029/2009JF001276.

Hjulström, F. (1935), Studies of the morphological activity of rivers as illustrated by the River Fyris. Inaugural dissertation, Almqvist & Wiksells, Uppsala.

Howard, A. D., W. E. Dietrich, and M. A. Seidl (1994), Modeling fluvial erosion on regional to continental scales, *J. Geophys. Res. Solid Earth*, *99*(B7), 13971–13986, doi:10.1029/94JB00744.

Jarrett, R. (1984), Hydraulics of High-Gradient Streams, *J. Hydraul. Eng.*, *110*(11), 1519–1539, doi:10.1061/(ASCE)0733-9429(1984)110:11(1519).

Johnson, C. W., C. L. Hanson, J. P. Smith, and R. L. Engleman (1977), Helley-Smith Bed Load Samplers, *J. Hydraul. Div.*, *103*(10), 1217–1221.

King, J., W. Emmett, P. J. Whiting, R. Kenworthy, and J. Barry (2004), *Sediment transport data and related information for selected coarse-bed streams and rivers in Idaho*, U.S. Department of Agriculture, Forest Service, Rocky Mountain Research Station, Fort Collins, CO.

Kondolf, G. M., and W. V. G. Matthews (1986), Transport of tracer gravels on a coastal California river, *J. Hydrol.*, *85*(3–4), 265–280, doi:10.1016/0022-1694(86)90060-0.

Lajeunesse, E., L. Malverti, and F. Charru (2010), Bed load transport in turbulent flow at the grain scale: Experiments and modeling, *J. Geophys. Res. Earth Surf.*, *115*(F4), 1–16, doi:10.1029/2009JF001628.

Lamarre, H., and A. G. Roy (2008), A field experiment on the development of sedimentary structures in a gravel-bed river, *Earth Surf. Process. Landf.*, *33*(7), 1064–1081, doi:10.1002/esp.1602.

Lamb, M. P., W. E. Dietrich, and J. G. Venditti (2008), Is the critical Shields stress for incipient sediment motion dependent on channel-bed slope?, *J. Geophys. Res.*, *113*, 20 PP., doi:200810.1029/2007JF000831.

Laronne, J. B., and M. A. Carson (1976), Interrelationships between bed morphology and bed-material transport for a small, gravel-bed channel, *Sedimentology*, *23*(1), 67–85, doi:10.1111/j.1365-3091.1976.tb00039.x.

Lee, H., and I. Hsu (1994), Investigation of Saltating Particle Motions, *J. Hydraul. Eng.*, *120*(7), 831–845, doi:10.1061/(ASCE)0733-9429(1994)120:7(831).

Lenzi, M., L. Mao, and F. Comiti (2006a), When does bedload transport begin in steep boulder-bed streams?, *Hydrol. Process.*, *20*(16), 3517–3533, doi:10.1002/hyp.6168.

Lenzi, M. A., L. Mao, and F. Comiti (2004), Magnitude-frequency analysis of bed load data in an Alpine boulder bed stream, *Water Resour. Res.*, *40*, 12 PP., doi:200410.1029/2003WR002961.

Lenzi, M. A., L. Mao, and F. Comiti (2006b), Effective discharge for sediment transport in a mountain river: Computational approaches and geomorphic effectiveness, *J. Hydrol.*, *326*(1-4), 257–276, doi:10.1016/j.jhydrol.2005.10.031.

Leopold, L. B., and M. G. Wolman (1960), River Meanders, *Geol. Soc. Am. Bull.*, *71*(6), 769–793, doi:10.1130/0016-7606(1960)71[769:RM]2.0.CO;2.

Leopold, L. B., M. G. Wolman, and J. P. Miller (1964), *Fluvial processes in geomorphology*, W.H. Freemand and Co., Mineola, NY.

Liedermann, M., M. Tritthart, and H. Habersack (2013), Particle path characteristics at the large gravel-bed river Danube: results from a tracer study and numerical modelling, *Earth Surf. Process. Landf.*, *38*(5), 512–522, doi:10.1002/esp.3338.

Mackin, H. (1948), Concept of the graded river, *Geol. Soc. Am. Bull.*, *59*(5), 463–512, doi:10.1130/0016-7606(1948)59[463:COTGR]2.0.CO;2.

Mao, L., and N. Surian (2010), Observations on sediment mobility in a large gravel-bed river, *Geomorphology*, *114*(3), 326–337, doi:10.1016/j.geomorph.2009.07.015.

Mao, L., G. P. Uyttendaele, A. Iroumé, and M. A. Lenzi (2008), Field based analysis of sediment entrainment in two high gradient streams located in Alpine and Andine environments, *Geomorphology*, *93*(3–4), 368–383, doi:10.1016/j.geomorph.2007.03.008.

Marion, D., and F. Weirich (2003), Equal-mobility bed load transport in a small, step-pool channel in the Ouachita Mountains, *Geomorphology*, *55*(1-4), 139–154, doi:10.1016/S0169-555X(03)00137-5.

Martin, R. L., D. J. Jerolmack, and R. Schumer (2012), The physical basis for anomalous diffusion in bed load transport, *J. Geophys. Res.*, *117*, 18 PP., doi:201210.1029/2011JF002075.

Martin, R. L., P. K. Purohit, and D. J. Jerolmack (2014), Sedimentary bed evolution as a mean-reverting random walk: Implications for tracer statistics, *Geophys. Res. Lett.*, *41*(17), 6152–6159, doi:10.1002/2014GL060525.

May, C. L., and B. S. Pryor (2013), Initial Motion and Bedload Transport Distance Determined by Particle Tracking in a Large Regulated River, *River Res. Appl.*, n/a–n/a, doi:10.1002/rra.2665.

McNamara, J. P., and C. Borden (2004), Observations on the movement of coarse gravel using implanted motion-sensing radio transmitters, *Hydrol. Process.*, *18*(10), 1871–1884, doi:10.1002/hyp.1453.

Milhous, R. T. (1973), Sediment transport in a gravel-bottomed stream, Oregon State University, Corvallis, Oregon.

Montgomery, D. R., and J. M. Buffington (1997), Channel-reach morphology in mountain drainage basins, *Geol. Soc. Am. Bull.*, *109*(5), 596–611, doi:10.1130/0016-7606(1997)109<0596:CRMIMD>2.3.CO;2.

Moog, D. B., and P. J. Whiting (1998), Annual hysteresis in bed load rating curves, *Water Resour. Res.*, *34*(9), 2393–2399, doi:10.1029/98WR01658.

Moustakidis, I., A. G. Tsakiris, and T. Papanicolaou (2010), Bridge Scour Measurements Using the Rfid Technology, *AGU Fall Meet. Abstr.*, *-1*, 0607.

Mueller, E. R., J. Pitlick, and J. M. Nelson (2005), Variation in the reference Shields stress for bed load transport in gravel-bed streams and rivers, *Water Resour. Res.*, *41*(4), n/a–n/a, doi:10.1029/2004WR003692.

Nichols, M. H. (2004), A Radio Frequency Identification System for Monitoring Coarse Sediment Particle Displacement, *Appl. Eng. Agric.*, *20*(6), 783–787.

Niezgoda, S., and T. West (2007), Stream Restoration Design Discharge for Snowmelt Dominated Streams., in *Restoring Our Natural Habitat*, pp. 1–10, American Society of Civil Engineers, Tampa, Florida.

Niezgoda, S., P. Wilcock, D. Baker, J. Price, J. Castro, J. Curran, T. Wynn-Thompson, J. Schwartz, and F. Shields (2014), Defining a Stream Restoration Body of Knowledge as a Basis for National Certification, *J. Hydraul. Eng.*, *140*(2), 123–136, doi:10.1061/(ASCE)HY.1943-7900.0000814.

Nikora, V., H. Habersack, T. Huber, and I. McEwan (2002), On bed particle diffusion in gravel bed flows under weak bed load transport, *Water Resour. Res.*, *38*(6), 17–1–17–9, doi:10.1029/2001WR000513.

Niño, Y., M. García, and L. Ayala (1994), Gravel saltation: 1. Experiments, *Water Resour. Res.*, *30*(6), 1907–1914, doi:10.1029/94WR00533.

Nolan, K. M., T. E. Lisle, and H. M. Kelsey (1987), Bankfull discharge and sediment transport in northwestern California, in *Proceedings of the Corvallis Symposium*, International Association of Hydrological Sciences, Corvallis, Oregon.

Northwest Watershed Research Center (2009), *Reynolds Creek Experimental Watershed: 1 m airborne LiDAR*, U.S. Department of Agriculture: Agricultural Research Service, Boise, Idaho.

Northwest Watershed Research Center (2015), *Reynolds Creek streamflow data: Tollgate station 116b*, U.S. Department of Agriculture: Agricultural Research Service, Boise, Idaho.

Onset Computer Corporation (2011), *HOBO Pendant G Acceleration Data Logger (Part # UA-004-64) Manual*, Bourne, MA.

Papanicolaou, A. N., K. Strom, A. Schuyler, and N. Talebbeydokhti (2003), The role of sediment specific gravity and availability on cluster evolution, *Earth Surf. Process. Landf.*, *28*(1), 69–86, doi:10.1002/esp.427.

Parker, G. (1990a), Surface-based bedload transport relation for gravel rivers, *J. Hydraul. Res.*, *28*(4), 417, doi:10.1080/00221689009499058.

Parker, G. (1990b), *The ACRONYM series of PSACAL programs for computing bedload transport in gravel rivers*, University of Minnesota, St. Anthony Falls Laboratory.

Parker, G. (2008), Transport of Gravel and Sediment Mixtures, in *Sedimentation Engineering*, pp. 165–251, American Society of Civil Engineers.

Parker, G., P. C. Klingeman, and D. G. McLean (1982), Bedload and size distribution in paved gravel-bed streams, *J. Hydraul. Div.*, *108*(4), 544–571.

Phillips, C. B., and D. J. Jerolmack (2014), Dynamics and mechanics of bed-load tracer particles, *Earth Surf. Dyn.*, *2*(2), 513–530, doi:10.5194/esurf-2-513-2014.

Phillips, C. B., R. L. Martin, and D. J. Jerolmack (2013), Impulse framework for unsteady flows reveals super-diffusive bed load transport, *Geophys. Res. Lett.*, *40*, 1328–1333, doi:10.1002/grl.50323.

Phillips, J. D. (2002), Geomorphic impacts of flash flooding in a forested headwater basin, *J. Hydrol.*, *269*(3–4), 236–250, doi:10.1016/S0022-1694(02)00280-9.

Pierson, F. B., C. W. Slaughter, and Z. K. Cram (2001), Long-Term Stream Discharge and Suspended-Sediment Database, Reynolds Creek Experimental Watershed, Idaho, United States, *Water Resour. Res.*, *37*(11), PAGES 2857–2861, doi:10.1029/2001WR000420.

Pyrce, R. S., and P. E. Ashmore (2003), The relation between particle path length distributions and channel morphology in gravel-bed streams: a synthesis, *Geomorphology*, *56*(1–2), 167–187, doi:10.1016/S0169-555X(03)00077-1.

Recking, A., F. Liébault, C. Peteuil, and T. Jolimet (2012), Testing bedload transport equations with consideration of time scales, *Earth Surf. Process. Landf.*, *37*(7), 774–789, doi:10.1002/esp.3213.

Rickenmann, D. (2001), Comparison of bed load transport in torrents and gravel bed streams, *Water Resour. Res.*, *37*(12), 3295–3305, doi:10.1029/2001WR000319.

Ross, C., and J. D. Forrester (1958), *Outline of the Geology of Idaho*, Idaho Bureau of Mines and Geology, Moscow, Idaho.

Scheingross, J. S., E. W. Winchell, M. P. Lamb, and W. E. Dietrich (2013), Influence of bed patchiness, slope, grain hiding, and form drag on gravel mobilization in very steep streams, *J. Geophys. Res. Earth Surf.*, n/a–n/a, doi:10.1002/jgrf.20067.

Schmidt, K.-H., and P. Ergenzinger (1992), Bedload entrainment, travel lengths, step lengths, rest periods—studied with passive (iron, magnetic) and active (radio) tracer techniques, *Earth Surf. Process. Landf.*, *17*(2), 147–165, doi:10.1002/esp.3290170204.

Schneider, J., R. Hegglin, S. Meier, J. M. Turowski, M. Nitsche, and D. Rickenmann (2010), Studying sediment transport in mountain rivers by mobile and stationary RFID antennas, in *River Flow*, pp. 1723–1730, Bundesanstalt für Wasserbau.

Schumer, R., M. M. Meerschaert, and B. Baeumer (2009), Fractional advection-dispersion equations for modeling transport at the Earth surface,

Segura, C., and J. Pitlick (2010), Scaling frequency of channel-forming flows in snowmelt-dominated streams, *Water Resour. Res.*, *46*(6), W06524, doi:10.1029/2009WR008336.

Seyfried, M., R. Harris, D. Marks, and B. Jacob (2001), Geographic Database, Reynolds Creek Experimental Watershed, Idaho, United States, *Water Resour. Res.*, *37*(11), 2825, doi:10.1029/2001WR000414.

Shields, A. (1936), Anwendung der Aehnlichkeitsmechanik und der Turbulenzforschung auf die Geschiebebewegung, *Mitt Preuss Vers. Wasserbau Schiffbau*, *26*, 36.

Shields, F. J., R. R. Copeland, P. C. Klingeman, M. W. Doyle, and A. Simon (2003), Design for Stream Restoration, *J. Hydraul. Eng.*, *129*(8), 575–584, doi:http://dx.doi.org.ezproxy.lib.utexas.edu/10.1061/(ASCE)0733-9429(2003)129:8(575.

Sholtes, J., K. Werbylo, and B. Bledsoe (2014), Physical context for theoretical approaches to sediment transport magnitude-frequency analysis in alluvial channels, *Water Resour. Res.*, n/a–n/a, doi:10.1002/2014WR015639.

Singh, A., K. Fienberg, D. J. Jerolmack, J. Marr, and E. Foufoula-Georgiou (2009), Experimental evidence for statistical scaling and intermittency in sediment transport rates, *J. Geophys. Res.*, *114*, 16 PP., doi:200910.1029/2007JF000963.

Snyder, N. P. (2010), 1D open channel flows on lidar data using HEC-RAS and HEC-GeoRAS, pp. 181–205, Boulder, CO.

Strom, K., A. Papanicolaou, N. Evangelopoulos, and M. Odeh (2004), Microforms in Gravel Bed Rivers: Formation, Disintegration, and Effects on Bedload Transport, *J. Hydraul. Eng.*, *130*(6), 554–567, doi:10.1061/(ASCE)0733-9429(2004)130:6(554).

Sugai, T. (1993), River terrace development by concurrent fluvial processes and climatic changes, *Geomorphology*, *6*(3), 243–252, doi:10.1016/0169-555X(93)90049-8.

Thompson, C., and J. Croke (2008), Channel flow competence and sediment transport in upland streams in southeast Australia, *Earth Surf. Process. Landf.*, *33*(3), 329–352, doi:10.1002/esp.1558.

Torizzo, M., and J. Pitlick (2004), Magnitude-frequency of bed load transport in mountain streams in Colorado, *J. Hydrol.*, *290*(1–2), 137–151, doi:10.1016/j.jhydrol.2003.12.001.

Tremblay, M., G. A. Marquis, and A. G. Roy (2010), A new method for tracking individual particles during bed load transport in a gravel-bed river, Abstract #EP53A-0599, San Francisco, CA.

Trush, W. J., S. M. McBain, and L. B. Leopold (2000), Attributes of an alluvial river and their relation to water policy and management, *Proc. Natl. Acad. Sci.*, *97*(22), 11858–11863, doi:10.1073/pnas.97.22.11858.

Turowski, J. M., A. Badoux, and D. Rickenmann (2011), Start and end of bedload transport in gravel-bed streams, *Geophys. Res. Lett.*, *38*, 5 PP., doi:201110.1029/2010GL046558.

U.S. Army Corps of Engineers (2010), *HEC-RAS*.

USDA-NRCS (2007), Chapter 11: Rosgen Geomorphic Channel Design, in *National Engineering Handbook*, vol. Part 654, p. 82, US Department of Agriculture, Natural Resources Conservation Serive, Washington, D.C.

Vericat, D., M. Church, and R. J. Batalla (2006), Bed load bias: Comparison of measurements obtained using two (76 and 152 mm) Helley-Smith samplers in a gravel bed river, *Water Resour. Res.*, *42*(1), W01402, doi:10.1029/2005WR004025.

Voepel, H., R. Schumer, and M. A. Hassan (2013), Sediment residence time distributions: Theory and application from bed elevation measurements, *J. Geophys. Res. Earth Surf.*, *118*(4), 2013JF002816, doi:10.1002/jgrf.20151.

Weeks, E. R., J. S. Urbach, and H. L. Swinney (1996), Anomalous diffusion in asymmetric random walks with a quasi-geostrophic flow example, *Phys. Nonlinear Phenom.*, *97*(1–3), 291–310, doi:10.1016/0167-2789(96)00082-6.

Whipple, K. X., and G. E. Tucker (1999), Dynamics of the stream-power river incision model: Implications for height limits of mountain ranges, landscape response timescales, and research needs, *J. Geophys. Res.*, *104*(B8), PP. 17,661–17,674, doi:199910.1029/1999JB900120.

Whitaker, A. C., and D. F. Potts (2007), Analysis of flow competence in an alluvial gravel bed stream, Dupuyer Creek, Montana, *Water Resour. Res.*, *43*(7), W07433, doi:10.1029/2006WR005289.

Whiting, P. J., J. F. Stamm, D. B. Moog, and R. L. Orndorff (1999), Sediment-transporting flows in headwater streams, *Geol. Soc. Am. Bull.*, *111*(3), 450–466, doi:10.1130/0016-7606(1999)111<0450:STFIHS>2.3.CO;2.

Wilcock, P. R. (1992), Flow competence: A criticism of a classic concept, *Earth Surf. Process. Landf.*, *17*(3), 289–298, doi:10.1002/esp.3290170307.

Wilcock, P. R., and J. C. Crowe (2003), Surface-based Transport Model for Mixed-Size Sediment, *J. Hydraul. Eng.*, *129*(2), 120–128, doi:10.1061/(ASCE)0733-9429(2003)129:2(120).

Wilcock, P. R., J. Pitlick, and Y. Cui (2009), *Sediment transport primer: estimating bed-material transport in gravel-bed rivers*, General Technical Report, US Department of Agriculture, Forest Service, Rocky Mountain Research station, Fort Collins, CO.

Wohl, E. (2010), *Mountain Rivers Revisited*, Water Resources Monograph, American Geophysical Union, Washington, D. C.

Wolman (1954), A method of sampling coarse river-bed material, *Trans. Am. Geophys. Union*, *35*(6), 951–956.

Wolman, M. G., and J. P. Miller (1960), Magnitude and Frequency of Forces in Geomorphic Processes, *J. Geol.*, *68*(1), 54–74.

Wong, M., G. Parker, P. DeVries, T. M. Brown, and S. J. Burges (2007), Experiments on dispersion of tracer stones under lower-regime plane-bed equilibrium bed load transport, *Water Resour. Res.*, *43*, 23 PP., doi:200710.1029/2006WR005172.

Yager, E. M., J. W. Kirchner, and W. E. Dietrich (2007), Calculating bed load transport in steep boulder bed channels, *Water Resour. Res.*, *43*, 24 PP.

Yager, E. M., W. E. Dietrich, J. W. Kirchner, and B. W. McArdell (2012a), Prediction of sediment transport in step-pool channels, *Water Resour. Res.*, *48*, 20 PP., doi:201210.1029/2011WR010829.

Yager, E. M., J. M. Turowski, D. Rickenmann, and B. W. McArdell (2012b), Sediment supply, grain protrusion, and bedload transport in mountain streams, *Geophys. Res. Lett.*, *39*(10), L10402, doi:10.1029/2012GL051654.

Yang, C. T. Y., and W. W. Sayre (1971), Longitudinal Dispersion of Bed-Material Particles, *J. Hydraul. Div.*, *97*(7), 907–921.

Yolcubal, I., M. L. Brusseau, J. Artiola, P. Wierenga, and L. G. Wilson (2004), Environmental physical properties and processes, in *Environmental Monitoring*

and Characterization, edited by J. Artiola, I. L. Pepper, and M. L. Brusseau, pp. 207–239, Academic Press, San Diego, CA.

Ziegler, A. D., R. C. Sidle, V. X. H. Phang, S. H. Wood, and C. Tantasirin (2014), Bedload transport in SE Asian streams—Uncertainties and implications for reservoir management, *Geomorphology, 227*, 31–48, doi:10.1016/j.geomorph.2014.01.015.